



TECHNICAL NOTE

TN-FT-76-4

FINAL REPORT

CONTRACT NAS8-28988

METHODS FOR DATA REDUCTION AND LOADS ANALYSIS

OF

SPACE SHUTTLE SOLID ROCKET BOOSTER  
MODEL WATER IMPACT TESTS

SEPTEMBER 1976

Prepared by

AERO/HYDRODYNAMICS GROUP  
ADVANCED DEVELOPMENT DEPARTMENT  
CHRYSLER CORPORATION SPACE DIVISION  
NEW ORLEANS, LOUISIANA



## SUMMARY

This report presents the methodology used to predict full-scale Space Shuttle Solid Rocket Booster (SRB) water impact loads from scale model test data. Tests conducted included 12.5 inch and 120 inch diameter models of the SRB. Geometry and mass characteristics of the models were varied in each test series to reflect the current SRB baseline configuration. Nose first and tail first water entry modes were investigated with full-scale initial impact vertical velocities of 40 to 120 ft/sec, horizontal velocities of 0 to 60 ft/sec., and off-vertical angles of 0 to  $\pm 30$  degrees. The test program included a series of tests with scaled atmospheric pressure.

Scaling relationships were established analytically and later verified by test. Full-scale equivalent loads were subsequently estimated by applying these scaling relationships to the model test data for the current SRB baseline configuration. Load distributions on the cylindrical body, aft bulkhead, nozzle and skirt were predicted for the significant dynamic events of initial impact, cavity collapse, maximum penetration, rebound and slapdown.

Loads developed during water impact were found to have a significant influence on the structural design of the SRB. Initial impact loads are critical to the design of the nozzle, aft skirt, aft bulkhead, lower cylindrical body and auxiliary components mounted in the nozzle-skirt annulus region. Loads developed during cavity collapse also define design requirements for the aft skirt and lower cylindrical body. Hydrostatic loads developed during maximum penetration are significant to the design of the lower cylindrical body,

while slapdown loads influence the design of upper cylindrical body and forward skirt.

This study was conducted in support of the NASA/MSFC Booster Recovery Program under NASA/MSFC Contract NAS8-28988.

## TABLE OF CONTENTS

	<u>PAGE</u>
LIST OF ILLUSTRATIONS	v
LIST OF TABLES	x
1.0 INTRODUCTION	1-1
2.0 TEST MODELS AND INSTRUMENTATION	2-1
3.0 TEST PROGRAMS	3-1
3.1 TEST SERIES C-143	3-1
3.2 NOL 12.5 INCH MODEL TEST	3-2
3.3 TEST SERIES C-145	3-2
3.4 TEST SERIES P-015	3-3
3.5 TEST SERIES P-022	3-3
3.6 TEST SERIES P-029	3-4
3.7 TEST SERIES TMS-333	3-4
3.8 TEST SERIES UNO-1	3-5
4.0 DATA ACQUISITION AND PROCESSING	4-1
5.0 SRB WATER IMPACT DYNAMIC EVENTS	5-1
5.1 INITIAL IMPACT	5-1
5.2 CAVITY FORMATION AND COLLAPSE	5-4
5.3 MAXIMUM PENETRATION	5-7
5.4 REBOUND AND SLAPDOWN	5-7
6.0 SCALING RELATIONSHIPS	6-1
7.0 DATA ANALYSIS	7-1
7.1 INITIAL IMPACT	7-3
7.2 CAVITY COLLAPSE	7-6
7.3 MAXIMUM PENETRATION	7-10
7.4 SLAPDOWN	7-10
8.0 FULL SCALE LOADS	8-1
8.1 INITIAL IMPACT	8-1
8.2 CAVITY COLLAPSE	8-11
8.3 MAXIMUM PENETRATION	8-17
8.4 SLAPDOWN	8-18
8.5 COMPONENT LOADS	8-23
8.5.1 NOSE CONE FRUSTUM LOADS	8-24
8.5.2 SYSTEM TUNNEL LOADS	8-26
8.5.3 E.T. ATTACH RING LOADS	8-26

TABLE OF CONTENTS (CONTINUED)

	<u>PAGE</u>
8.5.4 AFT SEPARATION MOTOR LOADS	8-27
8.5.5 TVC PACKAGE LOADS	8-27
8.5.6 NOZZLE ACTUATOR LOADS	8-28
8.5.7 HEAT SHIELD/AFT END RING LOADS	8-30
8.5.8 SRM CLEVIS JOINT PIN RETAINER BAND LOADS	8-31
9.0 REFERENCES	9-1
APPENDIX A TYPICAL SET OF MODEL TEST DATA	A-1
APPENDIX B SCALING OF TAIL-FIRST, VERTICAL WATER ENTRY MODEL TESTS OF THE SPACE SHUTTLE SOLID ROCKET BOOSTER	B-1

## LIST OF ILLUSTRATIONS

<u>FIGURE NUMBER</u>	<u>TITLE</u>	<u>PAGE NUMBER</u>
2-1	156 Inch-Diameter SRB Configuration	2-8
2-2	Space Shuttle Solid Rocket Booster 4/11/73 Baseline Configuration	2-9
2-3	11/1/75 Baseline SRB Water Impact Configuration	2-10
2-4	Basic Model, 4-11-73 Configuration	2-11
2-5	Pressure Transducer Locations, 4-11-73 Configuration	2-12
2-6	Accelerometer Locations, 4-11-73 Configuration	2-15
3-1	SRB Water Impact Loads Coordinate System	3-15
4-1	Data Acquisition and Processing Block Diagram	4-4
5-1	Qualitative Vehicle Trajectory During Impact	5-9
5-2	SRB Water Impact Dynamic Events	5-10
5-3	Cavity Development and Collapse	5-13
6-1	Comparison of 12.5 Inch and 120 Inch-Diameter Model Peak Internal Nozzle Pressures	6-5
6-2	Comparison of 12.5 Inch and 120 Inch-Diameter Model Internal Nozzle Pressures (Peak Values)	6-6
6-3	Comparison of 12.5 Inch and 120 Inch-Diameter Model Internal Nozzle Pressures (10 Milisecond Average)	6-7
6-4	Comparison of 12.5 Inch and 120 Inch-Diameter Model Internal Nozzle Pressures (Peak Values)	6-8
6-5	Comparison of 12.5 Inch and 120 Inch-Diameter Model Internal Nozzle Pressures (10 Milisecond Average)	6-9
6-6	Comparison of 12.5 Inch and 120 Inch-Diameter Model Peak Slapdown Pressure	6-10

LIST OF ILLUSTRATIONS (Continued)

<u>FIGURE NUMBER</u>	<u>TITLE</u>	<u>PAGE NUMBER</u>
6-7	Comparison of 12.5 Inch and 120 Inch-Diameter Model Primary Slapdown Pressures (Peak Values)	6-11
6-8	Comparison of 12.5 Inch and 120 Inch-Diameter Model Primary Slapdown Pressures (10 Millisecond Average)	6-12
7-1	Typical Model Test Data (Test P015-70)	7-13
7-2	Pressure Distribution at Nozzle Toe-In (With Nozzle Extension)	7-14
7-3	Determination of Maximum Pitch and Axial Acceleration Times	7-15
7-4	Description of Vehicle Aft End Geometry (with Nozzle Extension)	7-16
7-5	Pressure Distribution at Maximum Pitch Acceleration (Without Nozzle Extension)	7-17
7-6	Pressure Distribution at Maximum Pitch Acceleration (With Nozzle Extension)	7-18
7-7	Correlation of Nozzle Pressure D21	7-19
7-8	Extrapolation of Nozzle Pressures	7-20
7-9	Variation of Nozzle Internal Pressure with Impact Conditions, Maximum Pitch Acceleration	7-21
7-10	Pressure Distribution at Maximum Axial Acceleration (With Nozzle Extension)	7-22
7-11	Variation of Maximum Acceleration Levels with Impact Conditions, Maximum Pitch Acceleration	7-23
7-12	Variation of Maximum Acceleration Levels with Impact Conditions, Maximum Pitch Acceleration	7-24
7-13	Normalized Shear Force, Bending Moment, and Axial Force Distributions, Maximum Axial or Pitch Accelerations	7-25
7-14	Qualitative Description of Cavity Formation and Collapse	7-26



LIST OF ILLUSTRATIONS (Continued)

<u>FIGURE NUMBER</u>	<u>TITLE</u>	<u>PAGE NUMBER</u>
7-15	Typical Cavity Collapse Radial Pressure Distribution, NOL 12.5 inch-Diameter Model	7-28
7-16	Cavity Collapse Pressure Distributions, SRM Case and Aft Skirt Pressures	7-29
7-17	Cavity Collapse Pressure Distribution Factor, $K_C$	7-30
7-18	Cavity Collapse Pressure Distribution Function Parameter, $\eta$	7-31
7-19	Variation of Penetration Depth With Impact Conditions	7-32
7-20	Variation of Angle at Maximum Penetration with Impact Conditions	7-33
7-21	Typical Time Histories of Slapdown Pressures	7-34
7-22	Typical Full Scale Trajectory for Vehicle C.G., Test P015-70	7-35
7-23	Qualitative Vehicle Trajectory During Impact	7-36
8-1	Correlation of Internal Skirt Pressures, Maximum Pitch Acceleration Event	8-36
8-2	Correlation of Bulkhead Pressures, Maximum Axial Acceleration Event	8-37
8-3	Correlation of C.G. Accelerations, Maximum Pitch Acceleration Event	8-38
8-4	Correlation of C.G. Accelerations, Maximum Axial Acceleration Event	8-39
8-5	Correlation of Peak Lee Side Cavity Collapse Pressure	8-40
8-6	Correlation of C.G. Accelerations at Cavity Collapse	8-41
8-7	SRB Water Impact Cavity Collapse Loads 5/1/75 Full Scale Configuration	8-42
8-8	Maximum Penetration Depth	8-43

LIST OF ILLUSTRATIONS (Continued)

<u>FIGURE NUMBER</u>	<u>TITLE</u>	<u>PAGE NUMBER</u>
8-9	Pitch Angle at Maximum Penetration Depth	8-44
8-10	Minimum Expected Ullage Pressure for Solid Rocket Motor	8-45
8-11	Typical Nose Pitch Acceleration Time History	8-46
8-12	Typical C.G. Pitch Acceleration Time History	8-47
8-13	Typical Slapdown Pressure Time History	8-48
8-14	Slapdown Pressure Distribution Procedure	8-49
8-15	Slapdown Pitch Angle ( $\theta_{LW}$ ) - Degrees	8-50
8-16	Slapdown Radial Pressure Distributions	8-51
8-17	Variation of Slapdown Keel Peak Pressure with Impact Condition	8-52
8-18	SRB Slapdown Dynamics	8-53
8-19	SRB Water Impact Slapdown Loads, 5/1/75 Full Scale Configuration, Keel Pressure	8-54
8-20	SRB Water Impact Slapdown Loads, 5/1/75 Full Scale Configuration, Applied Pressure and Inertial Reaction Loads	8-55
8-21	SRB Water Impact Slapdown Loads, 5/1/75 Full Scale Configuration, Bending Moment	8-56
8-22	SRB Water Impact Slapdown Loads, 5/1/75 Full Scale Configuration, Shear	8-57
8-23	Component Acceleration Load Factors	8-58
8-24	Surface Pressure Coefficients for SRB Nose Cone Frustum	8-59
8-25	Nose Cone Configuration and Coordinate System	8-60
8-26	Systems Tunnel Water Impact Pressure Distributions	8-61
8-27	E.T. Attach Ring Water Impact Pressure Loads	8-62

LIST OF ILLUSTRATIONS (Continued)

<u>FIGURE NUMBER</u>	<u>TITLE</u>	<u>PAGE NUMBER</u>
8-28	Aft Separation Motor Water Impact Load	8-63
8-29	TVC Package Water Impact Loads	8-65
8-30	Nozzle Actuator Water Impact Load	8-67
8-31	Heat Shield Water Impact Configuration	8-70
8-32	$\Gamma$ - Function	8-71

LIST OF TABLES

<u>TABLE NUMBER</u>	<u>TITLE</u>	<u>PAGE NUMBER</u>
2-1	Characteristics of the 156 Inch-Diameter Configuration - Prototype and Models	2-5
2-2	Characteristics of the SRB 4/11/73 Baseline Configuration - Prototype and Models	2-6
2-3	Characteristics of the SRB 11/1/74 Baseline Configuration - Prototype and Models	2-7
3-1	Test Matrix - Test Series C-143	3-6
3-2	Test Matrix - NOL 12.5 Inch Model Test	3-7
3-3	Test Matrix - Test Series C-145	3-8
3-4	Test Matrix - Test Series P-015	3-9
3-5	Test Matrix - Test Series P-022	3-11
3-6	Test Matrix - Test Series P-029	3-12
3-7	Test Matrix - Test Series TMS-333	3-13
3-8	Test Matrix - Test Series UNO-1	3-14
8-1	Nose Cone Frustum Trajectory Listing	8-32
8-2	SRM Nozzle Actuator Response Loads	8-33

## SECTION 1.0

### INTRODUCTION

The initial stage of the Space Shuttle launch configuration will consist of two parallel-burn solid rocket boosters (SRB). After burn-out, the boosters will separate and return to earth for a sea landing. They will then be recovered at sea and subsequently refurbished for use again in later flights. Although a parachute recovery system will be used for deceleration prior to impact, the SRB will land with considerable vertical velocity. In addition, surface winds may superimpose appreciable drift velocities. Therefore, the SRB will experience relatively high acceleration and pressure loads at the time of impact and must be designed to withstand these loads in addition to the normal operating loads imposed during the propulsive boost ascent and stage separation phases.

In order to assess the magnitude and nature of these water impact loads and to study the general feasibility of water recovery, a test program was initiated using scale models of the SRB. Initial tests were conducted with a 12.5 inch-diameter model, geometrically similar to the original SRB design, which was a 156-inch diameter SRB. The objectives of these tests were to evaluate entry modes, flotation attitudes, penetration characteristics, fundamental fluid dynamic characteristics, and to obtain preliminary design loads. Additional tests were performed with a 120 inch-diameter Titan IIIC SRB for the purpose of verifying scaling relationships previously determined analytically. Results of these tests are described in References 4 to 8. More recent tests were designed to study the SRB 4-11-73 and 11-1-74 baseline

configuration. In these programs, 12.5 inch-diameter models were used to evaluate configuration effects and to assess the effects of wind drift (horizontal velocity).

The data base accumulated during the scale model test programs has been used to predict full scale water impact loads and assess the impact of configuration changes as the SRB evolved from the original design to the current 5/1/75 configuration. These loads for the various SRB configurations have been published in References 1 to 3 and 30 to 33.

These loads have served as a basis for trade studies related to SRB structural design and selection of the required recovery system. The methodology used in the data reduction and subsequent analysis is presented here.

## SECTION 2.0

### TEST MODELS AND INSTRUMENTATION

The configurations used in these tests were of two basic designs, a modified Titan III-C SRB and the 4-11-73 baseline SRB configuration. The modified Titan III-C SRB design, 156 in. in diameter, reflects initial thinking on the Space Shuttle design concept which called for a booster with fixed, canted nozzle, shielded by a straight skirt as illustrated in Figure 2-1. Two instrumented models, one of 12.5 inch-diameter and the other of 120 inch-diameter, were fabricated and tested. Pertinent dimensions and mass characteristics of the prototype and test models are given in Table I.

The 4-11-73 baseline configuration reflects a later design decision to incorporate a gimbaled nozzle for booster thrust control. The design, shown in Figure 2-2, features a nozzle whose neutral position is in line with the vehicle axis and which is shielded by a flared skirt to permit gimbaling. Several variations of this configuration were tested with a 12.5 in. diameter model. The original configuration incorporated a full-length nozzle ("long nozzle", "with nozzle extension"). Early testing indicated that water impact loads on the nozzle were quite severe. In order to provide for relief of these loads if later deemed necessary, the design option of jettisoning the nozzle extension prior to water impact was incorporated into the program. Therefore, a model configuration with shortened nozzle ("short nozzle", "without nozzle extension") was also tested to simulate the case in which the nozzle extension is jettisoned. The basic model was fitted with a conical aft bulkhead. It was later modified to incorporate a spherical aft bulkhead.

and was further modified to incorporate a baffle in the nozzle-skirt annulus region to protect the aft bulkhead from the severe pressure loads of initial impact as experienced earlier in tests with the short nozzle configuration. Pertinent dimensions and mass characteristics of the 4-11-73 configuration and models used in the different tests (discussed in the following section) are given in Table II.

The models were designed with sufficient strength to behave under load effectively as rigid bodies. Total weight, center of gravity and pitch moment of inertia were scaled as well as possible within the many constraints of design and instrumentation requirements. As can be seen in the tables, the models were overweight by no more than 15%, the center of gravity was within 6% (of model length) of the design location, and pitch moment of inertia was within  $\pm 10\%$  of the design value. No attempt was made to scale mass distribution or elastic properties of the full-scale vehicle since the structural design was still in its embryonic stages at the time and subject to certain change. Moreover, such scaling would have imposed serious limitations and restrictions on the amount and location of instrumentation installed on the model. The basic model, used for the primary tests (MSFC Test No. P-015) of the 4-11-73 configuration is shown in figure 2-4.

The models were instrumented with approximately 50 transducers to measure pressures, accelerations and strains. Transducers were strategically located to give maximum, or otherwise significant, measurements on the cylinder, aft skirt, nozzle and bulkhead. Three sets of axial, pitch and yaw accelerometers were located near the nose, center of gravity and tail to aid in determining total vehicle loads. Pressure transducer and accelerometer locations for the



basic 4-11-73 configuration model are shown in figures 2-5 and 2-6. Strain gages were distributed so as to determine local stresses over the vehicle and shear, bending moment and axial force at one station. Pressure transducers were located so as to aid in determining the loads on individual components and to help in assessing the fluid dynamics involved in the water impact. Slight variations in the type, number and location of transducers were made to meet the data requirements defined by individual test objectives. In all cases, an epoxy potting compound and silicone grease were used to waterproof the instruments, and RTV was added to protect the transducers from thermal shock at water entry. Nevertheless, strain gages bonded to the vehicle skin were quite susceptible to damage during test, and very little data was obtained from them. Due to the shortcomings in strain data no attempt was made at stress analysis in the present study. However, such analyses have been made, using data from the 120 inch-diameter model, and are reported separately in References 13 and 14. Accelerometers and pressure transducers were bench-calibrated in the MSFC Metrology Laboratory prior to installation in the model, and calibration resistances were determined for purposes of electrical simulation of the calibration signal later during testing.

Signal conditioning equipment was packaged in a sealed instrumentation canister mounted inside the models near its center of gravity. The canister contained approximately 60 Wheatstone bridge balance circuits and three 21-channel constant bandwidth multiplexers. Each multiplex system had a 96 kc center frequency and 10 channels on 8 kc spacing each side of center frequency. All channels had a  $\pm 2$  kc bandwidth.

The models were painted with longitudinal stripes along the 90° meridians and circumferentially at three axial locations to aid in the analysis of high speed photographic data.

	156 Inch-Diameter SRB Configuration					
	Configuration Design			Scale Models - As Built		
	Full-Scale Prototype	120 in-Diam. Scale Model	12.5 in-Diam. Scale Model	C-145 Test Series Configuration	C-143 Test Series Configuration	NOL 12.5 in. Model
Length, in.	1351	1040	108.4	1056.7 (1151.7) (1151.7)	108.4	108.1
Body Diam., In.	156	120	12.5	121.1 (121.1) (121.1)	12.5	12.5
Nozzle Exit Diameter, In.	163.8	126.1	13.1	77.5 (126.1) (126.1)	13.1	13.1
Nozzle Throat Diameter, In.	54.6	42.1	4.37	46 (46) (46)	4.37	4.37
Nozzle Expansion Ratio (Area)	9.0	9.0	9.0	2.8 (7.5) (7.5)	9.0	9.0
Weight, Lbs.	190,000	87100	97.7	84500 (87700) (88500)	101.0	97.8
C.G., in. aft of Fwd Cylinder End	618	476	49.4	485.6 (505.4) (509.9)	55.32	52.75
Pitch Moment of Inertia., Slug-Ft. <sup>2</sup>	7.22X10 <sup>6</sup>	1.95X10 <sup>6</sup>	23.6	1.8X10 <sup>6</sup> (2X10 <sup>6</sup> ) (2X10 <sup>6</sup> )	20.4	23.61

NOTES: (1) Values quoted are for water impact configuration (without nose cone, frustum, or recovery system).

(2) Values in ( ) are for the configuration with standard and reinforced nozzle extension; i.e.,  
(standard nozzle extension)  
(reinforced nozzle extension)

TABLE 2-1. Characteristics of the 156 inch-Diameter Configuration - Prototype and Models

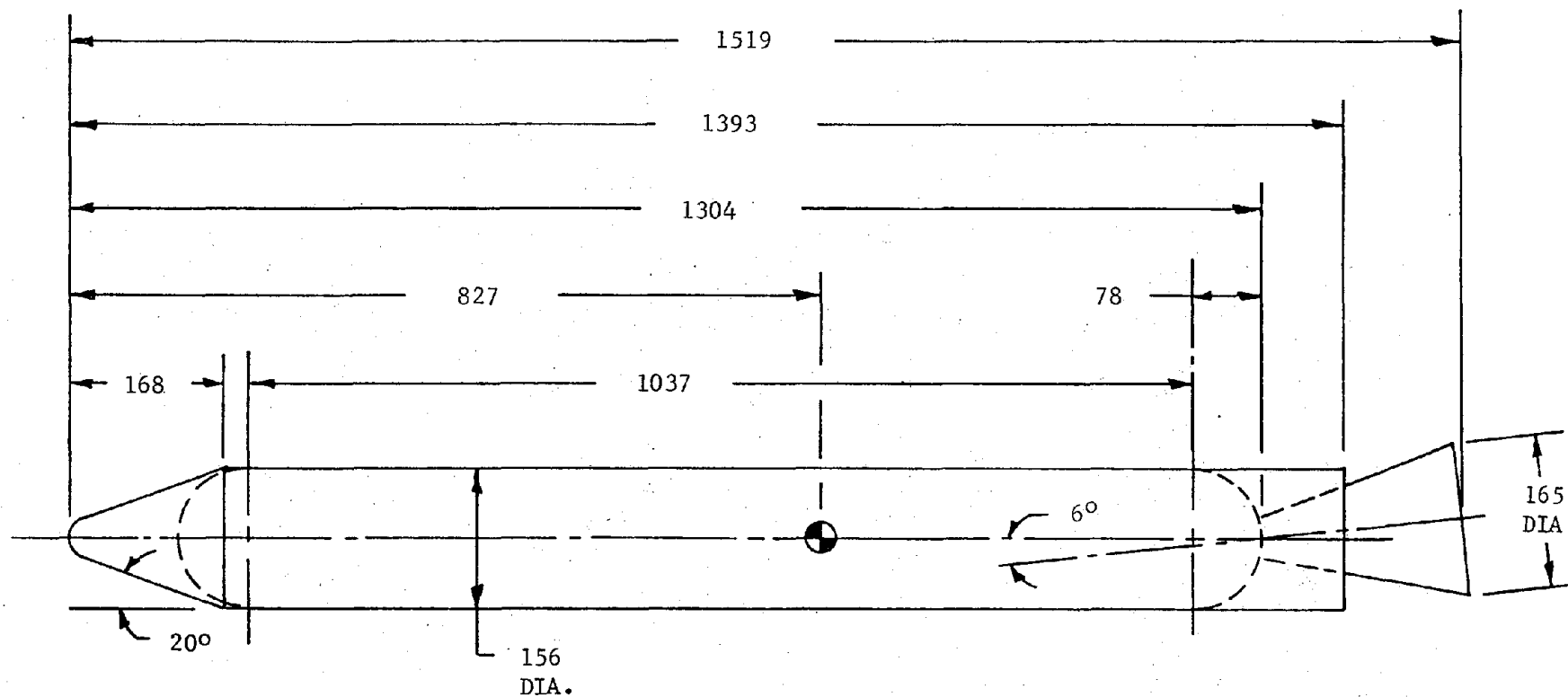
	4-11-73 Baseline Configuration				
	Configuration Design		12.5 in-Diam. Scale Models - As Built		
	Full-Scale Prototype	12.5 in-Diam. Scale Model	P-015 Test Series Configuration (Conical Bulkhead)	P-022 Test Series Configuration (Spherical Bulkhead)	P-029 Test Series Configuration Spherical Bulkhead Short Nozzle with Baffle
Length, in.	1553 (1) (1501) (2)	136.7 (132.1)	136.9 (132.3) (3)	138.8 (132.3) (3)	(132.3) (3)
Body Diam., in.	142 (142)	12.5 (12.5)	12.5 (12.5)	12.5 (12.5)	(12.5)
Nozzle Exit Diameter, in.	142 (105)	12.5 ( 9.25)	12.5 ( 9.25)	12.5 ( 7.4)	( 7.4)
Nozzle Throat Diameter, in.	53.4 (53.4)	4.7 (4.7)	4.7 (4.7)	4.7 (4.7)	(4.7)
Nozzle Expansion Ratio (Area)	7.1 (4.6)	7.1 (4.6)	7.1 (4.6)	7.1 (2.5)	(2.5)
Weight, lbs.	146,365 (4) (143,165)	99.8 (97.7)	116.7 (114.4)	115.6 (113.0)	111.0
C.G., in. Aft of Fwd. Cylinder End	864.3 (850.1)	76.1 (74.8)	74.3 (73.5)	73.2 (71.8)	(70.6)
Pitch Moment of Inertia, Slug-ft. <sup>2</sup>	7.118x10 <sup>6</sup> (4) 6.832x10 <sup>6</sup>	37.6 36.0	34.0 31.5	39.7 (39.0)	(38.5)

- NOTES: (1) Values quoted are for water impact configuration (without nose cone, frustum, or recovery system).  
 (2) Values in ( ) are for nozzle extension removed; i.e., "short nozzle".  
 (3) Includes forward bulkhead lip.  
 (4) Total mass and mass distribution taken from Ref. 15 for water impact configuration.

TABLE 2-2. Characteristics of the SRB 4-11-73 Baseline Configuration - Prototype and Models

	Configuration Design		12.5 Inch Diameter Model As Built TMS-333 Test
	Full Scale	12.5 Inch Diameter Model Scale	
Length - Inches	1530.2	131.01	131.01
Body Diameter Inches	146	12.50	12.5
Nozzle Exit Diameter Inches (Short Nozzle)	107.7	9.22	9.22
Nozzle Throat Diameter	54.4	4.66	4.66
Weight - Pounds	159706	100.2	107.2
C.G. Aft of Fwd Cylinder End	891.4	76.3	77.1
Pitch Moment of Inertia Slug-Ft <sup>2</sup>	$8.33 \times 10^6$	38.3	40.9

TABLE 2-3. Characteristics of the SRB 11-1-74 Baseline Configuration -  
Prototype and Model



## SPLASHDOWN MASS PROPERTIES

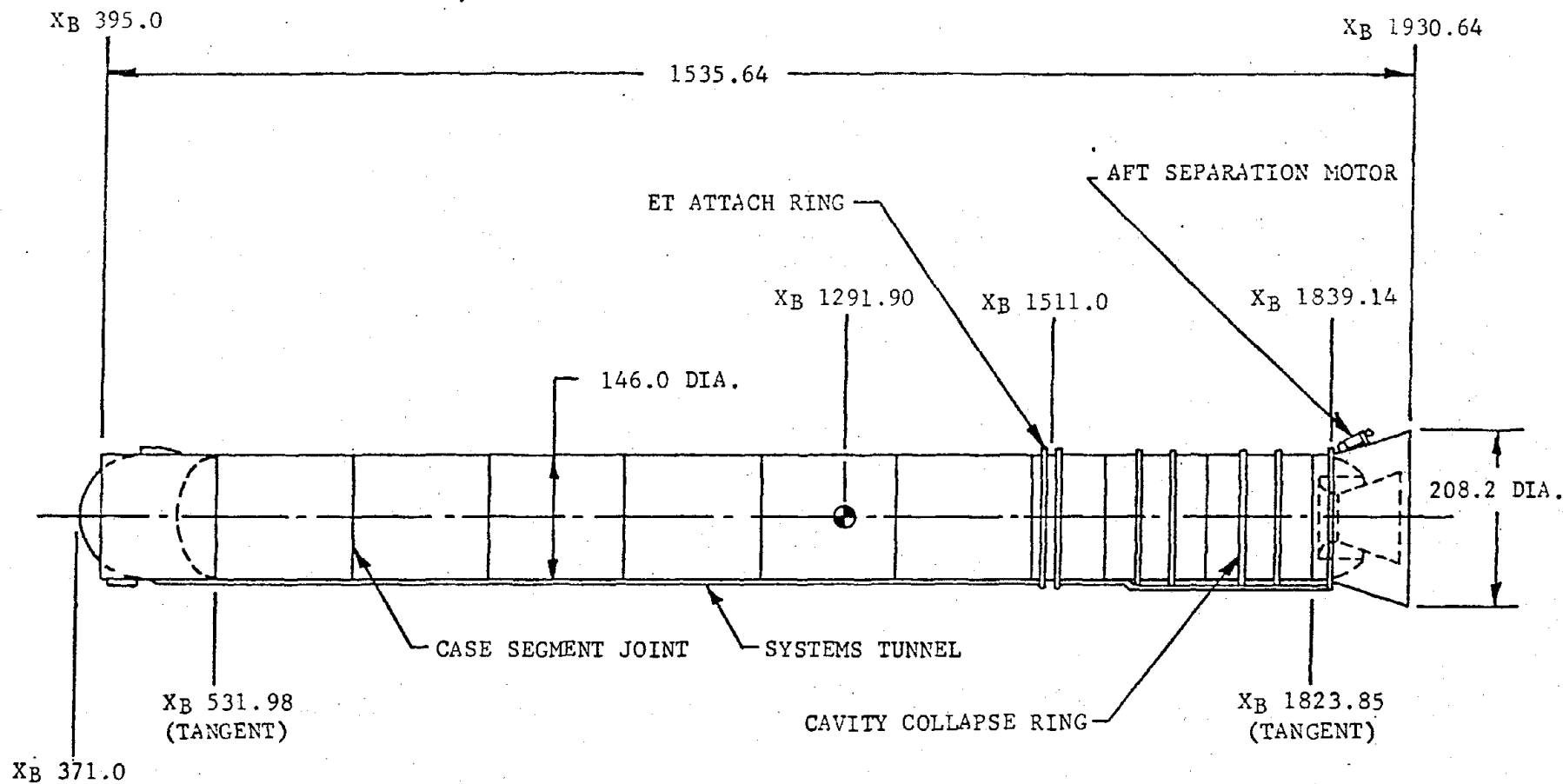
WEIGHT: 190,000 LBS.

PITCH MOMENT OF INERTIA:  $7.2 \times 10^6$  SLUG-FT<sup>2</sup>

FIGURE 2-1. 156 INCH-DIAMETER SRB CONFIGURATION

Weight at Water Impact (Lbs.) 146,365	C.G. Location $X_S = 1252.3$
--	---------------------------------

FIGURE 2-2 Space Shuttle Solid Rocket Booster 4/11/73 Baseline Configuration



**SPLASHDOWN MASS PROPERTIES:**

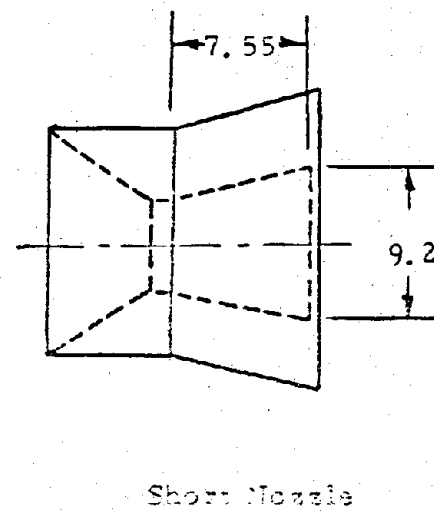
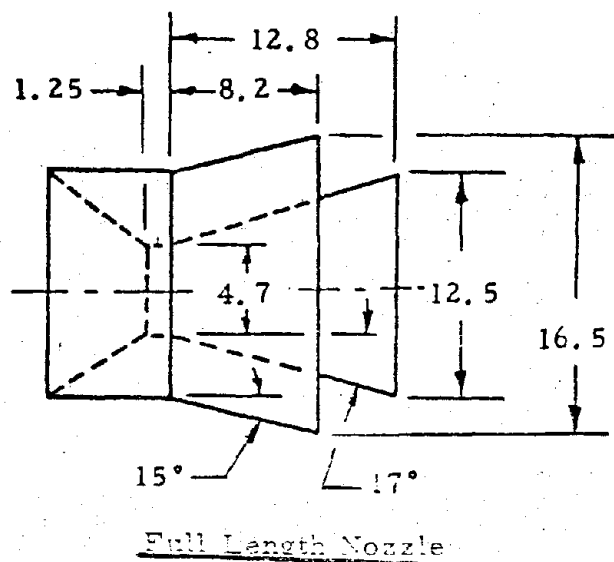
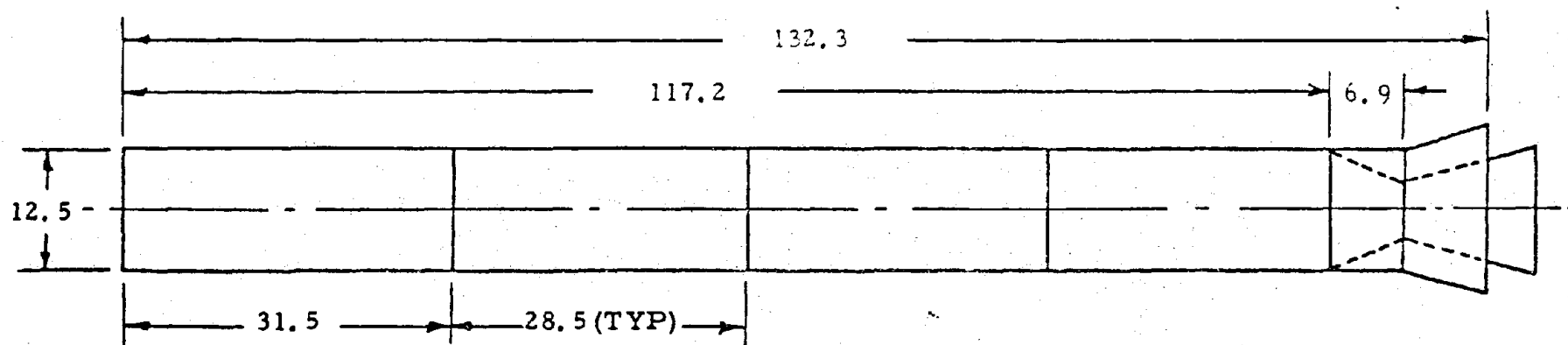
WEIGHT = 158,667 LBS.

PITCH MOMENT OF INERTIA =  $8.318 \times 10^6$  SLUG-FT<sup>2</sup>

FIGURE 2-3 - 11/1/74 BASELINE SRB WATER IMPACT CONFIGURATION



Note: Dimensions are in inches

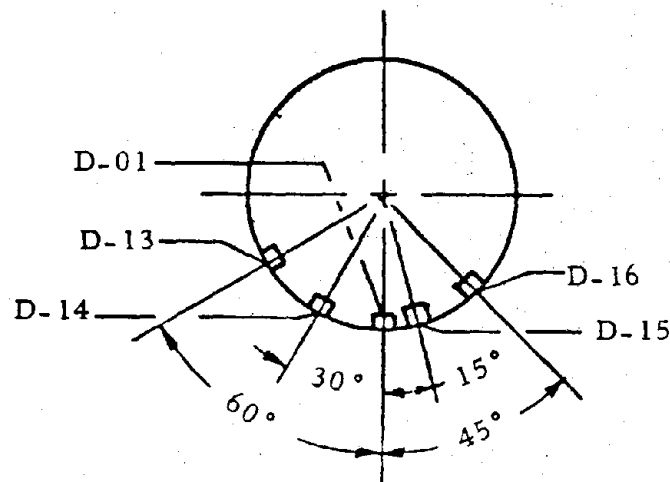
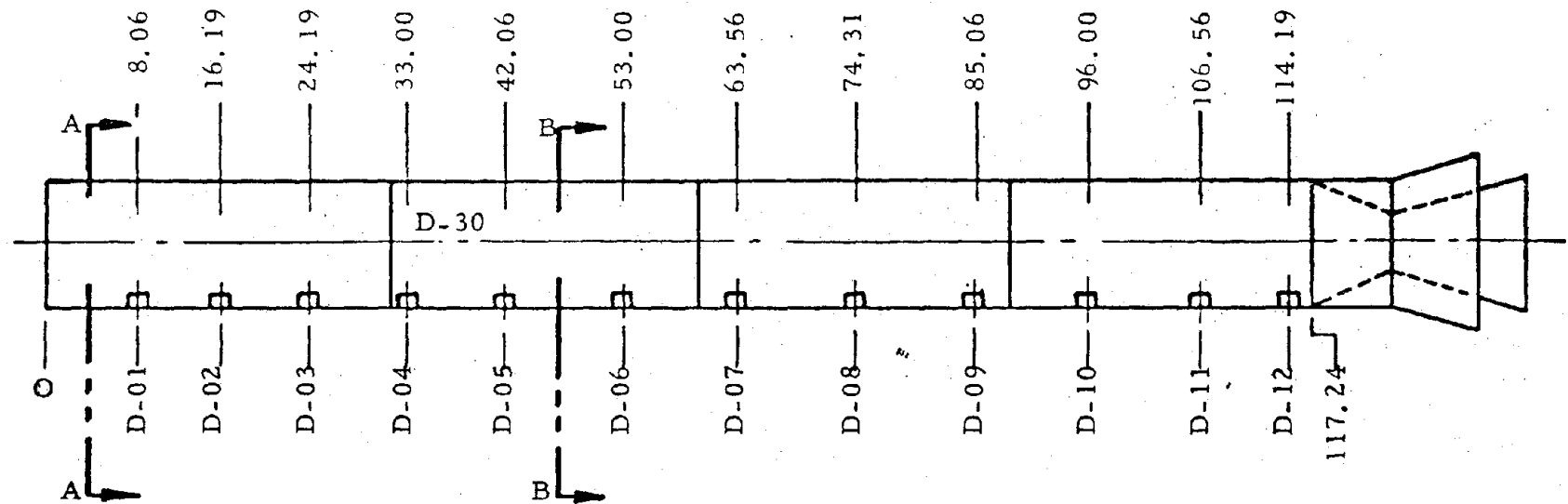


Note

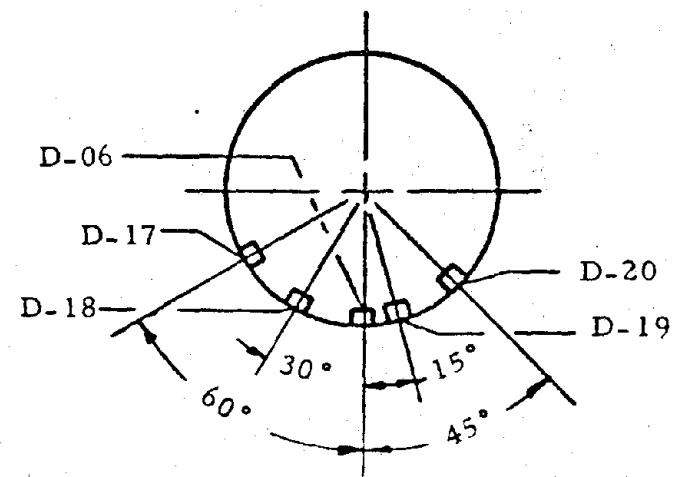
- Weight (lb)  
--Full Length Nozzle = 116  
--Short Nozzle = 114.4
- Model  $I_p$  (Slug-ft<sup>2</sup>)  
--Full Length Nozzle = 33.  
--Short Nozzle = 31.46

FIGURE 2-4. BASIC MODEL, 4-11-73 CONFIGURATION

Note: Dimensions are in inches



Section A-A



Section B-B

FIGURE 2-5 PRESSURE TRANSDUCER LOCATIONS, 4-11-73 CONFIGURATION  
(a) MODEL CYLINDER PRESSURE TRANSDUCERS

Note: Dimensions are in inches

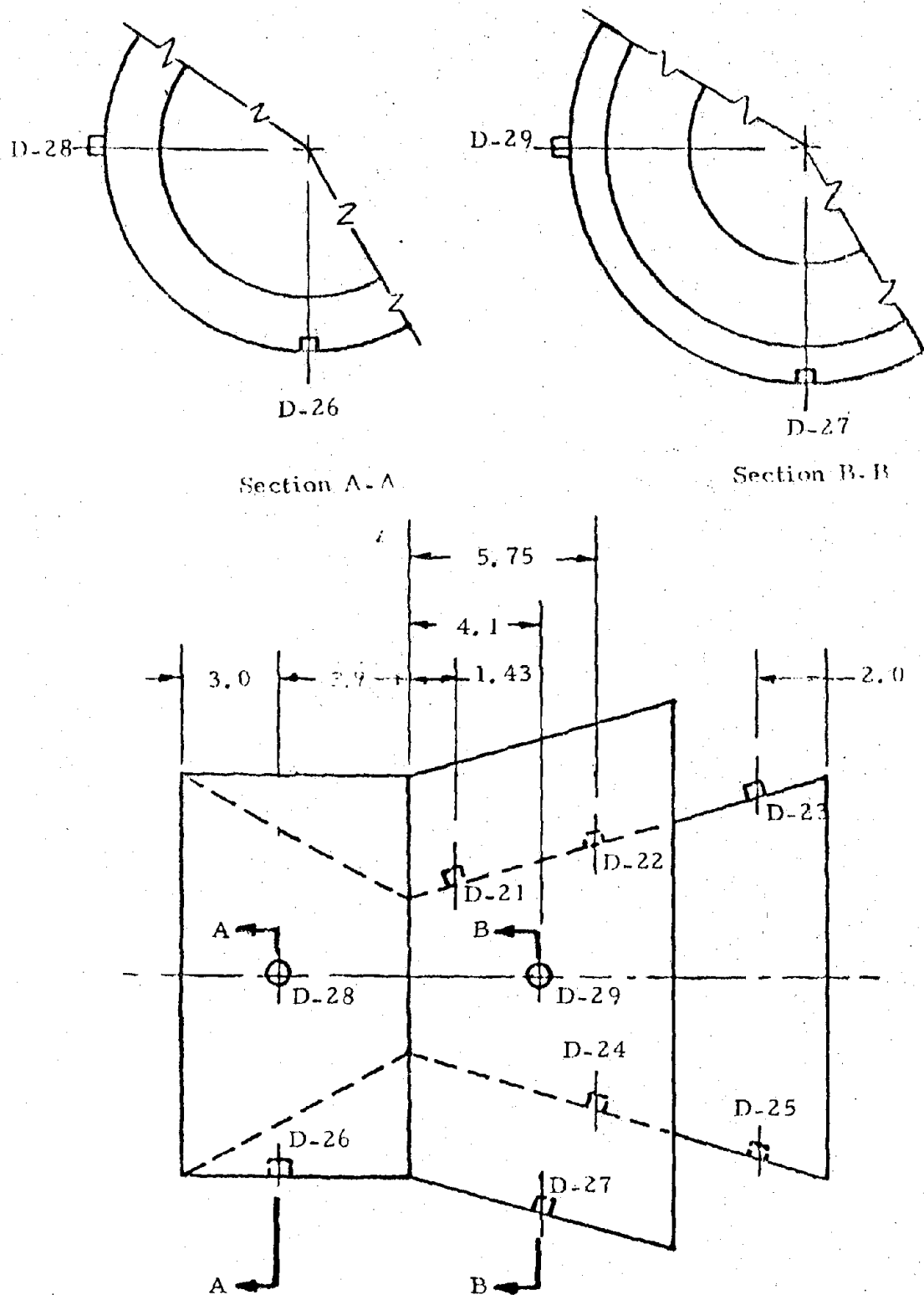


FIGURE 2-5 CONTINUED. (b) FULL LENGTH NOZZLE AND SKIRT PRESSURE TRANSDUCERS

Note: Dimensions are in inches

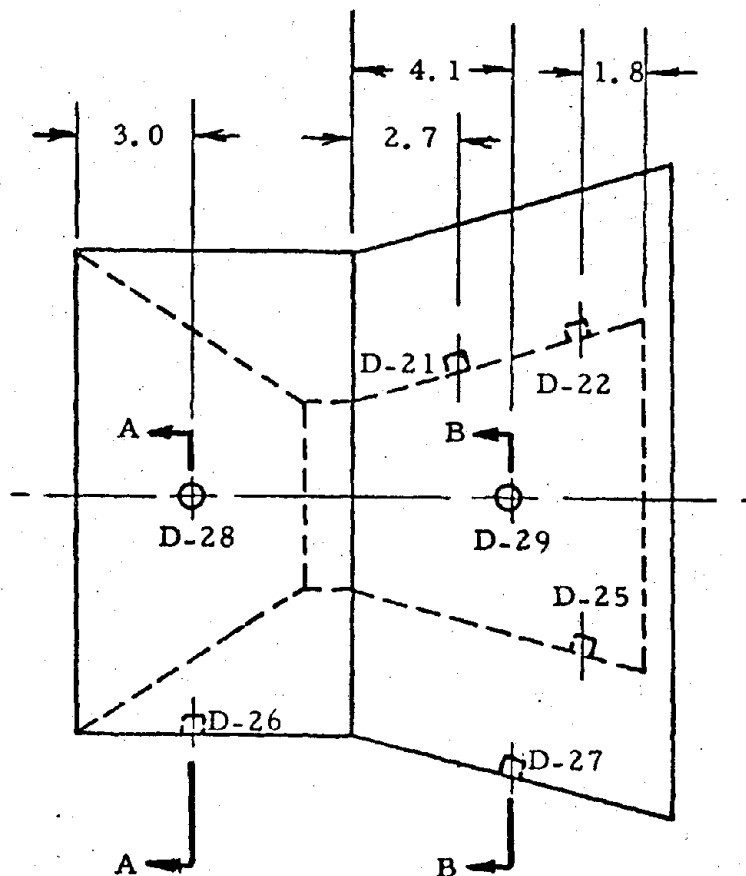
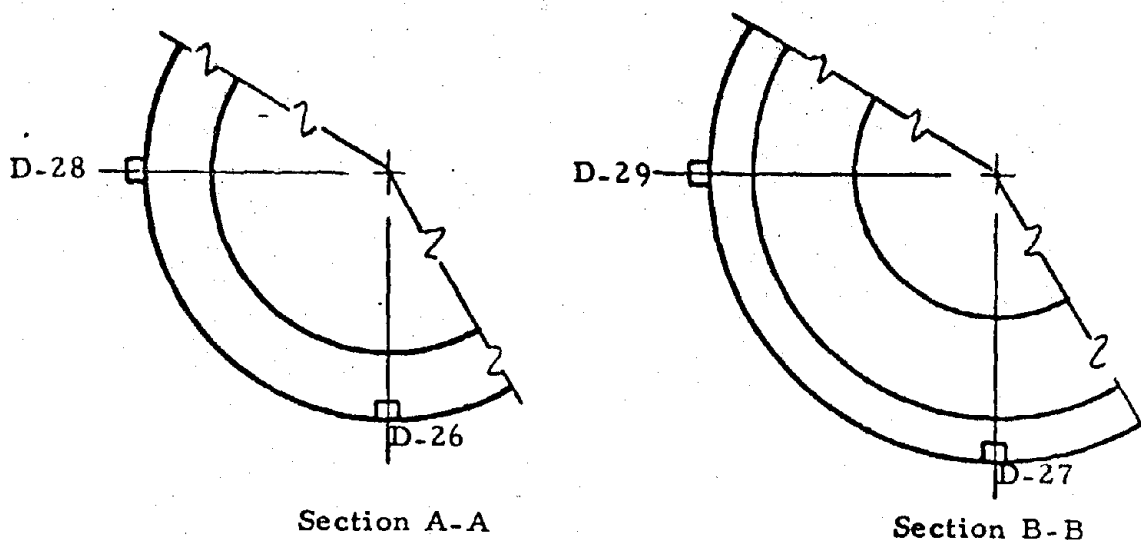


FIGURE 2-5 CONTINUED. (c) SHORT NOZZLE AND SKIRT PRESSURE TRANSDUCERS

Note: Dimensions are in inches

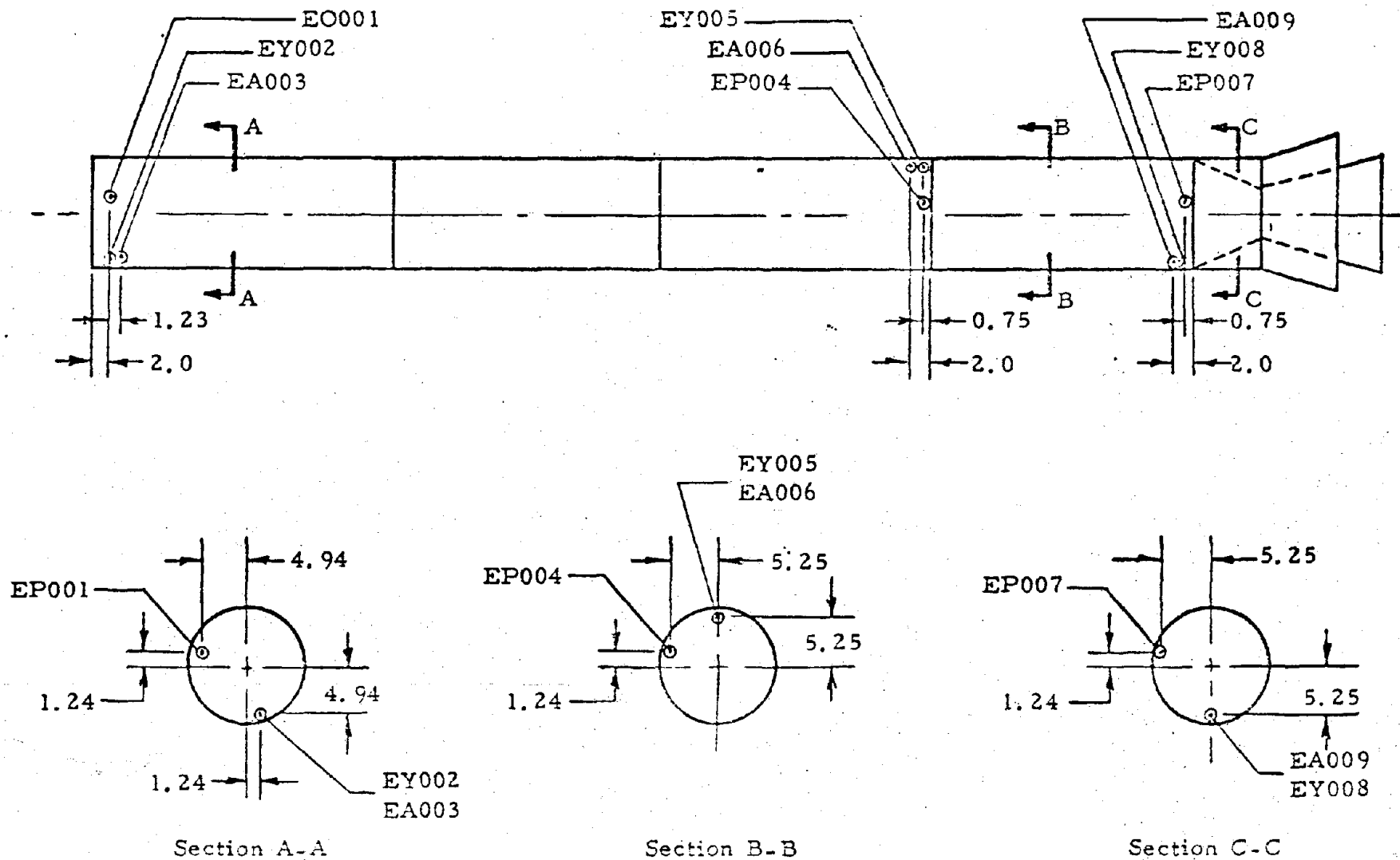


FIGURE 2-6. ACCELEROMETER LOCATIONS, 4-11-73 CONFIGURATION



## SECTION 3.0

### TEST PROGRAM

The test program consisted of a number of drop tests, using the scale models of the SRB described in Section 2.0. The tests were conducted at the NASA/MSFC Over Water Launch (OWL) Tank Facility in Huntsville, Alabama; the Naval Ordnance Laboratory (NOL) Hydroballistics Tank in White Oak, Maryland; The University of New Orleans, New Orleans, Louisiana; and the Long Beach Naval Shipyard (LBNS), Long Beach, California. The drops were made into calm water, in the nose-first and tail-first entry modes; impact conditions varying with entry velocity and pitch angle. Definition of the entry parameters is illustrated in Figure 3-1. The test program consisted of eight series of tests, conducted in the following chronological order:

#### 3.1 Test Series C-143

These were the initial tests of the program and were conducted in the OWL tank during the period November 1972 to April 1973, in accordance with the requirements of Reference 9. A total of 114 tests were conducted, using a 12.5 inch-diameter model of the 156 inch-diameter SRB configuration. The objectives of these tests were to evaluate entry modes, flotation attitudes, penetration characteristics, fundamental loads. Nose-first and tail-first entry modes were investigated, with impact conditions covering the full-scale range of vertical velocity,  $V_V = 80$  to 120 ft/sec, horizontal velocity,  $V_H = 0$  to 50 ft/sec, and pitch angle,  $\theta = 0$  to  $30^\circ$  (Fig. 3-1). The test matrix is shown in

Table 3-1. A detailed description of the tests is presented in Reference 4.

### 3.2 NOL Series #1207

This test program was conducted in the NOL Hydroballistics Tank during February 1973. A 12.5 inch-diameter model of the 156 inch-diameter SRB was used for the test. The program consisted of 37 drops with each impact condition tested twice, once at atmospheric pressure and once at a scaled atmospheric pressure of 1.53 psia. The objectives of this test were to evaluate the effects of pressure scaling on an open end model configuration and to provide data for comparison with the 120 inch-diameter model being tested at LBNS. All drops were conducted with a tail first water entry mode with impact conditions covering the full scale range of vertical velocity,  $V_v = 40$  to 100 FT/SEC, horizontal velocity,  $V_H = 0$ , and pitch angle,  $\theta = 0$  to  $30^\circ$ . The test matrix is shown in Table 3-2. A detailed description of the test is presented in Reference 5.

### 3.3 Test Series C-145

These tests were conducted at the LBNS facility during the period February 10 - March 10, 1973, in accordance with the requirements of Reference 6. A total of 22 tests were conducted, using a 120 inch-diameter model of the 156 inch diameter SRB configuration. In addition to the fundamental objectives of the earlier test series, these tests were conducted to verify scaling relationships. All tests were in the tail-first entry mode, with  $V_v = 8$  to 80 ft/sec,  $V_H = 0$  and  $\theta = 10$  to  $30^\circ$ . The test



matrix is shown in Table 3-3. A detailed description of these tests is presented in Reference 7.

#### 3.4 Test Series P-015

These tests were conducted in the OWL tank during the period July 1-27, 1973, in accordance with the requirements of Reference 16. A total of 127 tests were conducted, using a 12.5 inch-diameter model of the 4-11-73 baseline configuration (with and without nozzle extension), to evaluate the effects of drift velocity and the updated SRB configuration. The tail-first entry mode was investigated, with  $V_V = 80$  to  $120$  ft/sec,  $V_H = 0$  to  $60$  ft/sec and  $\theta = 0$  to  $\pm 30^\circ$ . The test matrix is shown in Table 3-4. A detailed description of these tests is presented in Reference 17.

#### 3.5 Test Series P-022

These tests were conducted in the NOL tank during the period September 9-19, 1973, in accordance with the requirements of Reference 18. A total of 30 tests were conducted, 22 of them at scaled atmospheric pressure (1.29 psia). The model used was the same as for the P-015 tests, except that it was modified to include a hemispherical bulkhead. The primary objective of the tests was to evaluate the effects of pressure scaling. The tail-first entry mode was investigated with the same range of impact conditions as for the P-015 tests, except that wind drift velocity was not simulated (i.e.,  $V_H = 0$ ). The test matrix is shown in Table 3-5, and a detailed description of the tests is presented in References 19 to 21.

### 3.6 Test Series P-029

These tests were conducted in the OWL tank during the period November 9-20, 1973. A total of 47 tests were conducted over the same range of impact conditions as for the P-022 tests. All tests were with tail-first entry, using the short-nozzle configuration of the P-022 model, modified to include an elliptical bulkhead and a baffle in the nozzle-skirt annulus region. The objectives of these tests were to evaluate the effectiveness of the baffle to shield the bulkhead region and to study lee-side cavity collapse pressures. The test matrix is shown in Table 3-6, and a detailed description of the tests is presented in Reference 22.

### 3.7 Test Series TMS-333

Water impact tests using a 12.5 inch scale model of the 11/1/74 configuration Space Shuttle Solid Rocket Booster were conducted during October 1974 at the Naval Surface Weapons Center, White Oak, Maryland in accordance with the requirements of Reference 25. The objective of this test program was to measure accelerations, forces, and pressures imparted to the SRB Model during the initial impact, cavity collapse, and slapdown phases of water entry.

A total of 69 tail first drops were made during this test. Model entry conditions simulated full scale vertical velocities of 80 and 100 ft/sec with horizontal drift velocities up to 45 ft/sec and impact angles over a  $\pm 10^\circ$  range. These tests were conducted at both ambient and scaled atmospheric pressures. The test matrix is shown in Table 3-7 and a detailed description of the test is presented in Reference 26.

### 3.8 Test Series UNO-1

Water impact tests using a fore-shortened 12.5 inch diameter model simulating the aft cylinder and nozzle/skirt geometry of the 11/1/74 and 5/1/75 configurations of the Space Shuttle Solid Rocket Booster were conducted during September 1975 at the University of New Orleans School of Engineering Hydrodynamics Tank, New Orleans, Louisiana in accordance with the test plan of Reference 28. The objective of this program was to evaluate changes in nozzle loads for the 5/1/75 configuration due to the addition of the compliance ring and a one-foot extension of the nozzle, and to substantiate the analytically defined increase of nozzle loads of the 5/1/75 baseline update.

A total of 49 drops were made with five geometric configurations. Model entry conditions simulated full scale vertical velocities of 70, 80, and 90 FPS with water impact angles of 0, 5, and 10 degrees. Horizontal drift velocity was not simulated in this test which was conducted at atmospheric pressure. The test matrix is shown in Table 3-8 and a detailed description of the test is presented in Reference 29.

TABLE 3-1

## TEST MATRIX - TEST SERIES C-143

		$\phi^*=0^\circ$							$V_H = 0 \text{ FPS}$						
VV FPS	VH FPS	$\theta$							$\phi^*$	$\theta=10^\circ$			$\theta=20^\circ$		
		-20°	-10°	0°	10°	20°	30°	90°		$V_V=80$	$V_V=100$	$V_V=120$	$V_V=80$	$V_V=100$	$V_V=120$
10	0							X	0°	X	X	X	X	X	X
20	0			X	X	X	X	X	22.5°	X	X	X	X	X	X
	25								45°	X	X	X	X	X	X
	50			X		X			67.5°	X	X	X	X	X	X
40	0			X	X	X	X		90°	X	X	X	X	X	X
	25	X	X	X	X	X			112.5°	X	X	X	X	X	X
	50	X	X	X					135°	X	X	X	X	X	X
60	0			X	X	X	X		157.5°	X	X	X	X	X	X
	25	X	X	X	X	X			180°	X	X	X	X	X	X
	50	X	X	X	X	X									
	0			X	X	X	X								
80	25	X	X	X	X	X									
	50	X	X	X	X	X									
100	0			X	X	X	X								
120	0			X	X	X	X								

$*\phi$  DENOTES MODEL ROLL ANGLE

\* $\phi$  DENOTES MODEL ROLL ANGLE

TABLE 3-2

TEST MATRIX NOL SERIES #1207

P PSIA	$\phi$ DEG°	V <sub>V</sub> FT/SEC	$\theta$			
			0°	10°	20°	30°
14.7 ↓	0° ↓	40	X	X	X	X
		60	X	X	X	X
		100	X	X	X	X
	45° ↓	40				
		60		X	X	X
		100		X	X	
1.53 ↓	0° ↓	40	X	X		
		60	X	X	X	X
		100	X	X	X	X
	45° ↓	40				
		60		X	X	X
		100		X	X	X
2.5	0°	60	X			
4.0	↓	↓	X			
8.0	↓	↓	X			

TABLE 3-3

## TEST MATRIX - TEST SERIES C-145

V <sub>V</sub> FPS	REINFORCED NOZZLE EXTENSION			STANDARD NOZZLE EXTENSION			NO NOZZLE EXTENSION		
	10°	20°	30°	10°	20°	30°	10°	20°	30°
10	X	X	X		X				
20	X	X	X						
40	X	X	X				X	X	
60	X	X		X	X	X		X	
80	X				X				

TABLE 3-4a

TEST MATRIX - TEST SERIES P-015  
WITH NOZZLE EXTENSION

V <sub>V</sub> FPS	V <sub>H</sub> FPS	$\theta$					
		-20°	-10°	0°	10°	20°	30°
60	0			X*	X*	X*	X*
	30			X			
	60						
80	0			X*	X*	X*	X*
	30	X	X	X	X	X*	
	60	X	X	X	X	X	
100	0			X*	X*	X*	X*
	30	X	X	X	X	X*	
	60	X	X	X	X	X	
120	0			X	X*	X*	X*
	30	X	X	X	X	X*	
	60	X	X	X	X	X	

\* Model rolled 180°

TABLE 3-4b

TEST MATRIX - TEST SERIES P-015  
WITHOUT NOZZLE EXTENSION

V <sub>V</sub> FPS	V <sub>H</sub> FPS	$\theta$				
		-20°	-10°	0°	10°	20°
80	0	X	X	X		
	30	X	X	X	X	X*
	60	X	X	X	X	X*
100	0	X	X	X		
	30	X	X	X	X	X*
	60	X	X	X	X	X*
120	0	X	X	X		
	30	X	X	X	X	X*
	60	X	X	X	X	X*

\*Model rolled 180°.



TABLE 3-5

TEST MATRIX - TEST SERIES P-022  
WITH NOZZLE EXTENSION

Pa PSIA	Vv FPS	$\theta$			
		0°	10°	20°	30°
1.29	80	X	X		X
	100	X			X
	120	X	X	X	X
14.7	80	X			X
	100	X			X
	120				

WITHOUT NOZZLE EXTENSION

Pa PSIA	Vv FPS	$\theta$			
		0°	10°	20°	30°
1.29	80	X	X		X
	100	X	X		X
	120	X	X	X	X
14.7	80	X			X
	100	X			X
	120				

TABLE 3-6

TEST MATRIX - TEST SERIES P-029  
WITH NOZZLE EXTENSION,  $\phi = 180^\circ$

Vv FPS	$\theta$	
	0°	10°
80	X	X
100	X	X
120	X	X

WITHOUT NOZZLE EXTENSION,  $\phi = 180^\circ$

Vv FPS	$\theta$				
	0°	5°	10°	15°	30°
80	X	X	X	X	
100	X	X	X	X*	X*
120	X	X	X	X*	X*

\*Model rolled 90°

WITHOUT NOZZLE EXTENSION, WITH BAFFLE,  $\phi = 0^\circ$

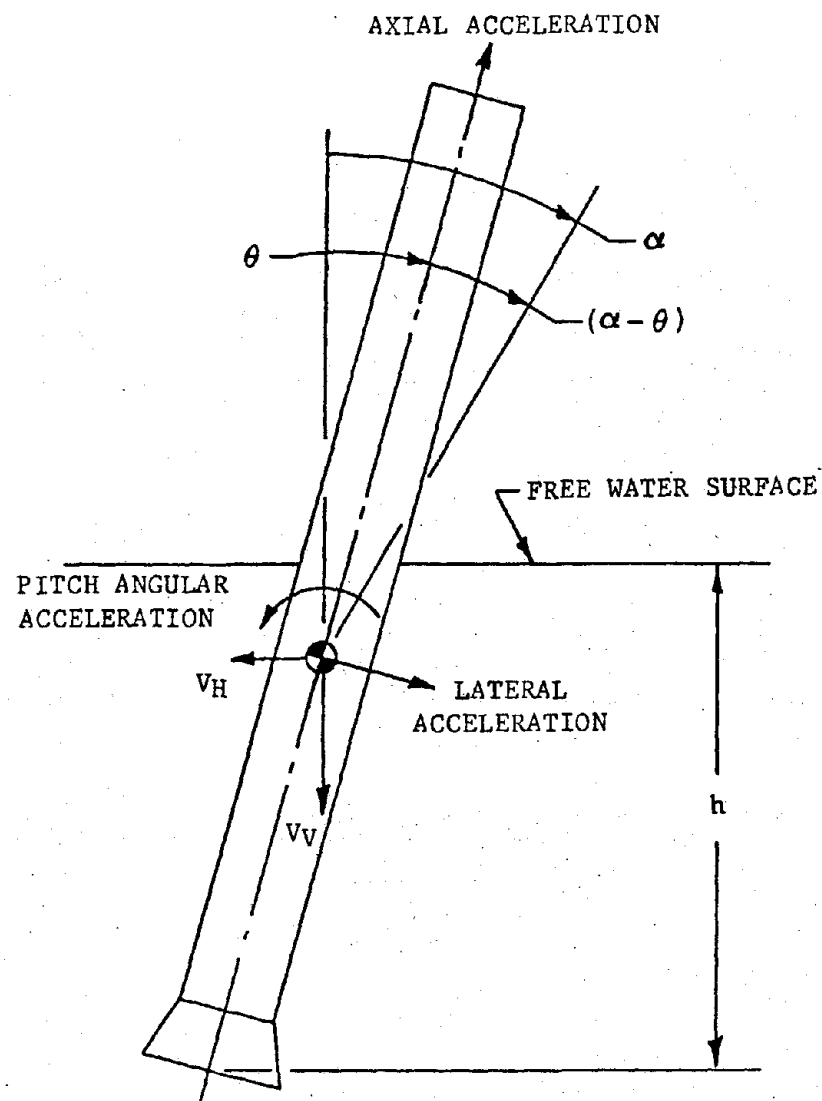
Vv FPS	$\theta$			
	0°	10°	20°	30°
80	X	X	X	X
100	X	X	X	X
120	X	X	X	X

TABLE 3-7  
DROP NUMBER MATRIX NOL TEST TMS-333

$V_V$	$V_H$	$P_\infty$	$\phi$	$\theta_i$				
				$-10^\circ$	$-5^\circ$	$0^\circ$	$+5^\circ$	$+10^\circ$
80	0	14.7	0	X	X	X		
	15		↓	X				
	30		↓			X		
	45		↓	X	X	X		
	0		120	X	X			
	15		↓					
	30		↓					
	45	↓	↓		X			
	0	1.26	0	X	X	X		
	15		↓		X	X	X	X
	30		↓			X	X	X
	45		↓				X	X
	0		120	X	X			
	15		↓		X	X	X	X
	30		↓					
↓	45	↓	↓					
100	0	14.7	0	X	X	X		
	15		↓	X				
	30		↓			X		
	45		↓	X	X	X		
	0		120	X	X			
	15		↓					
	30		↓					
	45	↓	↓		X			
	0	1.26	0	X	X	X		
	15		↓		X	X	X	X
	30		↓			X	X	X
	45		↓				X	X
	0		120	X	X			
	15		↓		X	X	X	X
	30		↓					
↓	45	↓	↓				X	X

TABLE 3-8 TEST MATRIX - TEST SERIES UNO-1

MODEL CONFIGURATION	MODEL SCALE VERTICAL VELOCITY FT/SEC	FULL SCALE VERTICAL VELOCITY FT/SEC	INITIAL IMPACT ANGLE		
			0	5°	10°
A	20.5	70	X	X	X
	23.4	80	X	X	X
↓	26.3	90	X	X	X
B	20.5	70	X	X	X
	23.4	80	X	X	X
↓	26.3	90	X	X	X
C	20.5	70	X	X	X
	23.4	80	X	X	X
↓	26.3	90	X	X	X
D	20.5	70	X	X	X
	23.4	80	X	X	X
↓	26.3	90	X	X	X
E	20.5	70	X	X	X
	23.4	80	X	X	X
↓	26.3	90	X	X	X



$V_V$  - VERTICAL VELOCITY

$V_H$  - HORIZONTAL VELOCITY

$\theta$  - PITCH ANGLE

$\alpha$  - FLIGHT PATH ANGLE

$(\alpha - \theta)$  - EFFECTIVE IMPACT ANGLE

$h$  - PENETRATION DEPTH

NOTE: ALL VALUES POSITIVE AS SHOWN

FIGURE 3-1 SRB WATER IMPACT LOADS COORDINATE SYSTEM



## SECTION 4.0

### DATA ACQUISITION AND PROCESSING

A wire cable was provided to carry the transducer signals from the onboard signal conditioner to an instrumentation trailer for recording on analog magnetic tape. The cable consisted of five wires to transmit power, electrical calibrations, and three multiplexed data signals. It was attached to the model near the C.G. and was dropped with and alongside the model during testing to minimize forces applied to the model by the cable. In the instrumentation trailer, seven tape tracks were used to record three multiplexed data signals, a 50 KC tape speed compensation signal, model release signal, IRIG-B time, and a voice signal.

Prior to each test, with model suspended above the water, calibration resistors were shunted across all transducers and pretest calibrations taken. After recording data during the test, post test calibrations were performed in a similar manner with the model in calm water. After each test, the data tape was played back through a demodulator and recorded on oscillograph charts. The oscillographs were then examined for data quality, polarity, and IRIG-B time. Based on the results of this examination, modifications or improvements to the instrumentation were made as required prior to subsequent testing.

The analog tape was then sent to the MSFC Computation Laboratory for digitizing and plotting. The tape was played back, one data track at a time, with the multiplexed signals passing through tuners with individual frequencies corresponding to the center frequencies of the multiplex channels. Thus, the original multiplex signal was separated into 21 individual signals.

These signals were then fed through a low pass filter (100 cps for test series TMS-333 and 220 cps for all others) into a discriminator which measured the deviation from center frequency and assigned to it a four digit magnitude. Digitizing was carried out at the rate of 1000 samples per second. The computer then read each discriminator in sequence, recycling to repeat the process for the next millisecond in time. Computer time required for one complete set of readings was approximately 8 microseconds.

During the digitizing, the computer tracked the 50 KC reference signal, adjusting time to compensate for any minute variations in speed of the tape transport of the original analog data recorder. Overall control of the process was keyed to IRIG-B time. The analog tape was sampled during the pretest calibration, the test (beginning before model release and continuing through slapdown), and the post test calibration. Output from the digitizing computer consisted of a digital tape containing IRIG-B time followed by 44 data points for each measured quantity; each data point corresponding to times one millisecond apart. This format was repeated until all data had been included. The calibrations were then used to express magnitudes of the digitized data in terms of engineering units, and all values were corrected for zero biases.

Finally, the tapes were processed in a merge and reformat program which converted the data to Fortran form and rearranged it on files in a prescribed numerical sequence. A plot tape was generated and time histories of all measured quantities plotted on a Stronberg-Carlson 4020 Plotter. A schematic of the data acquisition and processing system is shown in figure 4-1.



Photographic coverage for the tests was provided by 16 mm high-speed movie cameras. In OWL Test Series P-015, P-029, and C-143, data cameras were mounted above and below the waterline, while split image photography (with the centerline of the camera lens at the waterline) was used in NOL Test Series P-022 and TMS-333. All cameras were above the waterline for LBNS Test Series C-145. In all cases, one camera (or set of cameras) was placed in the model pitch plane, the other perpendicular to it. All were aimed at the impact point. In the LBNS tests, an additional camera was mounted inside the model to record the flow of water through the nozzle.

Camera speed was set at 250 frames per second. Timing lines were recorded on the margin of the film for exact determination of frame speed. A rectangular grid with horizontal and vertical lines one foot on center was photographed on each reel of film to provide a linear distance calibration. Flash bulbs, which illuminated at model release, were placed in the field of view of the cameras to coordinate time with the electrical instrumentation.

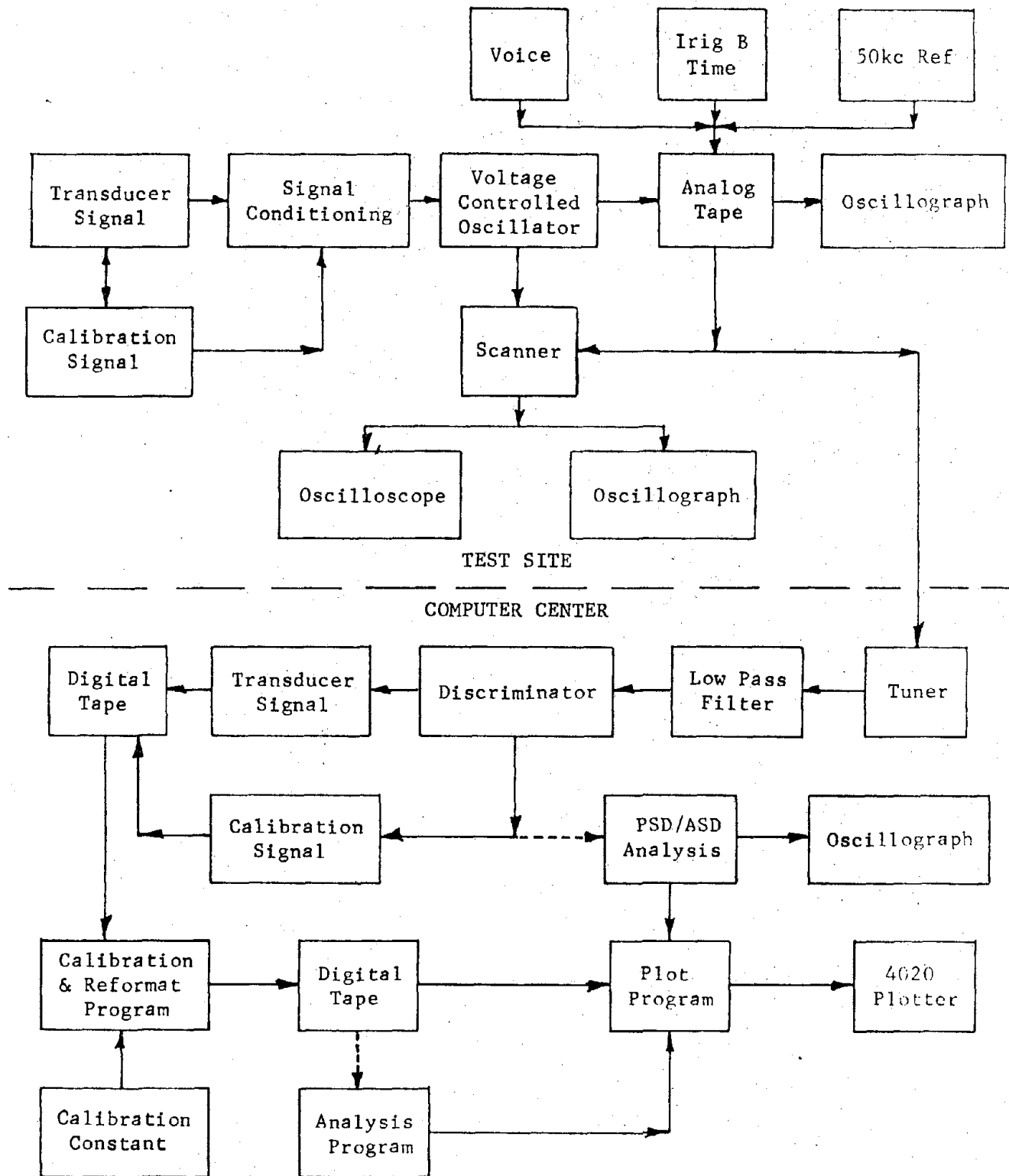


FIGURE 4-1 DATA ACQUISITION AND PROCESSING BLOCK DIAGRAM

## SECTION 5.0

### SRB WATER IMPACT DYNAMIC EVENTS

Water impact of the SRB as revealed by high speed photographic records and measured data from the model tests allows a qualitative description of entry phenomena. This description is best viewed as individual phases consisting of initial entry, cavity formation and collapse, maximum penetration, and rebound and slapdown (Figures 5-1 and 5-2). Within these phases, there are one or more distinct events which establish possible design criteria as indicated below:

<u>Entry Phase</u>	<u>Event</u>	<u>Possible Design Criteria</u>
Initial Entry	Nozzle Toe-in	External Crushing Pressure on Nozzle Keel (Long Nozzle)
	Max. Pitch Acceleration	Normal Load on Nozzle and Skirt, Vehicle Bending Moment, Pressures on Nozzle & Skirt.
	Max. Axial Acceleration	Axial Load on Nozzle, Vehicle Pressure Loads on Nozzle, Skirt
	Annulus Stagnation	Crushing Load on Bulkhead
Cavity Formation & Collapse	Cavity Collapse	Crushing Load on Aft Case & Skirt
Max. Penetration	Max. Penetration	Crushing Load on Aft Case
Rebound and Slapdown	Slapdown	Crushing Load on Forward Case at Various Times ( $t_0$ , $t_1$ , $t_2$ )

#### 5.1 Initial Impact

Nozzle Toe-in. As the vehicle enters the water, there is a very short time interval following initial contact with the liquid free surface during which only a portion of the nozzle extension is wetted. The remainder of the vehicle is dry. For negative impact angles, this wetted portion is on

the keel side of the nozzle. If water entry is accompanied by appreciable horizontal velocity ( $V_H \geq \sim 30$  ft/sec), significant external nozzle keel pressures result and the event is designated as nozzle "toe-in". In this case, the component of fluid velocity normal to the body at impact is maximized. Pressures associated with this flow develop over the nozzle external surface. The flow separates from the internal nozzle surface on the keel side giving rise to near ambient pressure on the nozzle internal surface. As a result, the vehicle is subject to a momentary pitching moment, while the wetted portion of the nozzle extension is subject to a local short-duration compression (buckling) load. Nozzle toe-in, as a distinct event, is observed only with the long nozzle configuration at the relatively high effective impact angles associated with large horizontal velocity and negative impact attitude.

Maximum Pitch Acceleration. As the vehicle penetrates further the increasing flow of water into the nozzle and nozzle-skirt annulus compresses the entrapped air in the motor case chamber. Due to the normal velocity component, the flow is asymmetric, causing a build-up of fluid along the inner walls of the skirt and nozzle on the lee side. The resulting pressure build-up over the external keel and internal lee surfaces producing a considerable normal force and pitching moment on the vehicle. This time is designated the maximum pitch acceleration event.

Maximum Axial Acceleration. Moments later, with continued penetration, the nozzle flows full. Nozzle and skirt internal pressures rise sharply, producing maximum hoop loads and for the configuration without nozzle extension, the nozzle/skirt annulus stagnates by impact of the water head with the motor case aft closure bulkhead. This produces the maximum vehicle axial acceleration event and maximum local pressure loads on most of the appendage structure and subsystem components. The time interval between maximum pitch and

and axial acceleration is a function of effective impact angle, decreasing with decreasing angle until the two events become indistinguishable for near-zero angles.

Annulus Stagnation (With Nozzle Extension). Although the vehicle has lost considerable momentum during the deceleration of initial impact for the configuration with nozzle extension, penetrating velocity is still sufficient to cause flow past the nozzle to separate at the nozzle exit plane. As back pressure builds up in the nozzle-skirt annulus region, the separating free-streamlines from the nozzle exit plane diverge with time. As a result, the flow passage between separating free surface and vehicle skirt continually decreases. About 30 msec. (model scale) after the time of maximum axial acceleration, the separating free streamline has diverged to the point where it encloses the aft rim of the skirt. Therefore, oncoming flow is diverted around the skirt, and flow into the nozzle-skirt annulus is completely cut off. The annular slug of water entrained between the nozzle and skirt continues toward and finally stagnates on the bulkhead. There is a spike in bulkhead pressure with a corresponding spike in axial acceleration, the magnitude of which is much smaller than that of the earlier maximum axial acceleration event for this configuration. The associated loads on the nozzle wall are compressive (buckling) from the throat to the aft end of the skirt and tensile (hoop) from there to the exit plane.

Annulus Stagnation (Without Nozzle Extension)

With continued penetration a quasi-steady state flow is established inside the nozzle and internal pressures drop rapidly. In the nozzle/skirt annulus a cavitating flow has been established along the walls as

a result of wakes from the nozzle compliance ring and the large structural rings inside of the skirt. After the water slug impacts the aft closure, bulkhead pressures begin to decay to approximately 50% of peak value as a pressure wave reflects back through the annulus. Local pressure in the water increases and all internal cavitation collapses. Nozzle, skirt, and bulkhead pressures rise with all areas being subjected to approximately the same pressure which is on the order of  $2/3$  of the peak bulkhead pressure during maximum axial acceleration. In addition to compressive buckling, the stagnation results in a negative nozzle axial load, pulling it away from the bulkhead, due to the stagnation pressure being much larger than the nozzle internal pressures at this time. For some impact conditions the magnitude of the negative nozzle axial force is approximately equal to the positive axial load during maximum axial acceleration.

## 5.2 Cavity Formation and Collapse

For a pure vertical entry, i.e. initial horizontal velocity and pitch angle are zero, the cavity formation and collapse is symmetrical about the vehicle centerline as shown in Figure 5-3. Vertical velocity for the case illustrated is 100 ft/sec., full scale.

During the initial entry phase discussed above, cavity development is very minor. This is due to the fact that the open nozzle or nozzle skirt combination capture most of the stream tube of water with a diameter equal to the exit diameter. The water outside this stream tube diverges very little and enters the nozzle-skirt annulus region. After the nozzle and nozzle/skirt annulus are filled with water and entrapped air (i.e. shortly after the maximum axial acceleration event), the vehicle acts more nearly like a blunt (solid) body and lateral displacement acceleration of the water increases rapidly to

accommodate the penetrating vehicle. As the vehicle continues to penetrate, its velocity decreases and less lateral momentum is imparted to the water. The lateral momentum imparted to the water at the cavity wall is resisted by the difference in pressure across the cavity wall. This pressure difference is a result of hydrostatic pressure in the water and the ambient air pressure in the open cavity. Near the surface this cavity restoring force is very small and the maximum cavity diameter is developed at about one half vehicle diameter below the original water surface. At greater depths, the combination of less lateral momentum imparted to the water (due to reduced velocity) and the greater restoring force on the cavity wall (due to increased hydrostatic pressure) results in smaller maximum cavity diameters. Maximum total cavity volume is developed when the vehicle has penetrated about three vehicle diameters. Beyond this point in the entry, the cavity wall about two vehicle diameters below the water surface begins to close toward the vehicle. The cavity then "collapses" rather uniformly over about two vehicle diameters forward of the aft end of the vehicle skirt. A large amount of air is trapped near the aft skirt and becomes entrained in the water as illustrated. This collapse of the cavity onto the vehicle causes large pressures on the vehicle aft case and skirt. After the "cavity collapse" onto the vehicle, the remainder of the cavity (above about two vehicle diameters below the surface) closes rapidly from the bottom. This vertical closing of the cavity results in a jet of water being created which sprays up from the original entry point.

If there is some horizontal velocity or pitch angle at impact, the cavity formation is similar to the vertical case above but collapses asymmetrically with respect to the vehicle. This is illustrated in figure 5-3 for a case with zero horizontal velocity and a 10 degree pitch attitude at

impact. Vertical velocity is 100 fps in this case also. The water which initially filled the nozzle/skirt annulus can be seen being expelled in the early stages of cavity development. The cavity boundaries are somewhat straighter, in the pitch plane shown, than for the symmetrical entry discussed above. Although the cavity is asymmetric with respect to the vehicle, it is nearly symmetric with respect to the vertical. As the cavity starts to collapse, the keel side cavity wall encounters the vehicle which is also tending to pitch into the cavity wall due to pitch rates induced during initial impact. This event, denoted cavity "wall slap" induces significant pressures locally, but are higher frequency and of lower magnitude than the subsequent "cavity collapse" pressures. The keel side cavity wall washes around the vehicle and the cavity collapses onto itself along a line just off the surface of the vehicle. The collapse line coincides very nearly to a vertical line passing the center of the vehicle base. The collapse is accompanied by local pressures in the vicinity of the collapse line greater than the symmetric case. This is to be expected since the energy due to cavity collapse is now concentrated along a line rather than over the surface of the vehicle.

At initial impact angles greater than about  $10^\circ$ , the maximum pressures and accelerations due to cavity collapse begin to decrease. This is primarily due to the fact that the collapse line described above retains the characteristic of coinciding with a vertical passing through the center of the vehicle base. But at the higher impact angles, the vehicle is at a large angle with respect to this vertical at cavity collapse so that the energy source of cavity collapse is more removed from the surface of the vehicle. Another factor reducing the cavity collapse pressure at the higher impact angles is the lower penetration depth at cavity collapse which reduces the hydrostatic restoring forces on the cavity walls.



### 5.3 Maximum Penetration

After cavity collapse the vehicle continues to penetrate, but at a continually decreasing rate, as it loses momentum due to the combined effects of hydrodynamic drag and bouyancy forces. With hydrostatic pressure in the neighborhood of the nozzle exit increasing with increasing depth, water again flows through the nozzle into the combustion chamber. Chamber pressure rises until the time of "maximum penetration", which is attained about 0.6 sec. (Model scale) after insertion. At this time, the farthest aft point on the vehicle centerline reaches its maximum depth. For reference, maximum penetration depth is 60 to 70 ft., full scale, for zero pitch attitude and horizontal velocity at impact, and vertical velocities of 80 to 120 fps for the configuration with nozzle extension. For the short nozzle configuration, maximum penetration depths are slightly less but only because the reference point is the skirt rather than nozzle exit plane.

### 5.4 Rebound and Slapdown

After the vehicle has lost its penetrating momentum, bouyancy forces predominate. For low effective impact angles ( $\alpha - \theta \cong 0$ ), the bouyancy forces will cause the vehicle to "rebound", i.e., the axial velocity will reverse direction and the vehicle will return along its original entry path for some distance before pitching over and "slapping down" on the water surface. For moderate or high effective impact angles, high pitch rates are induced during the initial impact phase and slapdown occurs while the C.G. is monotonically approaching the water. In the latter case, maximum penetration may be reduced to the order of 30 ft.

During this "slapdown" phase, a sharp pressure pulse runs up the cylindrical body of the vehicle as keel penetrates the free water surface at progressively more forward locations. This pressure pulse takes on maximum values at a point about one-third body length from the nose. At the same time, since the cylinder is driven into the free surface of the water more or less broadside, a cavity is formed circumferentially about the cylinder. The circumferential location of the waterline defining the wetted (loaded) portion of the cylinder varies with axial position along the body, moving from the keel at the spray root location to a position  $90^\circ$  from the keel a short distance aft. Its location along the remainder of the body is effectively unchanged. Since the waterline geometry varies with time, so does the pressure distribution and associated load over the wetted portion of the cylinder defined by this boundary. The separating flow responsible for the lateral cavity collapses rapidly on the vehicle, but with relatively low collapsing pressures as collapse points are at very shallow depths. Slapdown is considered complete when pitch rotational velocity goes to zero as a result of decreased inertial forces and increased buoyancy forward of the vehicle C.G. The final rotational motion is quickly damped out, and the vehicle assumes its equilibrium position. Although some water has been taken on board, it floats in an approximately horizontal flotation attitude. Thereafter, vehicle motion is limited to bobbing in response to perturbations in the water surface, and the water impact is over.

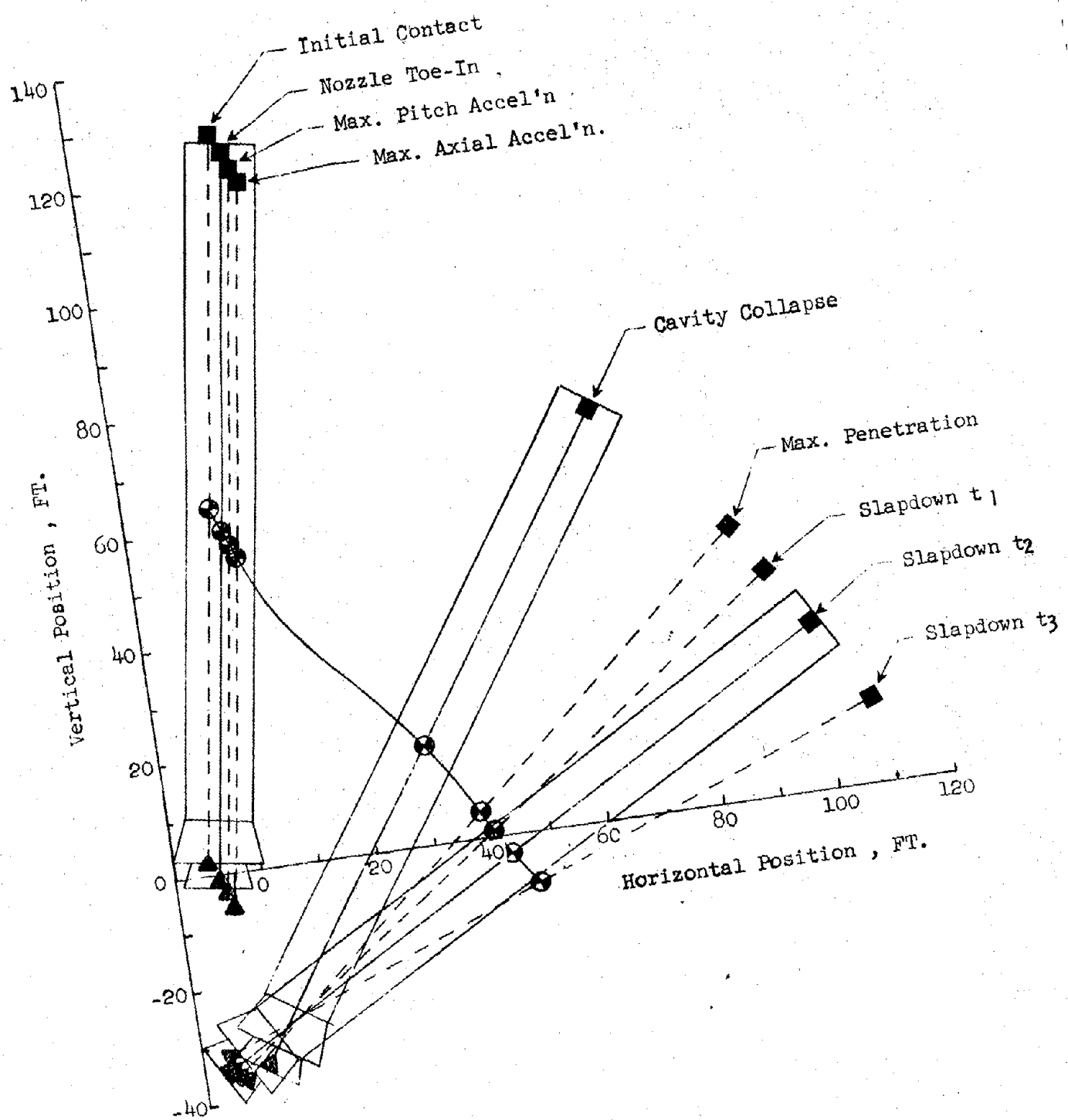


FIGURE 5-1 QUALITATIVE VEHICLE TRAJECTORY DURING IMPACT

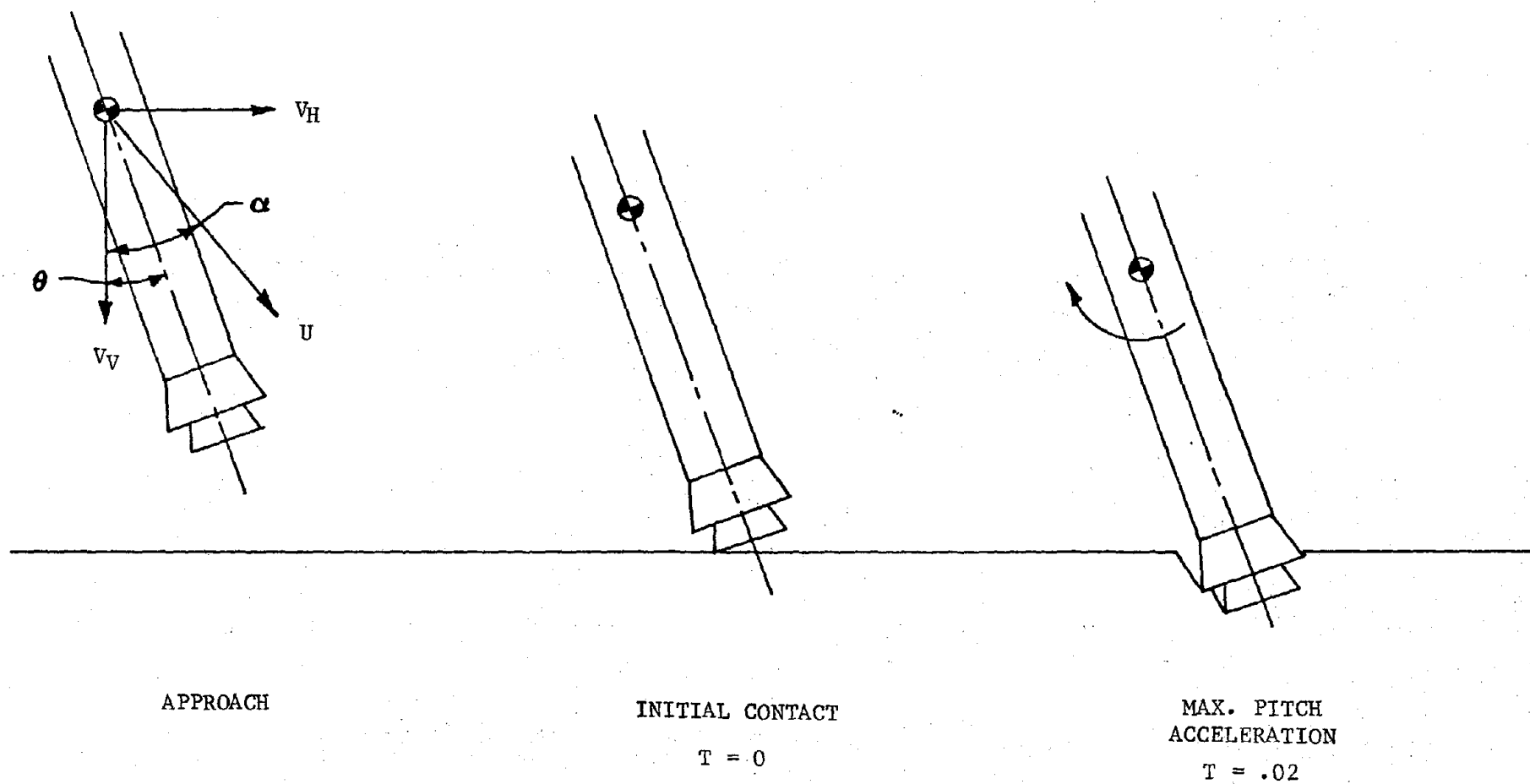


FIGURE 5-2. SRB WATER IMPACT DYNAMIC EVENTS

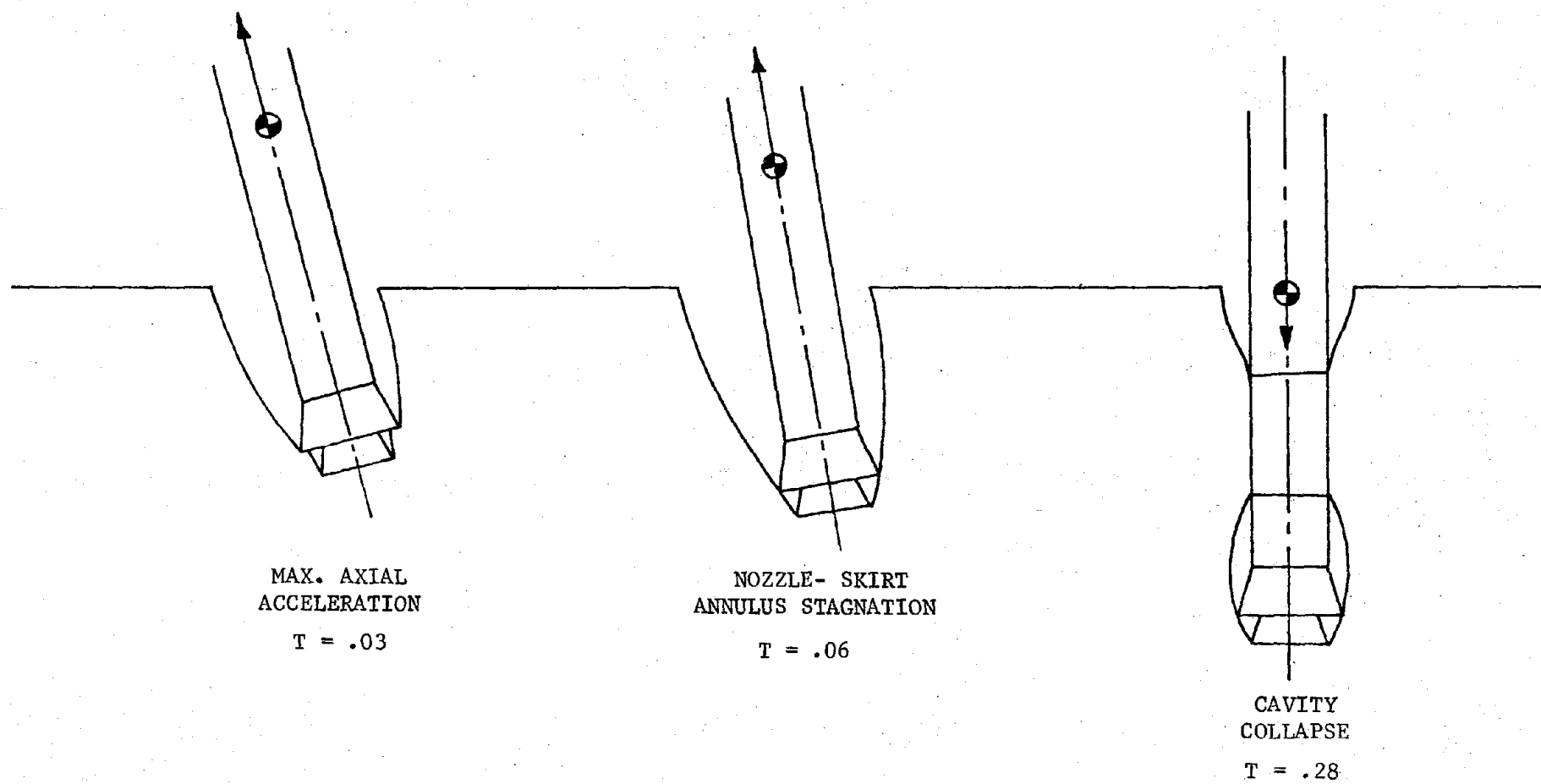


FIGURE 5-2. CONTINUED

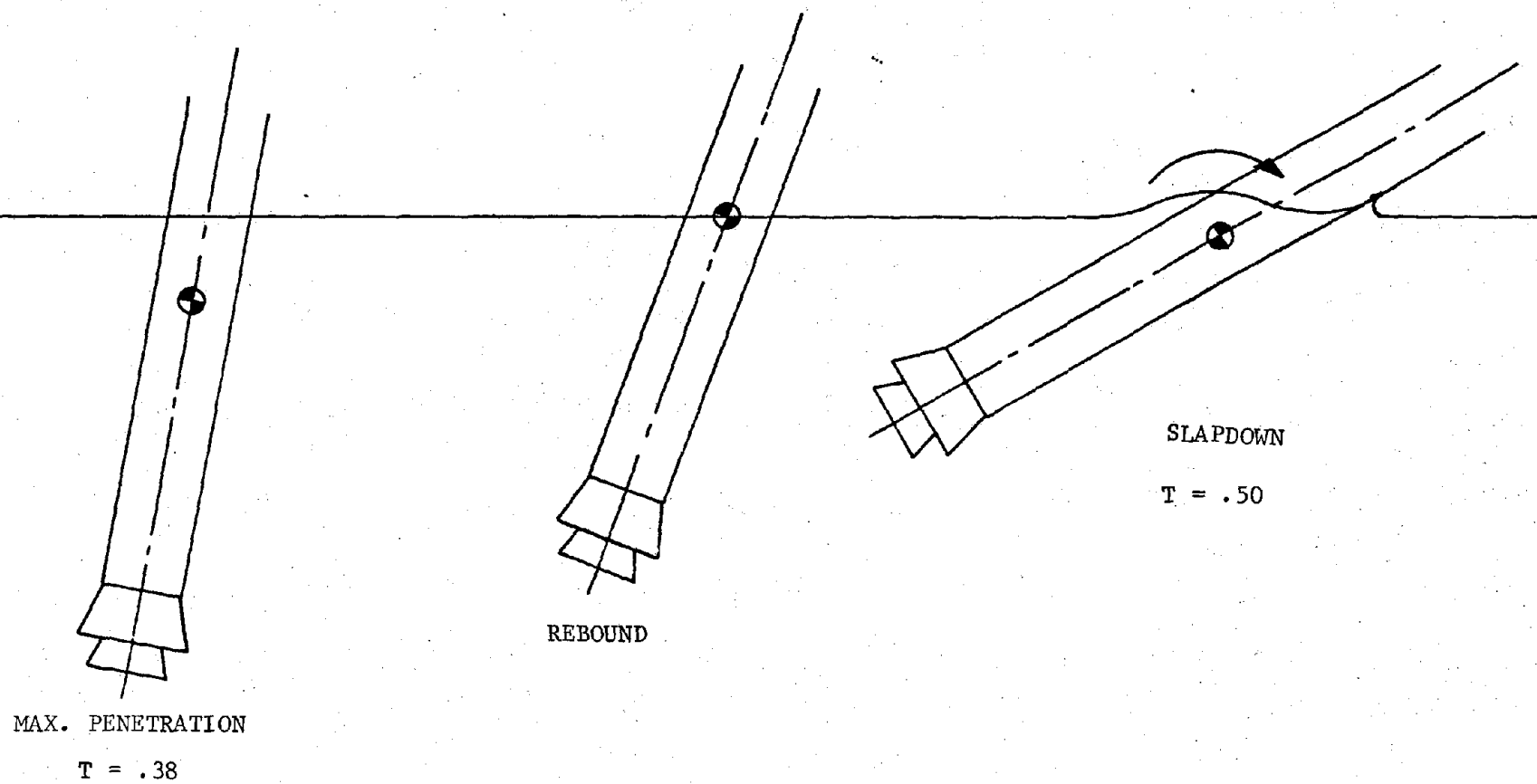
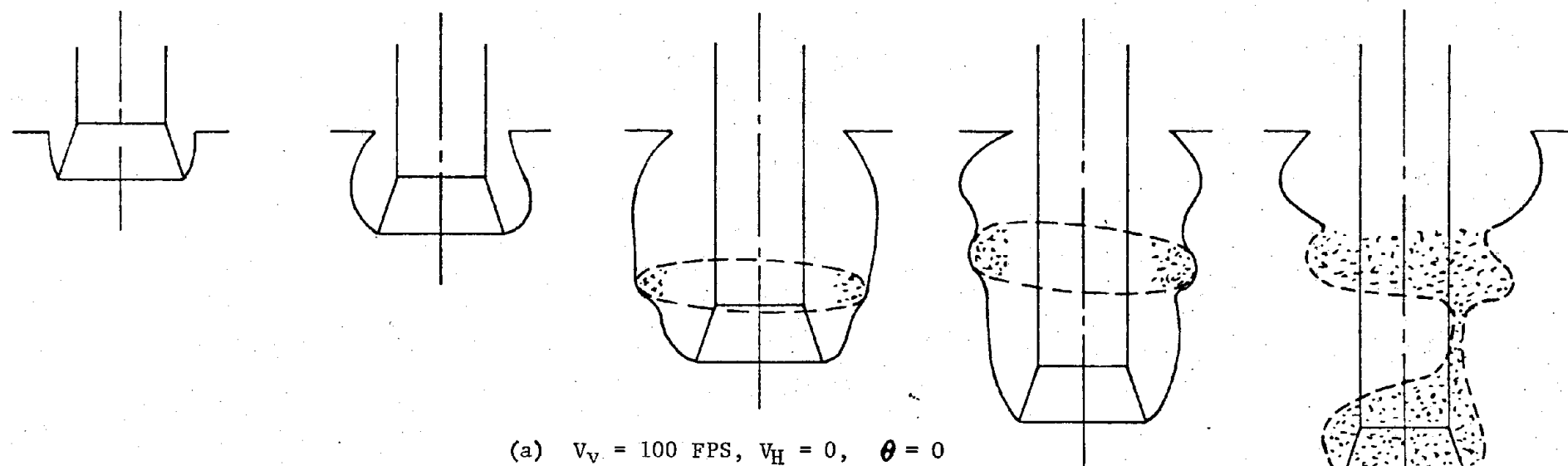
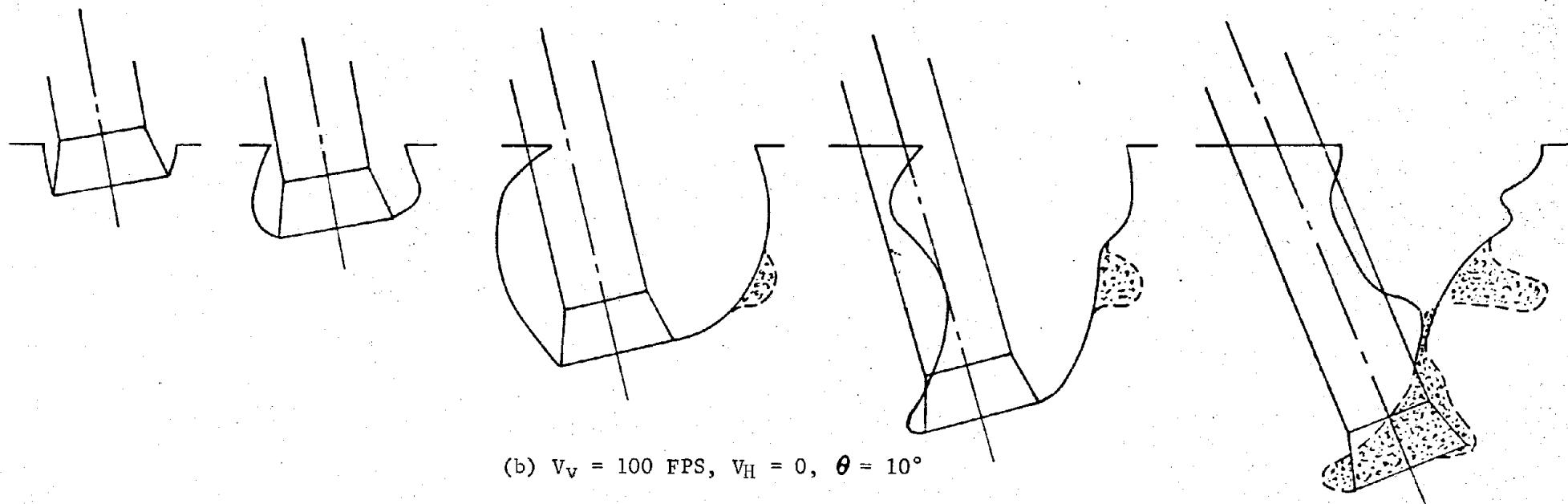


FIGURE 5-2 CONTINUED



(a)  $V_V = 100$  FPS,  $V_H = 0$ ,  $\theta = 0$



(b)  $V_V = 100$  FPS,  $V_H = 0$ ,  $\theta = 10^\circ$

FIGURE 5-3. CAVITY DEVELOPMENT AND COLLAPSE





## SECTION 6.0

### SCALING RELATIONSHIPS

Scale model testing of a prototype vehicle entering a liquid (water) from a gas (air) requires the simultaneous matching of many non-dimensional parameters for a complete simulation of the dynamics of entry. For the configuration and entry conditions of interest here, the most important parameters are the vehicle density relative to the liquid density ( $M/\rho_1 L^3$ ), Froude number ( $F = V_0/\sqrt{Lg}$ ), and Euler number ( $E = p/\rho V^2$ ). Matching of these parameters along with geometric and mass distribution similarity can be accomplished simultaneously in scale model testing in water with ambient air pressure reduced by the scale factor,  $\lambda = L_M/L_p$ . The resulting relationships between the various model and prototype physical quantities are summarized in the table below and are referred to cumulatively as "Froude Scaling".

<u>Physical Quantity</u>	<u>Scale Factor</u> <u>(<math>\frac{\text{Model}}{\text{Prototype}}</math>)</u>
Angle	1
Length	$\lambda$
Area	$\lambda^2$
Weight	$\lambda^3$
Moment of Inertia	$\lambda^5$
Time	$\sqrt{\lambda}$
Linear Velocity	$\sqrt{\lambda}$
Angular Velocity	$1/\sqrt{\lambda}$
Linear Acceleration	1
Angular Acceleration	$1/\lambda$
Pressure	$\lambda$
Force	$\lambda^3$

Other parameters which involve such effects as air and water compressibility, body temperature, and body flexibility are expected to have little effect on loads (pressures, forces and accelerations) and were not simulated. Cavitation number,  $\sigma = \frac{P_a - P_c}{\frac{1}{2} \rho_w V^2}$ , is not expected to be an important parameter although it is matched when testing at reduced ambient pressures. The role of gas to liquid density ratio,  $\rho_g/\rho_l$ , is not fully understood at the present time but it is indicated by Waugh, Ref. 27, that the gas density ratio should be matched in order to model the effect of gas dynamic pressure,  $\frac{1}{2} \rho_g V_g^2$ . The results of Waugh are based on prototype torpedoes with various head shapes at entry velocities of 400 fps as compared to 80-120 fps here, and a mass density of 43 lb/ft<sup>3</sup> as compared to 11 lb/ft<sup>3</sup> for the SRB. Waugh also drew his conclusions from comparisons of trajectories and cavity shapes, whereas we are concerned here primarily with the effect of gas density scaling on maximum cavity collapse pressures. Except for air entrainment, Appendix B indicates Froude and pressure scaling are the prime requirements.

Although Froude scaling is generally accepted for modeling of water entry, no previous testing had been conducted which would establish Froude scaling for configurations and entries typical of the SRB. A test program was conducted, therefore, to verify Froude scaling using a Titan IIIC 120 in. SRB and a 12.5 in. scale model.

Figures 6-1 through 6-8 present comparisons of 12.5 inch and 120 inch diameter scale model data. These comparisons are necessarily limited to nozzle and slapdown pressures for five entry conditions because of the high instrument failure rate in the 120 inch diameter model tests, the accelerometers were inoperative for all drops and approximately 1/2 of the other on-line instruments were damaged or destroyed on each drop. For the presented comparisons, the 12.5 inch data pressures and times were scaled to 120 inch data using the Froude scaling relationships.

Figure 6-1 shows the maximum nozzle pressures for  $V_v = 40$  FT/SEC at  $\theta = 10^\circ$ ,  $20^\circ$ , and  $30^\circ$ , and for  $V_v = 60$  FT/SEC at  $\theta = 10^\circ$ . The data presented are peak values for 120 inch data and 10 millisecond average values for 12.5 inch. The aft nozzle pressure, No. 42, compares well for all conditions, the throat pressure, No. 41, has a tendency to fall off at the higher impact angles.

Figures 6-2 and 6-3 show time history overlay tracing of nozzle pressures for  $V_v = 40$  FT/SEC and  $\theta = 10^\circ$ . The upper plots on each page compare 120 inch data with 12.5 inch data taken at  $P_\infty = 14.7$  psia, the lower plots present the same comparison with the 12.5 inch data taken at  $P_\infty = 1.53$  psia. The first figure, 6-2, presents true value data for both models and the second figure, 6-3, presents 10 millisecond average data for both models. Figures 6-4 and 6-5 show similar plots for an entry condition of  $V_v = 60$  FT/SEC and  $\theta = 10^\circ$ . With the exception of the maximum pressure value at the throat, the 120 inch data compares very well with the 12.5 inch data taken at  $P_\infty = 1.53$  psia. The appearance of the 120 inch scale throat pressure, D21, indicates that it may have been driven into the carrier frequency band edge on the data tape and folded down. This phenomena has been encountered on other test data when the data system voltage controlled oscillators are not tuned to their center frequency and the transducer puts out a high signal level. Referring back to Figure 6-1 for the impact conditions of  $V_v = 40$  FT/SEC and  $\theta = 30^\circ$ , the throat pressure D21 reads 72 psi. It is expected that this pressure would increase at lower impact angles for a given vertical velocity. Also the widely separated double peaks on D21 in figures 6-2 through 6-5 are typical for high impact angles but were not observed on other data for  $\theta \approx 0^\circ$  and  $10^\circ$ .

Figure 6-6 presents comparisons of primary slapdown keel pressures for the 12.5 inch and 120 inch scale models. The data shown is peak value 120 inch data and 10 millisecond average 12.5 inch model data. Figure 6-7 presents time history overlay tracings of peak value slapdown pressures for the two models. Figure 6-8 shows the same comparisons using 10 millisecond average data for both models. The 12.5 inch data is generally higher at the maximum value but it compares very well over the time history of the measurements.

12.5 INCH MODEL DATA ARE SCALED TO 120 INCH MODEL VALUES

□ 12.5 INCH MODEL DATA

○ 120 INCH MODEL DATA

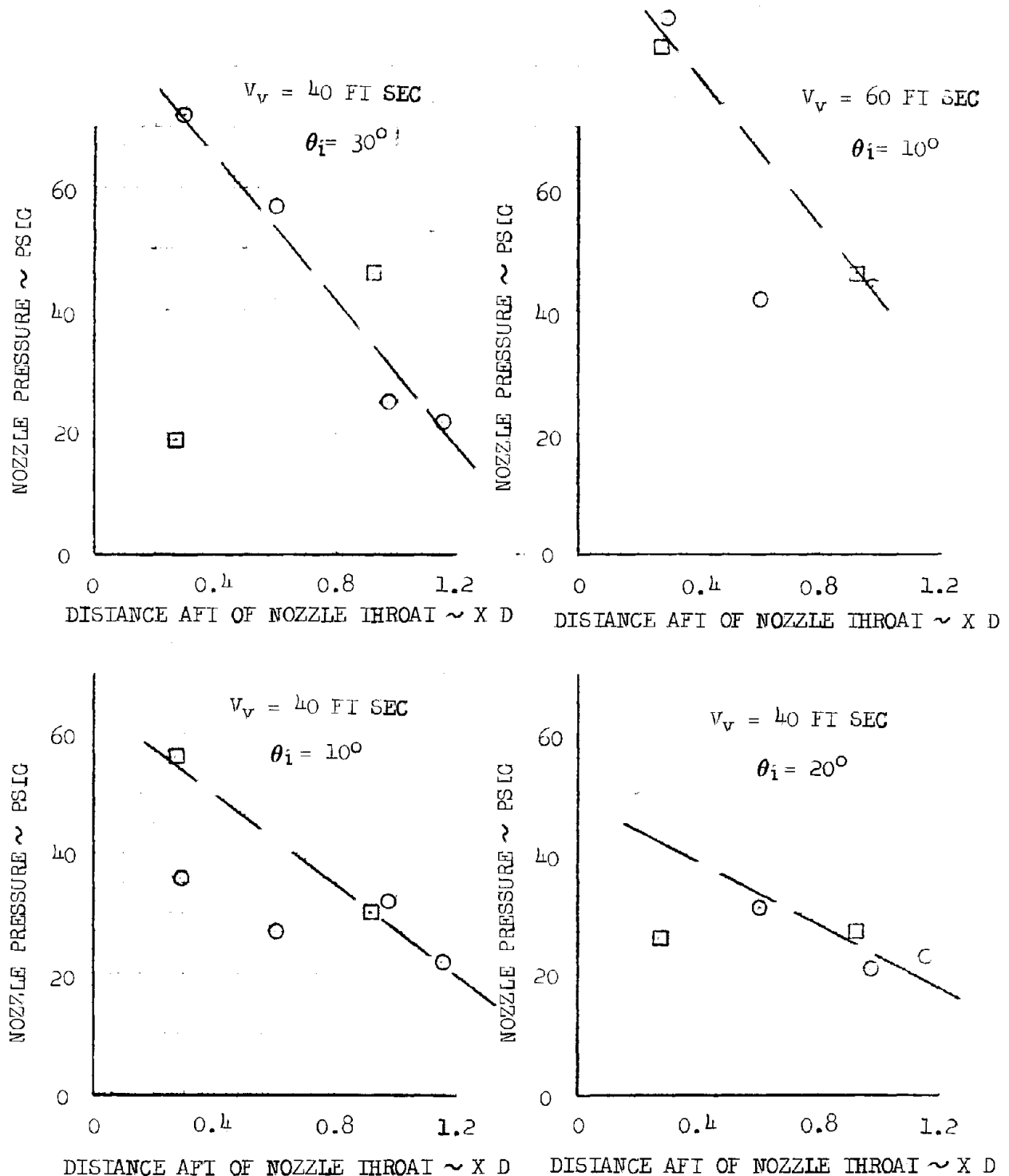


FIGURE 6-1 COMPARISON OF 12.5 INCH AND 120 INCH DIAMETER MODEL PEAK INTERNAL NOZZLE PRESSURES

REPRODUCIBILITY OF THE  
ORIGINAL PAGE IS PROVEN

12.5 INCH MODEL DATA ARE SCALED TO 120 INCH MODEL VALUES

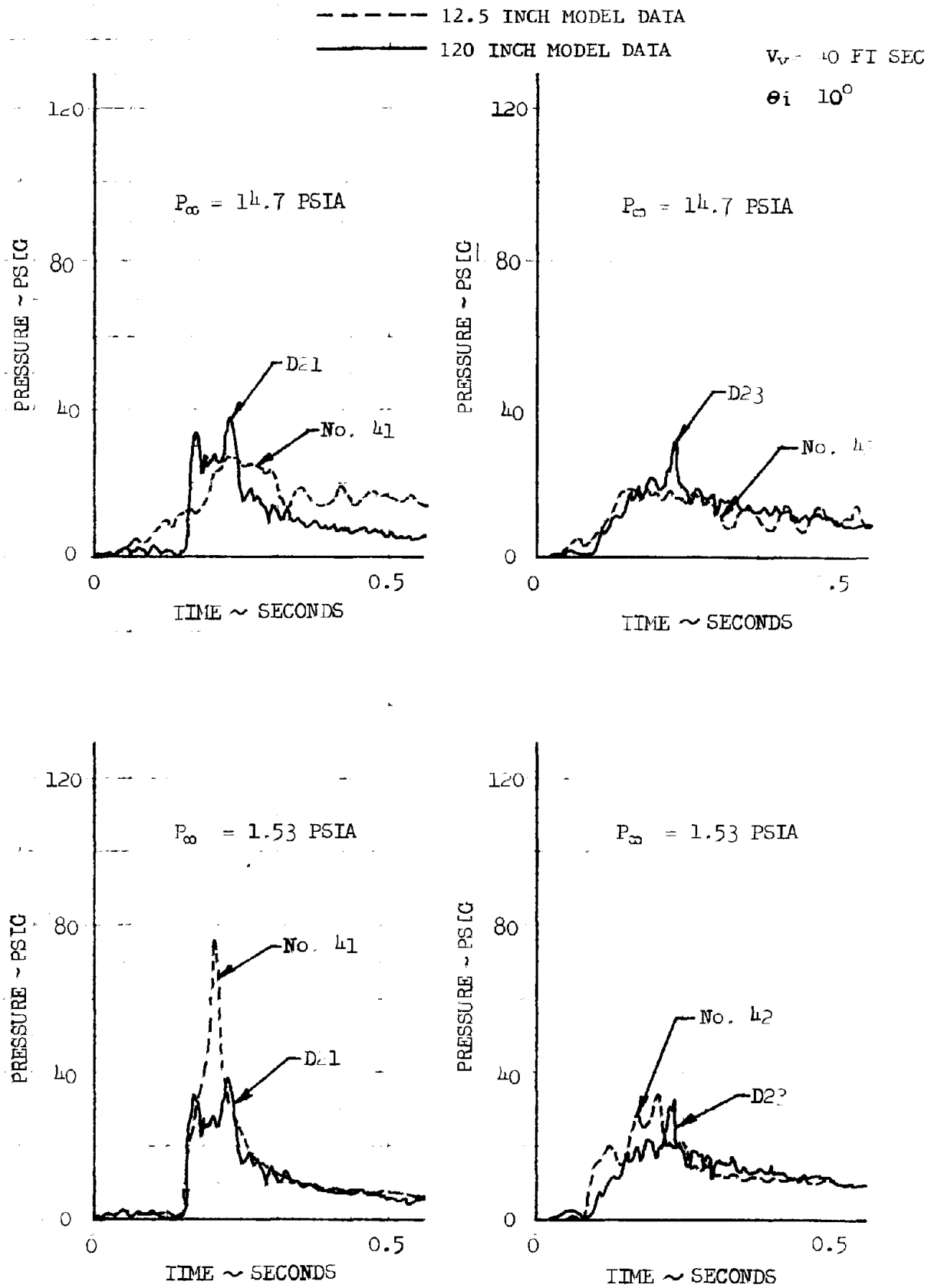


FIGURE 6-2 COMPARISON OF 12.5 INCH AND 120 INCH DIAMETER MODEL INTERNAL NOZZLE PRESSURES (PEAK VALUES)

12.5 INCH MODEL DATA ARE SCALED TO 120 INCH MODEL VALUES

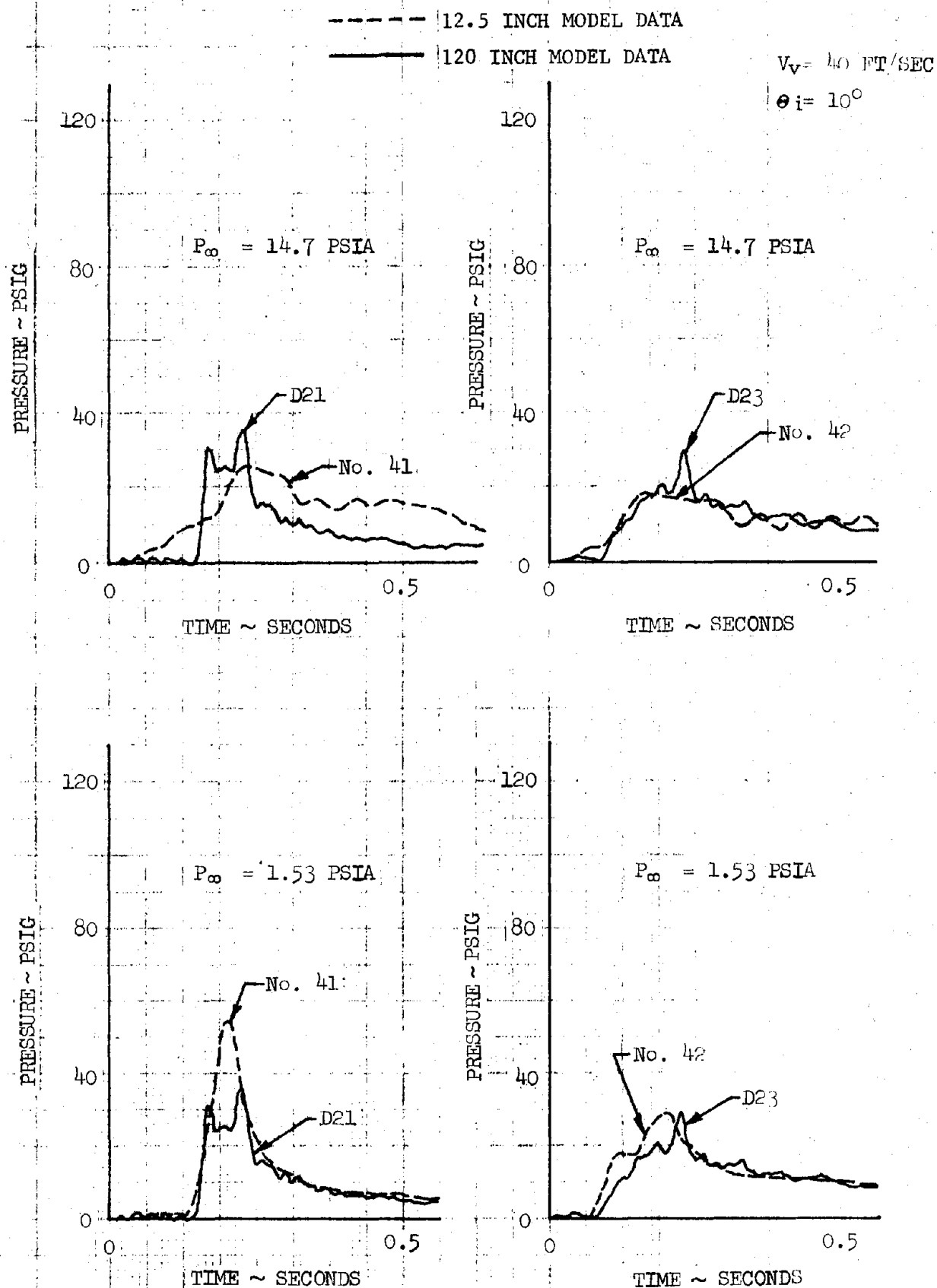


FIGURE 6-3 COMPARISON OF 12.5 INCH AND 120 INCH DIAMETER MODEL INTERNAL NOZZLE PRESSURES (10 MILLISECOND AVERAGE)

12.5 INCH MODEL DATA ARE SCALED TO 120 INCH MODEL VALUES

----- 12.5 INCH MODEL DATA

———— 120 INCH MODEL DATA

$V_v = 60$  FT/SEC

$\theta_i = 10^\circ$

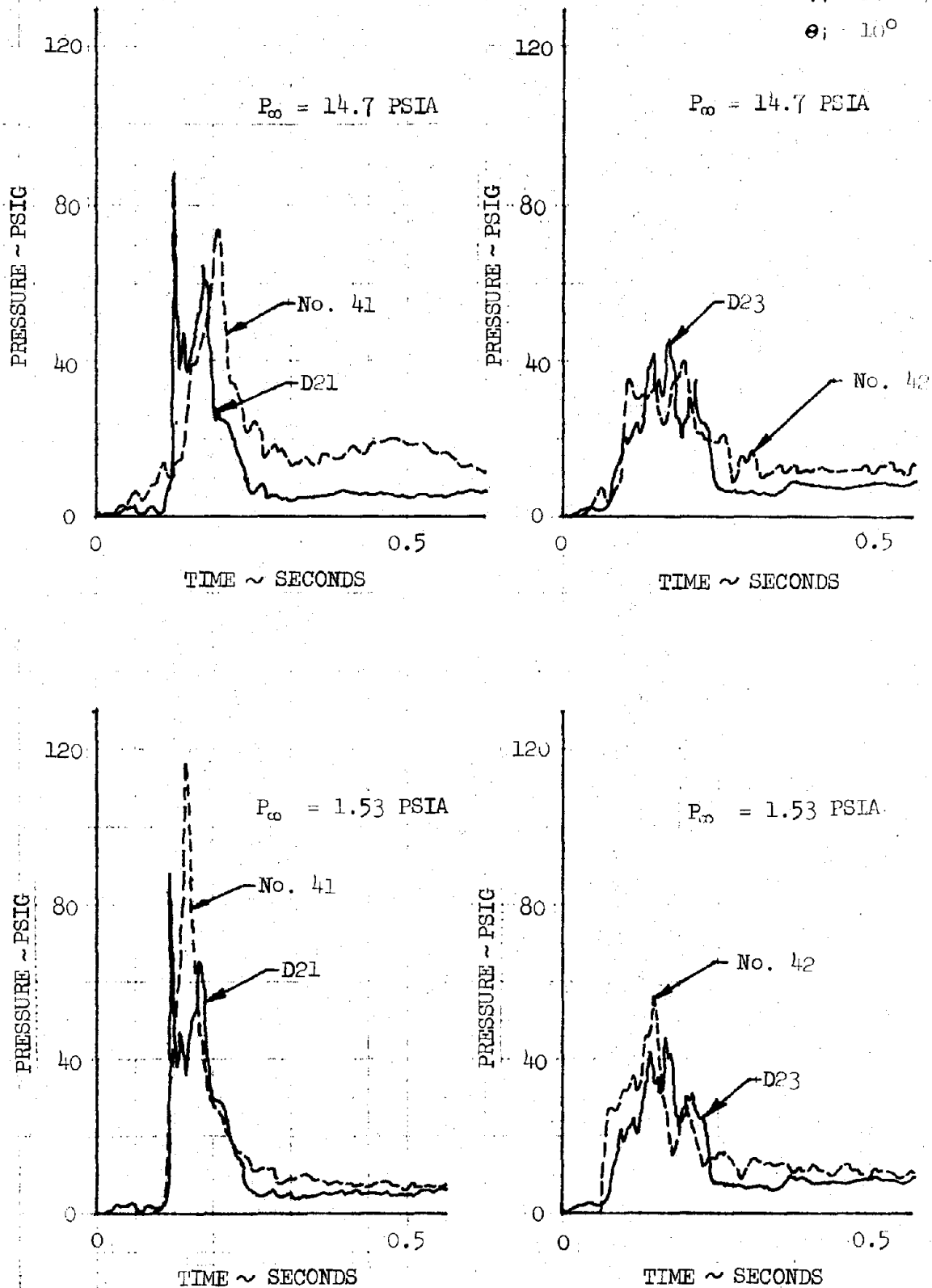


FIGURE 6-4 COMPARISON OF 12.5 INCH AND 120 INCH DIAMETER MODEL INTERNAL NOZZLE PRESSURES (PEAK VALUES)



12.5 INCH MODEL DATA ARE SCALED TO 120 INCH MODEL VALUES

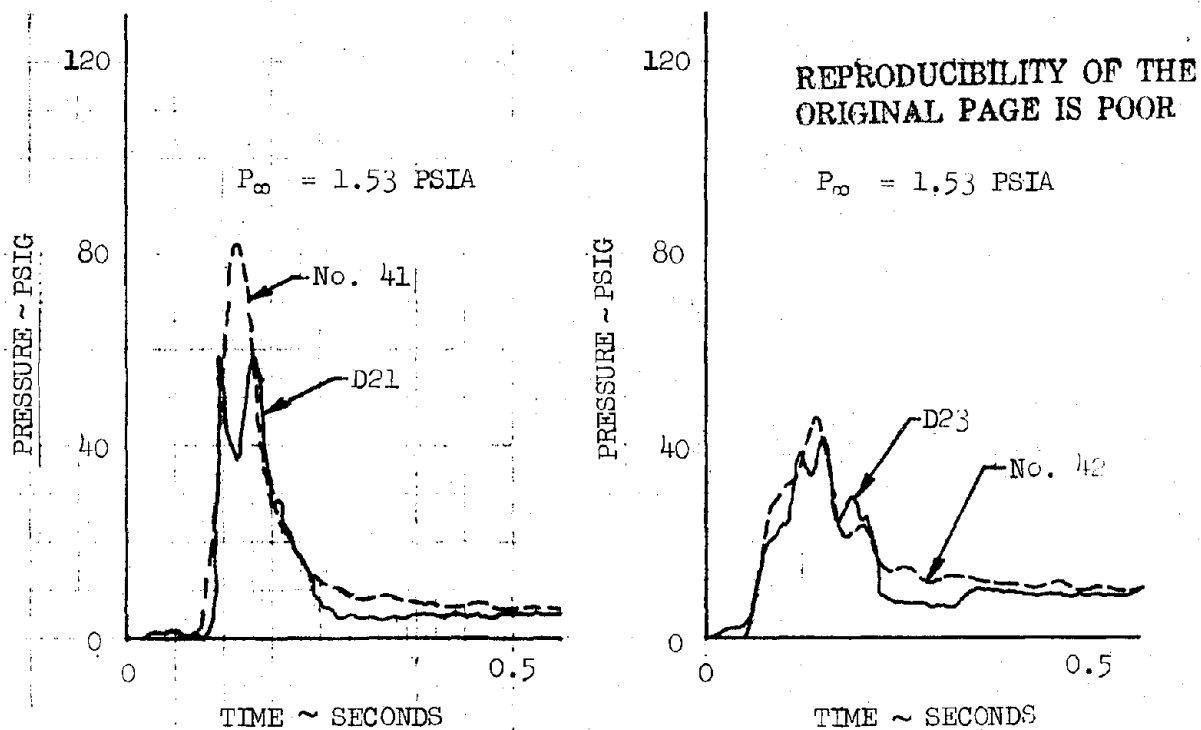
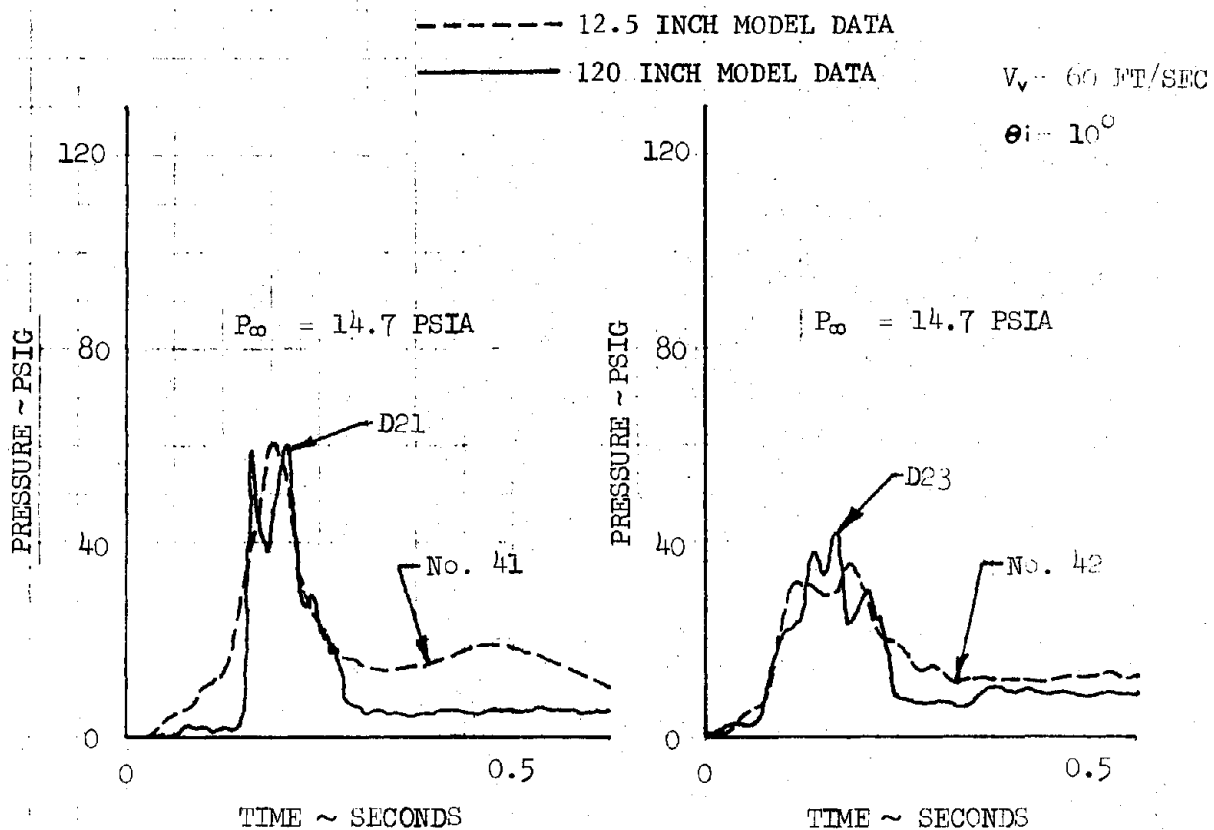


FIGURE 6-5 COMPARISON OF 12.5 INCH AND 120 INCH DIAMETER MODEL INTERNAL NOZZLE PRESSURES (10 MILLISECOND AVERAGE)

12.5 INCH MODEL DATA ARE SCALED TO 120 INCH MODEL VALUES

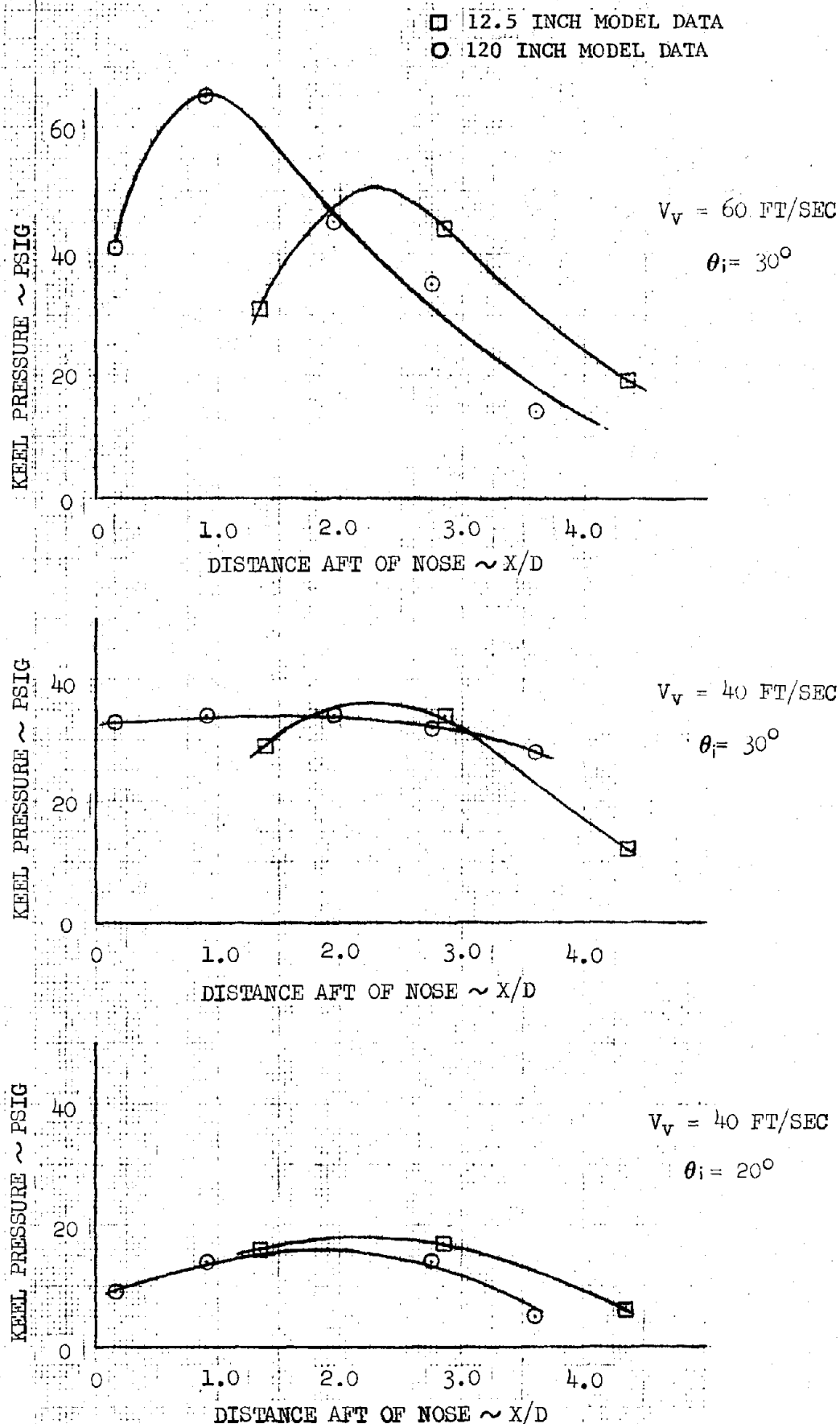


FIGURE 6-6 COMPARISON OF 12.5 INCH AND 120 INCH DIAMETER MODEL PEAK SLAPDOWN PRESSURE

12.5 INCH MODEL DATA ARE SCALED TO 120 INCH MODEL VALUES

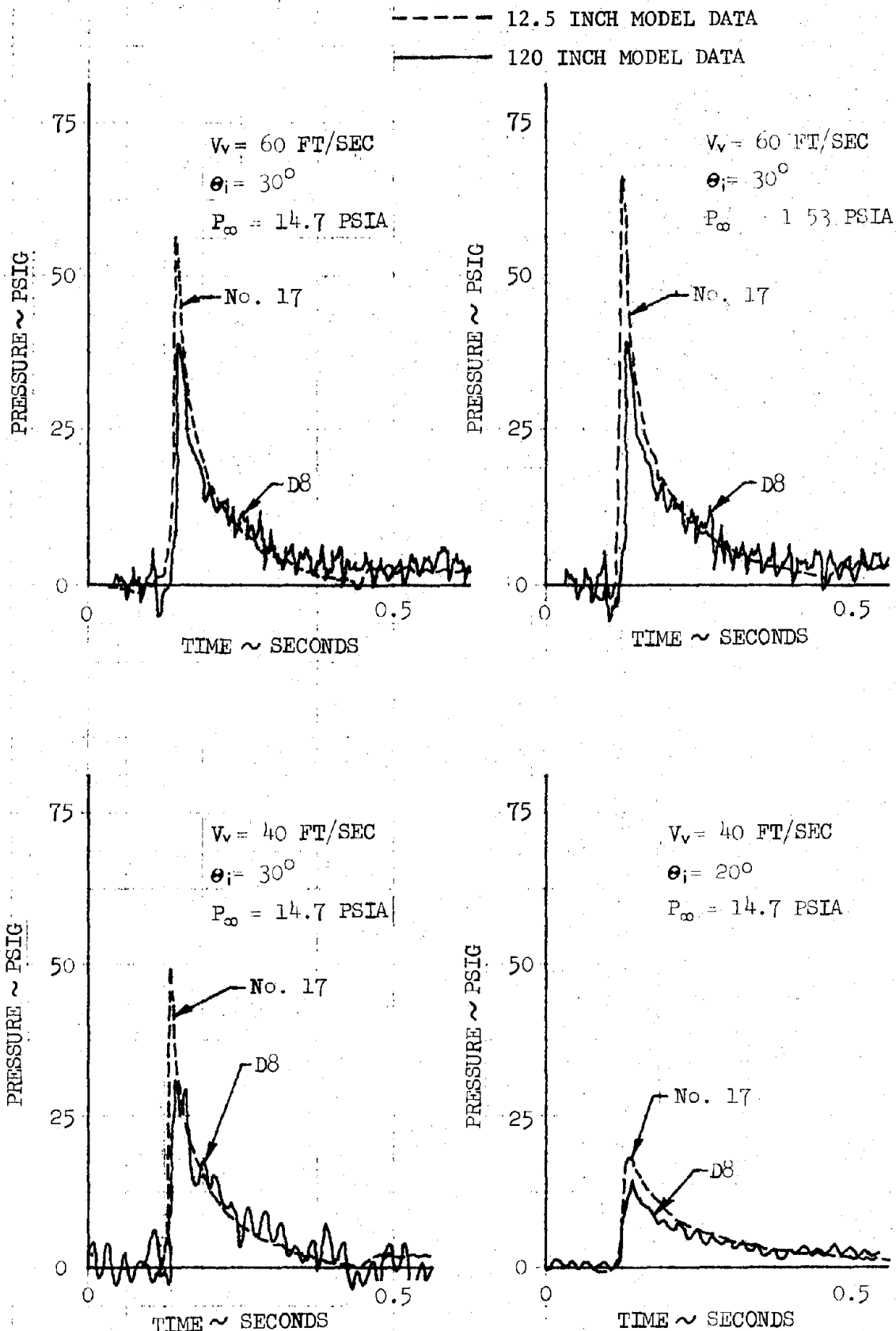


FIGURE 6-7 COMPARISON OF 12.5 INCH AND 120 INCH DIAMETER MODEL PRIMARY SLAPDOWN PRESSURES (PEAK VALUES)

12.5 INCH MODEL DATA ARE SCALED TO 120 INCH MODEL VALUES

----- 12.5 INCH MODEL DATA

———— 120 INCH MODEL DATA

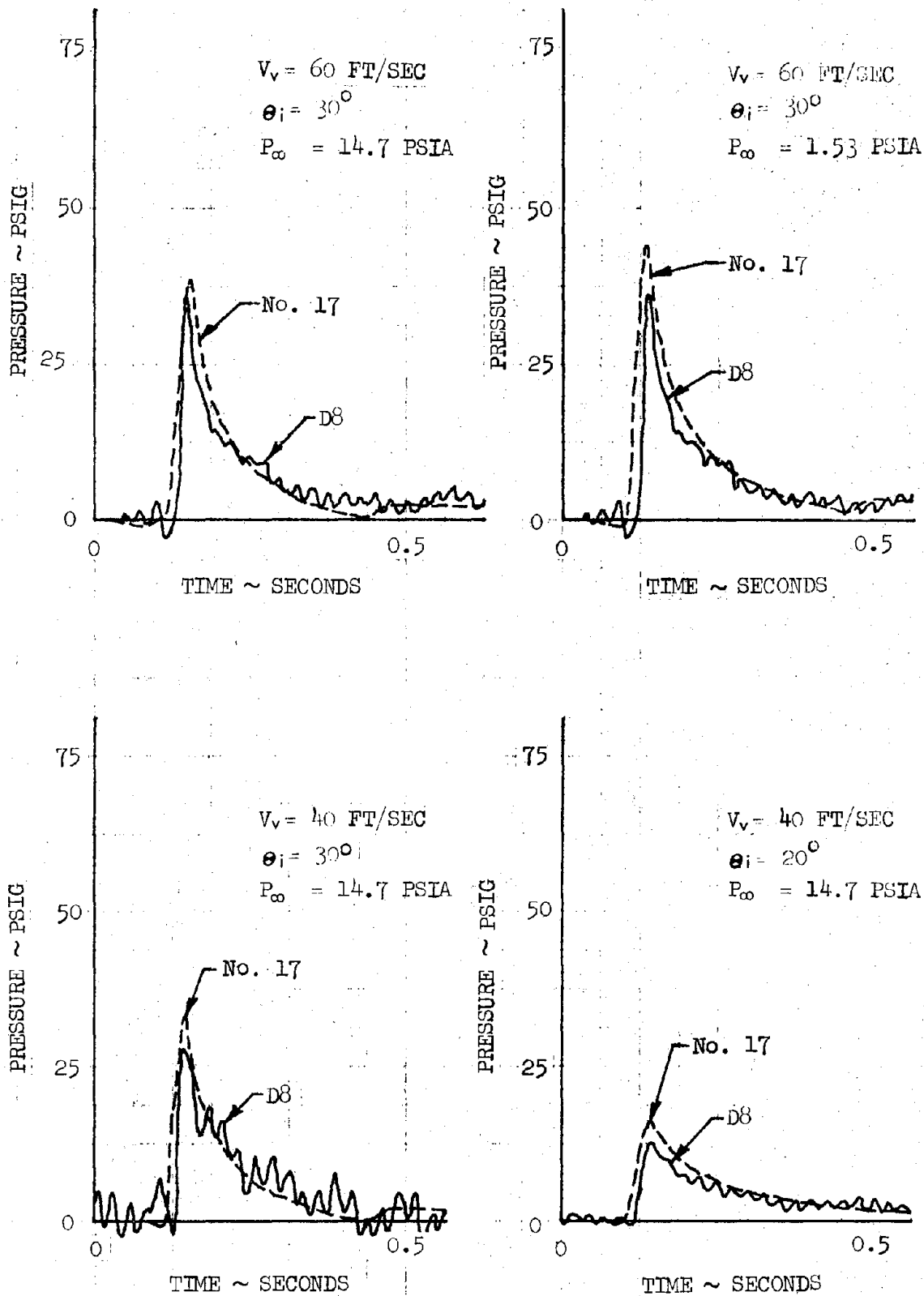


FIGURE 6-8 COMPARISON OF 12.5 INCH AND 120 INCH DIAMETER MODEL PRIMARY SLAPDOWN PRESSURES (10 MILLISECOND AVERAGE)

## SECTION 7.0

### DATA ANALYSIS

Typical plots of the drop test data are presented in Figure 7-1. Superimposed on the time histories in the figure are indications of the times of the various dynamic events characterizing the impact, as described in Section 5.0. As described earlier, the models were fabricated to be essentially rigid bodies. Nevertheless, they were not complete rigid. As a result, there was some minor dynamic response of the structure, excited by the impulsive loads of initial impact producing small oscillations in pressures and accelerations.

Since the elastic properties of the models were not to scale, instantaneous values of the data subject to these high frequency oscillations cannot necessarily be taken at face value, as they do not accurately reflect the hydroelastic response to be expected of the full-scale vehicle. At the same time, it must be remembered that the primary purpose of the model test data is to serve as a basis for generating full-scale loads for SRB structural design, and the stress analysis methods to be used in formulating that design are based on a static analysis. Therefore, the dynamic values of pressures and accelerations acting on the model during water impact cannot be used directly and must be replaced by equivalent static values which will produce stresses in the supporting structure equal to the maximum values actually developed by the short-duration dynamic loading.

The stress developed in a structure supporting a short-duration dynamic load is not only a function of the magnitude of the applied load, but it is also strongly dependent on the duration over which the load is applied. This duration defines an associated frequency. Depending on how this frequency compares with the natural frequency of the structure, the dynamic amplification factor will be greater or less than unity. That is, the stresses induced in the structure by the actual dynamic load will be greater than or less than those that would be induced by a load of the same magnitude and distribution applied for an extended period of time.

A method for determining the equivalent static load for a given short-duration dynamic load, presuming the supporting structure can be represented as a linear, elastic system with one degree of freedom, is given in Reference 23. Using this method, equivalent static values were determined for typical short-duration pressure pulses developed on the model during water impact. At the same time, the actual pressure-time histories were averaged by computer over various averaging time intervals and re-plotted. The calculated equivalent static values were then compared with the magnitudes taken on by the same pressure in the time-averaged plots. The comparison showed that equivalent static values for the pressures and accelerations developed on the model during water impact could be approximated by reading 10 millisecond averages of the original data. Therefore, in reducing the data for the model tests, 10 millisecond average values were read for all quantities with the exception of cavity collapse data. The pulse period for cavity collapse is of the same order as the case natural period for the first ring mode and actual peak values were used for this event.

## 7.1 Initial Impact

Nozzle Toe-in. Initial contact by the vehicle with the liquid free surface was detected by the accelerometers. All registered an instantaneous displacement from their free-fall positions at the moment of contact. The time of nozzle toe-in was then given by the spike in nozzle external pressure immediately after initial contact (Figure 7-1). Only a limited portion of the nozzle extension is wetted at this time, and only one transducer read non-zero pressure. Therefore, the precise boundary of the wetted surface and distribution of pressure over this surface could not be determined and had to be assumed. It was assumed that only that portion of the nozzle extension not shielded by the skirt from relative flow due to the horizontal component of velocity was wetted (Figure 7-2). The pressure associated with this flow was then taken to be constant along the  $\phi = 0^\circ$  meridian and to vary circumferentially with the cosine of the ray angle,  $\phi$ . Flow separation (zero pressure) was assumed at the nozzle exit plane or at  $\phi = \pm 90^\circ$ , whichever was encountered first by the individual streamlines of the presumed flow.

Maximum Pitch Acceleration. This event was detected by all three pitch accelerometers. By definition, the time for this event is taken to be the time at which the value of the pitch acceleration reaches a maximum. Due to the elasticity of the model structure, the time indicated for the event by the three accelerometers was not always precisely the same; under certain impact conditions, the indicated time varied by 2 to 4 milliseconds. Therefore, the output of the accelerometer located farthest aft, and therefore closest to that portion of the vehicle over which the impact

loads were applied, was selected as the reference for determining the time of maximum pitch acceleration (Fig. 7-3).

The nozzle and skirt are only partially wetted at the time of maximum acceleration, and since the number of pressure transducers installed in this region was limited, a precise description of the wetted boundary was not obtained. Therefore, for purposes of evaluating the loads, the boundary was prescribed by a rather arbitrary interpolation between wetted and unwetted transducer locations. Since only one transducer on the skirt and one on the nozzle were wetted along the  $\phi = 0^\circ$  meridian, pressures along the wetted portions of the meridian were assumed constant. Two transducers measuring nozzle internal pressure along the  $\phi = 180^\circ$  meridian gave non-zero and unequal readings, so the longitudinal distribution of pressure along the meridian was assumed to vary linearly. Based on the results of Ref. 4, the circumferential distributions were assumed to vary with the cosine of the ray angle, as described in Figures 7-4 through 7-6.

Nozzle and skirt pressures were read at the time of maximum pitch acceleration for all tests. With actual impact conditions ( $V_V$ ,  $V_H$ ,  $\theta$ ) measured from the photographic data for each test, the resultant velocity,  $U$  and effective impact angle ( $\alpha - \theta$ ) were calculated by,

$$U = \sqrt{V_V^2 + V_H^2}$$

$$(\alpha - \theta) = \tan^{-1} \left( \frac{V_H}{V_V} \right) - \theta$$

The equivalent non-dimensional pressure,  $\frac{P}{\frac{1}{2} \rho U^2}$  was then calculated for each measured nozzle and skirt pressure and plotted as a function of



$(\alpha - \theta)$ . For each measured quantity, the result should be a family of curves with  $V_V$ ,  $V_H$ , or  $\theta$  as parameters. However, due to experimental error, the plots exhibited considerable scatter, and the parametric dependence could not be discerned. Nevertheless, a mean curve was easily drawn. Similar curves were constructed for axial locations coincident with nozzle throat and nozzle and skirt exit planes by cross-plotting the non-dimensional curves for the pressures at the transducer locations, extrapolating and replotting. Since given impact conditions dictate corresponding values for  $U$  and  $(\alpha - \theta)$ , these non-dimensional curves then yielded nozzle and skirt pressures at throat and exit planes for any given set of  $V_V$ ,  $V_H$ , and  $\theta$ . Given the matrix of full-scale impact conditions of interest, the pertinent nozzle and skirt pressures required for quantitative definition of the pressure distribution over the wetted surface were then obtained directly from the curves. They were later carpet plotted as functions of impact conditions (Fig. 7-9).

The pressures were integrated over the surface of the vehicle to give the resultant force in the direction of the vehicle axis, the resultant force normal to the axis in the pitch plane, and the associated pitch moment developed about the C.G. Vehicle mass and pitch moment of inertia were used to calculate axial, normal and angular accelerations at the time of maximum pitch acceleration (Figs. 7-11 and 7-12). Axial load, shear and bending moment were then calculated as a function of vehicle station. (Fig. 7-13).

Maximum Axial Acceleration. The time for the maximum axial acceleration event is defined as the time at which the value of the axial acceleration reaches a maximum. The event was detected by the axial accelerometers.

Generally, there was very little difference in the time indicated by all three accelerometers. However, in those cases in which there was appreciable difference, the accelerometer located farthest aft was used as the reference.

At the time of maximum axial acceleration, the nozzle is flowing full and an appreciable amount of water has entered the nozzle-skirt annulus. Therefore, the wetted surface and pressure distribution over that surface are relatively well-defined. Measurements indicated that the pressure acting on the bulkhead and skirt internal surface was essentially constant. Pressure acting on the nozzle internal surface was greater at the throat than at the exit plane, varying linearly with axial distance between the two locations. The nozzle external surface was not appreciably wetted, so the external pressure was taken to be constant and equal to ambient pressure. The circumferential distribution of pressure was assumed to be axisymmetric, based on the results of Ref. 4, so the pressures at maximum axial acceleration were taken to be independent of angle  $\phi$ . (Fig. 7-10).

The data reduction method for the maximum axial acceleration event was identical to that described above for the maximum pitch acceleration event.

## 7.2 Cavity Collapse

Cavity collapse is signalled by a sudden increase in external case and skirt pressures, and depending on the effective impact angle may result in large pitch accelerations. This event was detected by accelerometers and pressure transducers for every test condition except for a few at the highest effective impact angles for 120 ft/sec vertical velocity.

For the "typical model test data" of Figure 7-1, cavity collapse occurs at about 0.3 second after impact. The tail pitch accelerometer (EP007) goes from a pre-cavity-collapse quasi-steady level of +2 g's to a -1 g peak in about .02 seconds, and quickly returns to a post-cavity-collapse level of +1 g. At the same time, peaks are noted in the skirt external pressure (D0026), skirt internal pressure (D0028) and the nozzle internal pressure (D0025). This test condition corresponds to a rather high effective impact angle ( $\alpha - \theta = 32^\circ$ ) and cavity collapse does not result in severe loads. The +2 g tail accelerometer reading before cavity collapse is due to the fact that the keel centerline is wetted, i.e. the cavity does not envelope the vehicle, from just after impact through the complete entry.

Cavity collapse loads were found to be primarily a function of effective impact angle,  $\alpha - \theta$ , but for convenience are first discussed as a function only of pitch angle for zero horizontal velocity conditions. For a pure vertical impact, cavity development and collapse is symmetric about the vehicle centerline and results in sudden increase in pressure from zero to about 5 psig (model scale) over the aft 2 to 3 diameters of the vehicle. The cavity shape and resulting maximum pressures on the keel and lee meridians at cavity collapse are illustrated in figure 7-14a.

Maximum cavity collapse pressures are encountered at  $(\alpha - \theta) \approx 10^\circ$ . For this case the cavity envelopes the entire vehicle below the water surface until maximum cavity size is attained. The cavity collapses asymmetrically with respect to the vehicle but axisymmetrically with respect to a line just off the lee

side and has the typical shape and resulting pressure distributions as shown in figure 7-14b. Maximum pressures on the order of 15 to 20 psig, model scale, are generated on the lee meridian. As illustrated, a large portion of the keel side is wetted at cavity collapse whereas the lee side is wetted over a length somewhat less than for  $\alpha - \theta = 0$ . At impact angles ( $\alpha - \theta$ ) greater than about 10 degrees, the cavity collapse pressures and loads decrease for the reasons discussed in section 5.2.

The primary test upon which the loads analysis of this report are based is the P-015 test, conducted at ambient atmospheric pressure, and simulated entries with various horizontal velocities, vertical velocities and pitch angles at impact. This test yielded keel pressure distributions and total loads (accelerations) at cavity collapse for the full range of expected entry conditions. Lee side pressure distributions were obtained in test P-029, also an ambient atmospheric test, but horizontal velocity was not simulated in this test. Thus the lee side pressures had to be estimated for horizontal velocity impact conditions.

Estimates of the lee side pressure distributions for conditions with horizontal velocity were made using the known total normal force and moment (from accelerometer data) and keel pressure distribution, lee side wetted length (measured from underwater camera pictures), and estimates of the circumferential pressure distributions. A balance of applied pressure loads and inertial reaction loads then yields the lee side pressure load. The lee side pressure load was then distributed over the above wetted length with a lee meridian pressure distribution similar to those measured for zero horizontal velocity. The effect of on-board water was accounted

for in the load balancing by assuming that the nozzle and skirt were full of water but that it was only 50% effective in reacting the applied loads. The reduction in effectiveness was used to account for the fact that this water is not fixed to the vehicle but is free to flow out of the nozzle and skirt.

The circumferential pressure distributions from the base of the vehicle to the lee side wetted length are based on previous tests of a 12.5 in. model of the 156 inch-diameter configuration tested at atmospheric and scaled ambient pressure at the Naval Ordnance Laboratory Hydroballistics Tank. Circumferential pressure distributions were measured at two stations near the base of the model. The cavity collapse distributions were found to be very similar at all significant test conditions. The keel side pressures were found to be very nearly constant from the keel to the side meridians. From the side meridian, the pressure rises to a maximum at the lee meridian. All of the distributions could be represented quite closely as

$$P = P_0 + K_c (P_{180} - P_0)$$

where  $P_0$  is the keel pressure,  $P_{180}$  is the lee pressure, and  $K_c$  is an empiric factor derived from the data and shown in Figure 7-17.

Forward of the lee side wetted length the circumferential pressure distribution is taken to be of the form

$$P = P_0 \cdot \frac{1}{2} \left[ 1 + \cos \left( \frac{\phi}{\phi_w} \cdot \pi \right) \right]$$

where  $\phi_w$  is the angle from the keel meridian to a wetted line drawn between the keel and lee side wetted lengths and may be expressed as

$$\phi_w = \cos^{-1} \left[ \frac{2(X-L_{w2})}{(L_{w1}-L_{w2})} - 1 \right]$$

### 7.3 Maximum Penetration

Maximum penetration was determined through analysis of high speed motion picture data recorded during the model test programs. These films were viewed with a Vanguard Film Analyzer and the relative position of a point on the model was tracked on successive frames from shortly before impact until the model was obscured by the water spray. Time and the  $x, y, \theta$  model coordinates were then processed in a computer program which calculated the horizontal and vertical position and velocity of the model nose, C.G., and tail during water entry.

The reduced photographic data was examined and the point of maximum penetration selected. The model depth and pitch angle at maximum penetration were smoothed and carpet plotted as a function of impact condition.

### 7.4 Slapdown

As discussed in Section 5, slapdown is defined as that phase of water entry where high pitch rates induced by the initial impact and/or unstable buoyancy forces rotate the vehicle to pitch attitudes where the keel meridian of the forward portion of vehicle is rapidly entering the water. The vehicle C.G. is generally at or approximately one diameter below the water surface during this phase of water entry, the pitch angle is at 50 to 80°, and the instantaneous center of rotation is near the vehicle base. This corresponds to keel meridian locations up to about 4 diameters from the nose penetrating the water surface at high velocities. High local

pressures and forces are generated which eventually reduce the angular velocity to zero and the vehicle settles to a near horizontal floating attitude.

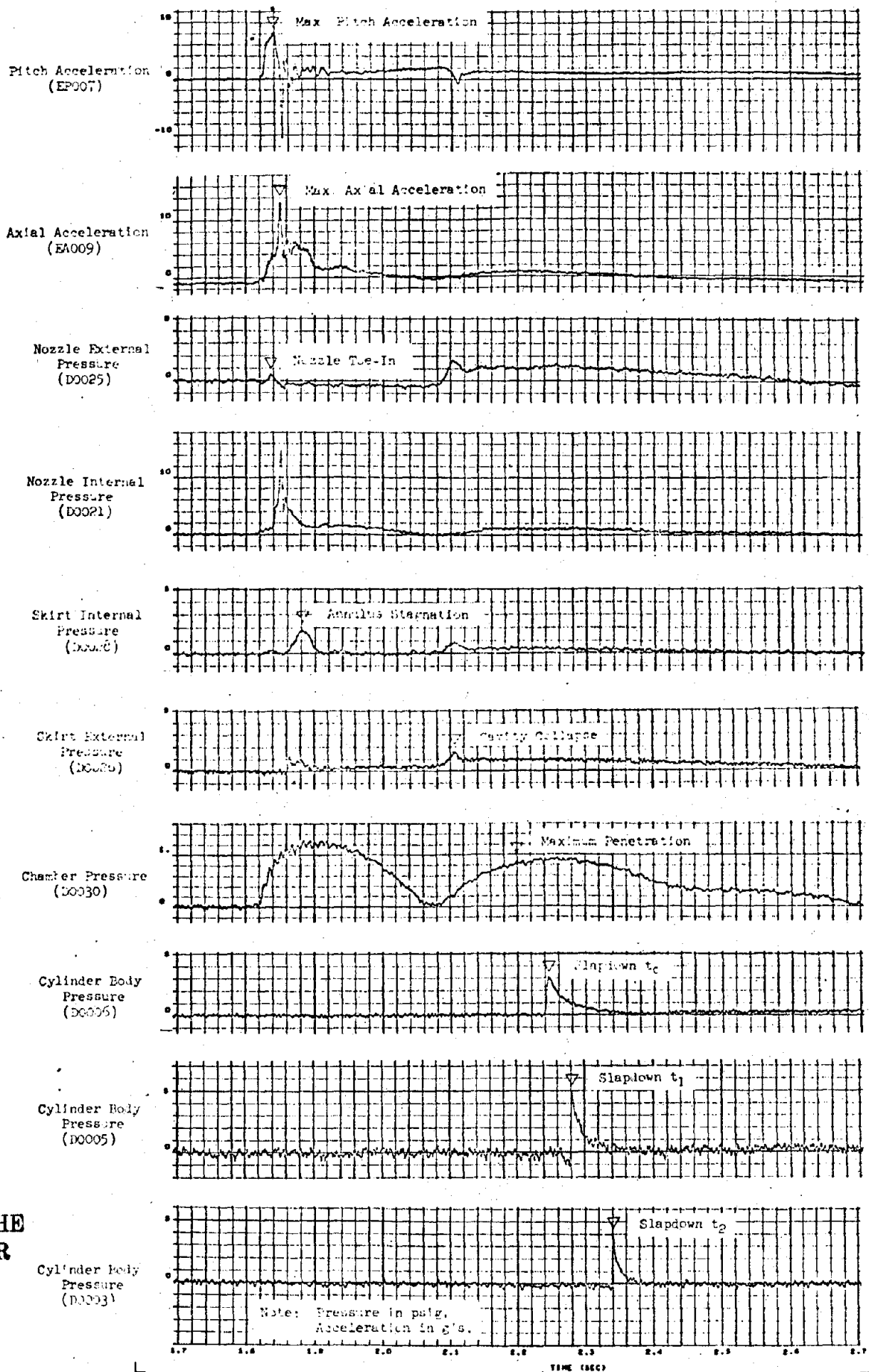
Slapdown occurs over a finite time period with time varying pressures and accelerations acting on the vehicle, and there is no specific time at which structural loads are obviously at a maximum. In order to investigate the variation of structural loads with time during slapdown, pressure distributions were integrated over the vehicle to obtain applied load distributions and the inertial reaction load distributions were calculated for several times during slapdown. The time points selected for slapdown load analyses were keyed to the times at which the keel pressure measured at selected transducer locations was at a maximum. Results of these analyses showed that keying the load analyses to maximum pressure times at transducer locations D0003, D0005 and D0006 (Figure 7-21), would yield three time points, one of which would always correspond to very near maximum values of local pressure, and/or shear and bending moment. Structural analysis at these three times ( $t_1$ ,  $t_2$ ,  $t_3$ , corresponding to maximum pressure times measured by D0006, D0005, D0003 respectively) should therefore give near maximum stresses for any given impact condition.

The slapdown phase is illustrated by the typical model test data and corresponding full scale trajectory shown in Figures 7-21 and 7-22. Initial full scale impact conditions for this run are:  $V_V = 84$  fps,  $V_H = 34$  fps,  $\theta = -8.9$  deg. The pitch angular velocity increases rapidly to about 19 deg/sec during the initial impact phase and then gradually increases to

about 45 deg/sec until cavity collapse occurs at  $t = 1.0$  sec. Prior to cavity collapse the keel side of the vehicle beneath the water surface is exposed to hydrodynamic pressures while the lee side is in a cavity at near ambient pressure, causing significant tip over moments. After cavity collapse, both keel and lee sides experience nearly the same pressure and the pitch angular velocity remains constant till about  $t = 1.2$  sec. The vehicle C.G. penetrates the free water surface at  $t = 1.3$  sec at a pitch angle of -50 degrees, and slapdown pressures on the keel side above the C.G. have already started to reduce the pitch angular velocity.  $t_1$ ,  $t_2$  and  $t_3$  are 1.4, 1.58 and 1.78 seconds, respectively for this run as indicated on the trajectory. At  $t_3$ , the pitch angular velocity is down to 28 deg/sec, and is monotonically decreasing.

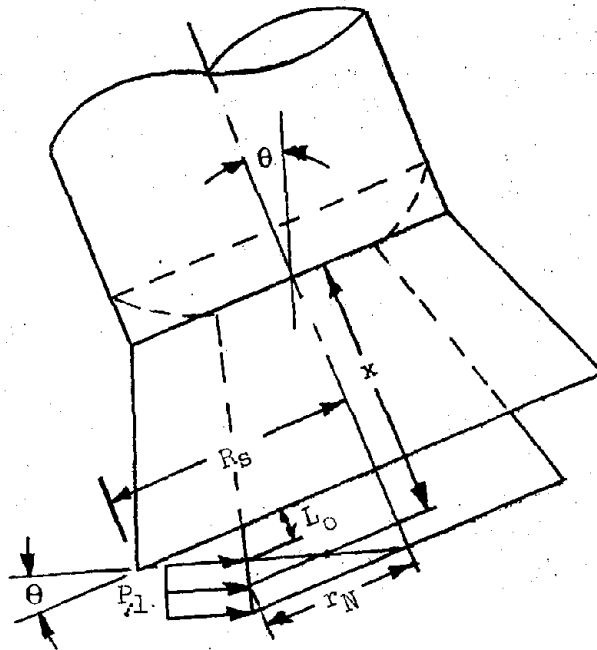
The total vehicle forces and accelerations during slapdown are generally of low frequency (on the order of 1 cps) and low amplitude (less than 4 g's at vehicle nose) when compared to initial impact while the local peak pressures on the vehicle keel are high frequency and high amplitude (see pressures D0003, D0005, D0006, Figure 7-21). The slapdown pressure time history for a given keel pressure transducer actually appears as a suddenly applied pressure with an exponential decay to approximately local hydrostatic. Although the local peak pressures near the keel penetration location appear as a high frequency pressure pulse, the overall keel pressure load induces low frequency vehicle loads, on the order of 1 Hz. The vehicle position for the above three slapdown times are illustrated in Figure 7-23.





REPRODUCIBILITY OF THE  
ORIGINAL PAGE IS POOR

FIGURE 7-1 TYPICAL MODEL TEST DATA (TEST P015-70)



# NOZZLE PRESSURE

## ◦ EXTERNAL

$$P = P_1 \cdot \cos \phi$$

The wetted surface is defined to be that portion of the nozzle extension below the undisturbed liquid free surface at the moment the skirt makes initial contact. The limits on  $\phi$  for a given value of  $x$  are then defined by the waterline, but are not to exceed  $\pm 90^\circ$ .

NOTE: All surfaces for which pressure is not specified are subject to ambient pressure.

FIGURE 7-2. PRESSURE DISTRIBUTION AT NOZZLE TOE-IN  
(WITH NOZZLE EXTENSION)

# MSFC SRB WATER RECOVERY TEST P-015-70<sup>121</sup>

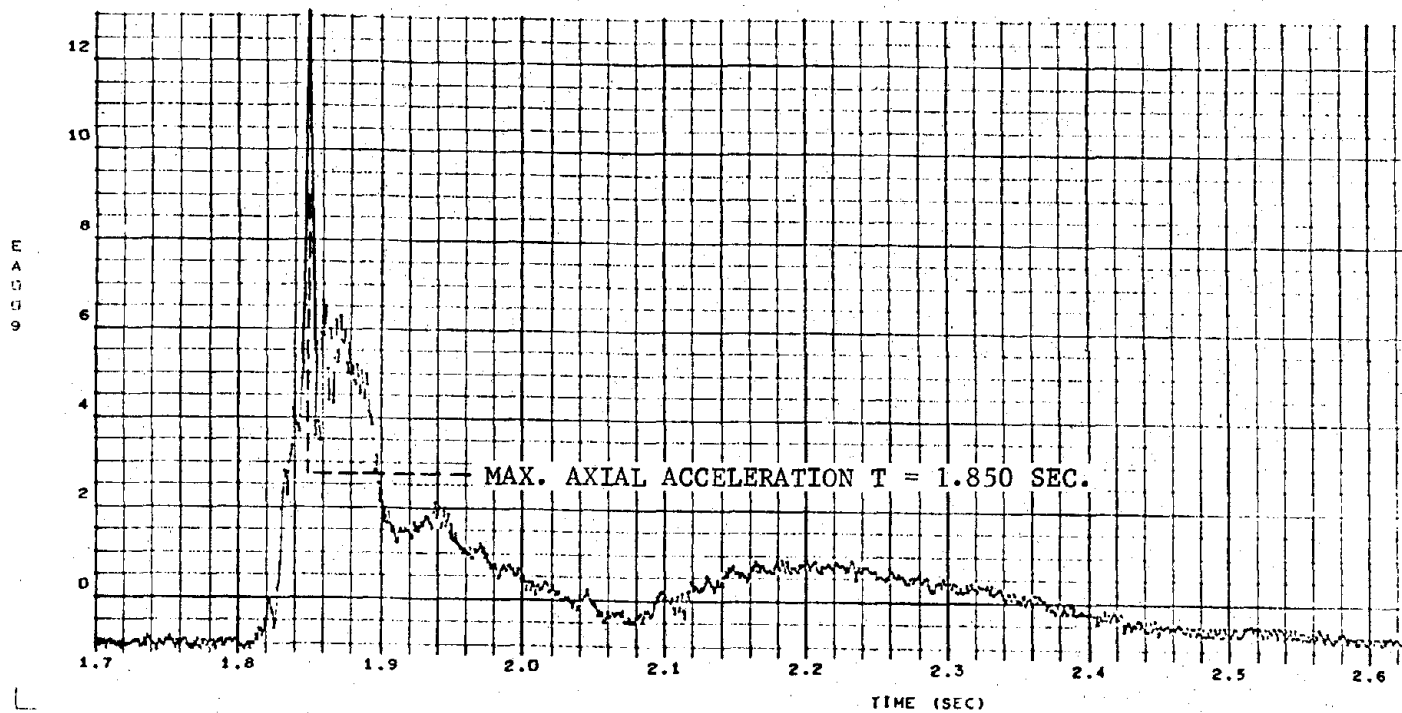
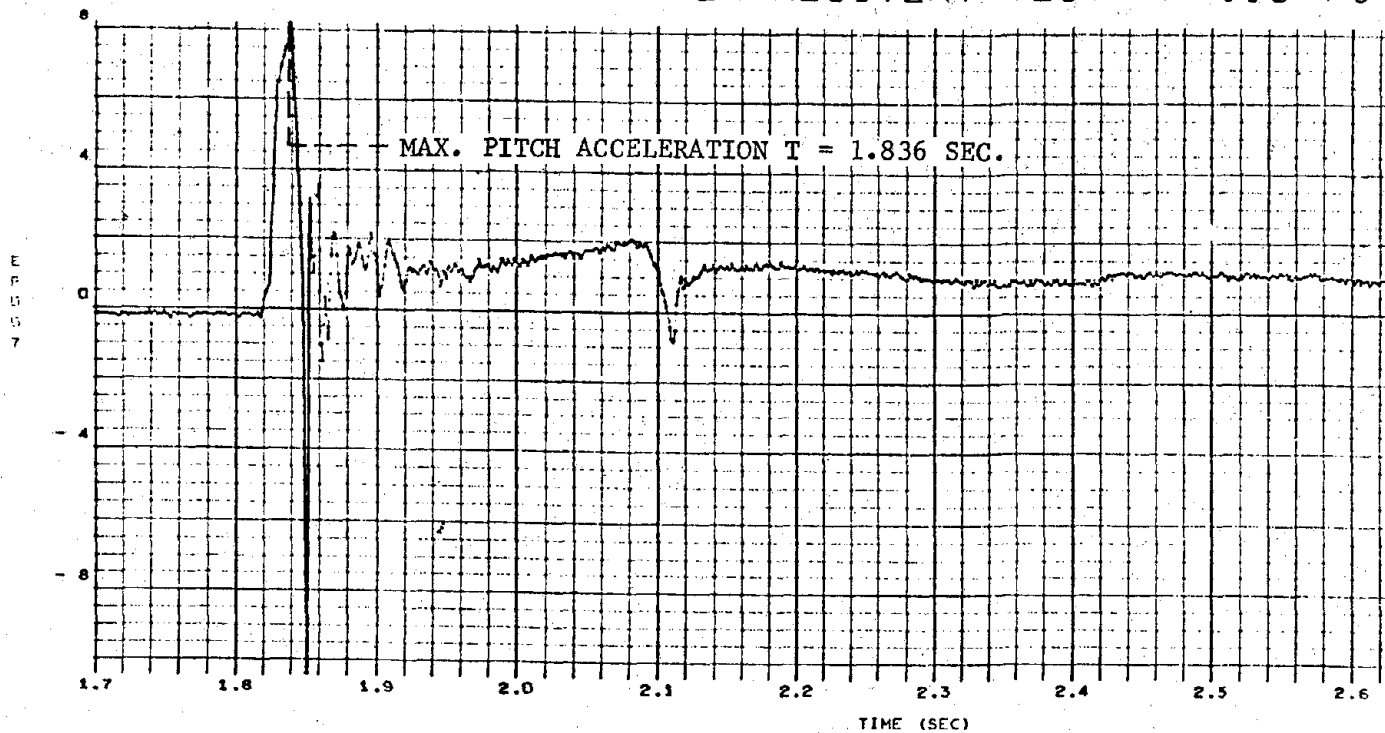


FIGURE 7-3 DETERMINATION OF MAXIMUM PITCH AND AXIAL ACCELERATION TIMES

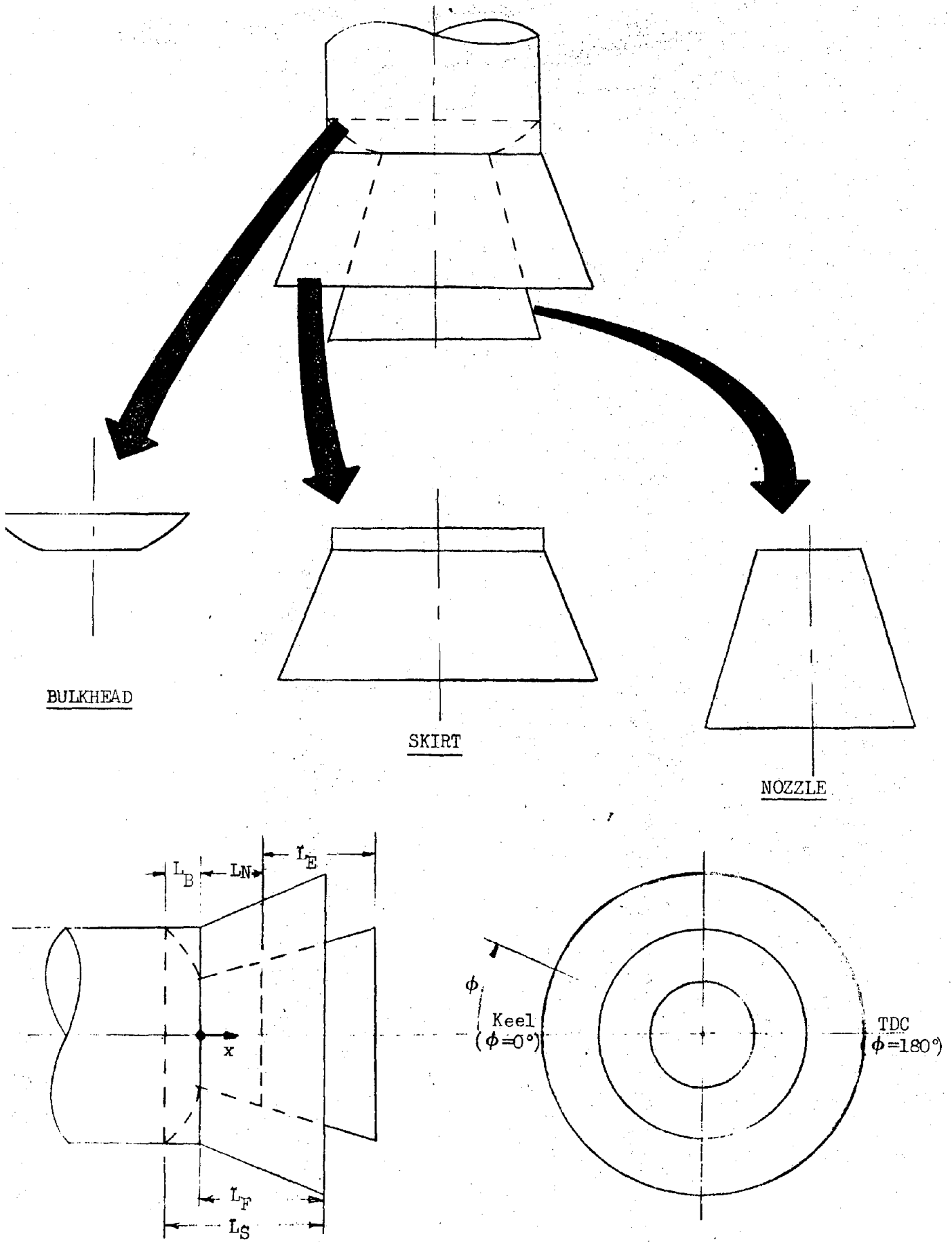
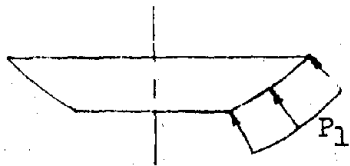


FIGURE 7-4 - DESCRIPTION OF VEHICLE AFT END GEOMETRY  
(WITH NOZZLE EXTENSION)

### BULKHEAD PRESSURE



● INTERNAL

$$P = P_{\text{ambient}} = \text{const.}$$

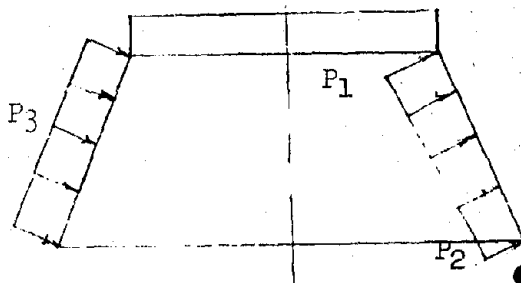
$$\left( \begin{array}{l} -L_B \leq x \leq 0 \\ -180^\circ \leq \phi \leq +180^\circ \end{array} \right)$$

● EXTERNAL

$$P = P_{\text{ambient}} + \frac{1}{2} (P_1 - P_{\text{ambient}})(1 - \cos \phi)$$

$$\left( \begin{array}{l} -L_B \leq x \leq 0 \\ -180^\circ \leq \phi \leq +180^\circ \end{array} \right)$$

### SKIRT PRESSURE



● INTERNAL

$$P = P_{\text{ambient}} + \frac{1}{2} (P_{180} - P_{\text{ambient}})(1 - \cos \phi)$$

$$\left( \begin{array}{l} 0 \leq x \leq L_F \\ -180^\circ \leq \phi \leq +180^\circ \end{array} \right)$$

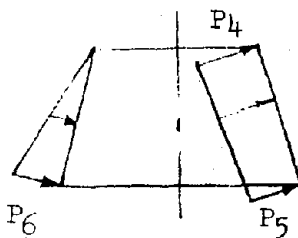
$$P_{180} = P_1 + \left( \frac{P_2 - P_1}{L_F} \right) \cdot x$$

● EXTERNAL

$$P = P_3 \cdot \cos \phi$$

$$\left( \begin{array}{l} 0 \leq x \leq L_F \\ -90^\circ \leq \phi \leq +90^\circ \end{array} \right)$$

### NOZZLE PRESSURE



● INTERNAL

$$P = P_{\text{ambient}} + \frac{1}{2} (P_{180} - P_{\text{ambient}})(1 - \cos \phi)$$

$$\left( \begin{array}{l} 0 \leq x \leq L_N \\ -180^\circ \leq \phi \leq +180^\circ \end{array} \right)$$

$$P_{180} = P_4 + \left( \frac{P_5 - P_4}{L_N} \right) \cdot x$$

● EXTERNAL

$$P = P_6 \cdot \cos \phi$$

$$\left( \begin{array}{l} 0 \leq x \leq L_N \\ -90^\circ \leq \phi \leq +90^\circ \end{array} \right)$$

$$P_0 = P_{\text{ambient}} + \left( \frac{P_6 - P_{\text{ambient}}}{L_N} \right) \cdot x$$

NOTE: All surfaces for which pressure is not specified are subject to ambient pressure.

FIGURE 7-5 . - PRESSURE DISTRIBUTION AT MAXIMUM PITCH ACCELERATION (WITHOUT NOZZLE EXTENSION)

### BULKHEAD PRESSURE



● INTERNAL

$$P = P_{\text{ambient}} = \text{const.}$$

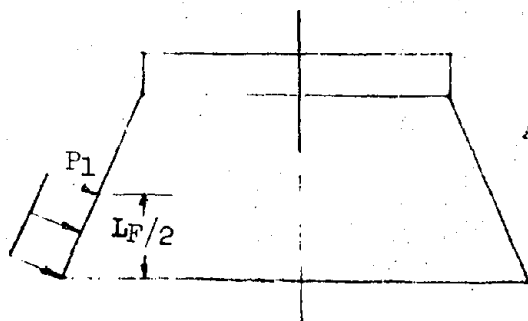
$$\left( \begin{array}{l} -L_B \leq x \leq 0 \\ -180^\circ \leq \phi \leq +180^\circ \end{array} \right)$$

● EXTERNAL

$$P = P_{\text{ambient}} = \text{const.}$$

$$\left( \begin{array}{l} -L_B \leq x \leq 0 \\ -180^\circ \leq \phi \leq +180^\circ \end{array} \right)$$

### SKIRT PRESSURE



● INTERNAL

$$P = P_{\text{ambient}} = \text{const.}$$

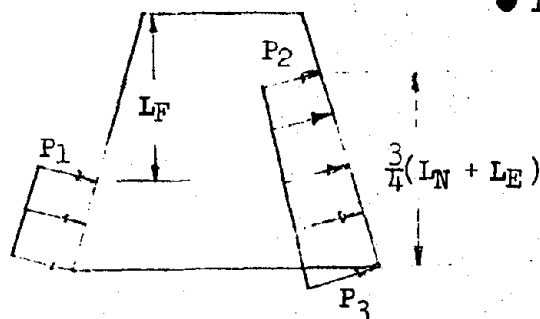
$$\left( \begin{array}{l} 0 \leq x \leq L_F \\ -180^\circ \leq \phi \leq +180^\circ \end{array} \right)$$

● EXTERNAL

$$P = P_1 \cdot \cos \phi$$

$$\left( \begin{array}{l} \frac{L_F}{2} \leq x \leq L_F \\ -90^\circ \leq \phi \leq +90^\circ \end{array} \right)$$

### NOZZLE PRESSURE



● INTERNAL

$$P = P_{\text{ambient}} + \frac{1}{2} (P_{180} - P_{\text{ambient}}) (1 - \cos \phi)$$

$$\left( \begin{array}{l} \frac{L_N + L_E}{4} \leq x \leq L_N + L_E \\ -180^\circ \leq \phi \leq +180^\circ \end{array} \right)$$

$$P_{180} = P_2 + \frac{4}{3} \left( \frac{P_3 - P_2}{L_N + L_E} \right) \left( x - \frac{L_N + L_E}{4} \right)$$

● EXTERNAL

$$P = P_1 \cdot \cos \phi$$

$$\left( \begin{array}{l} L_F \leq x \leq L_N \\ -90^\circ \leq \phi \leq +90^\circ \end{array} \right)$$

NOTE: All surfaces for which pressure is not specified are subject to ambient pressure.

FIGURE 7-6 - PRESSURE DISTRIBUTION AT MAXIMUM PITCH ACCELERATION (WITH NOZZLE EXTENSION)

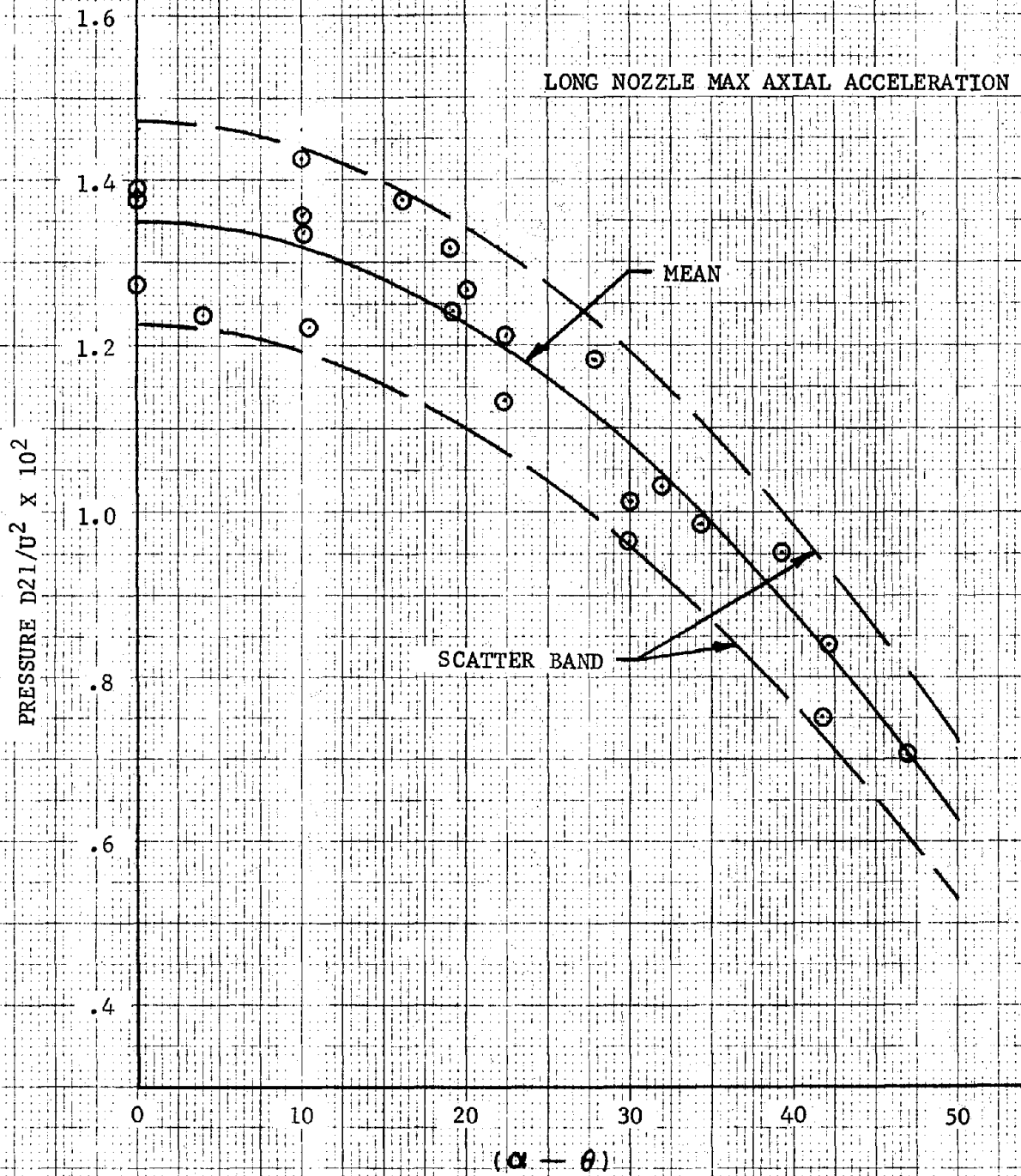


FIGURE 7-7. CORRELATION OF NOZZLE PRESSURE D21

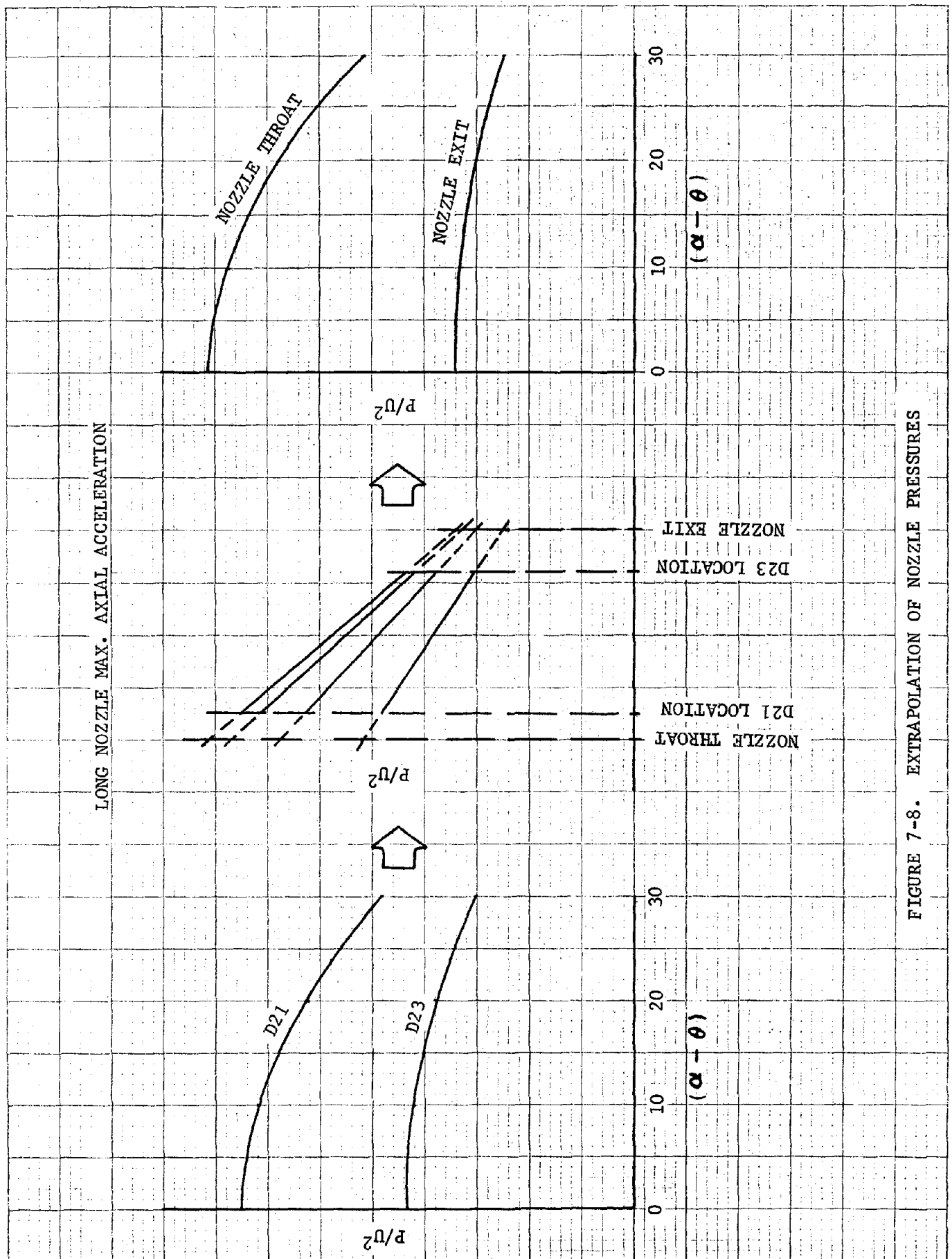
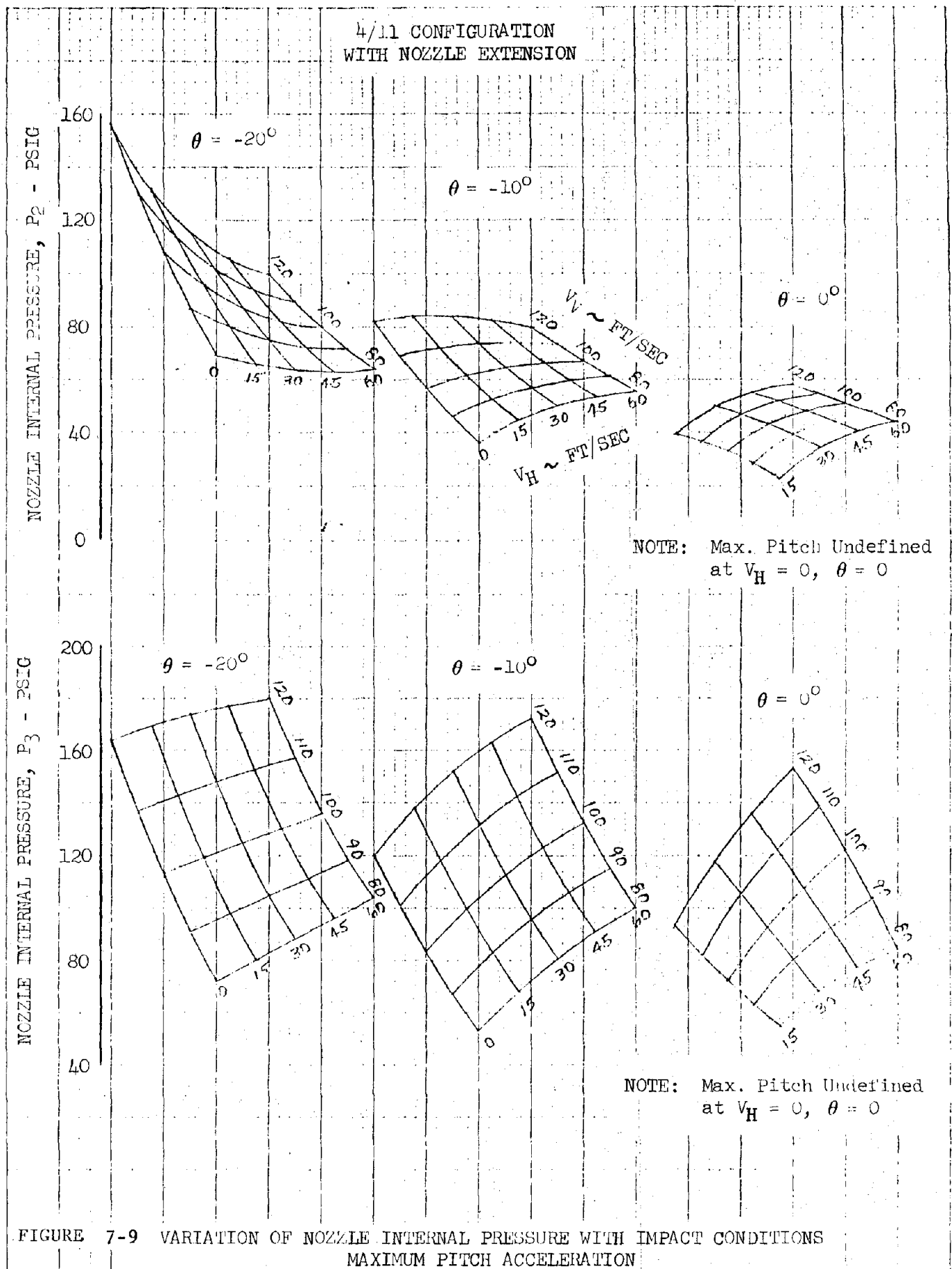
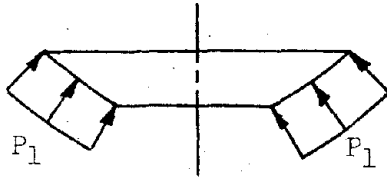


FIGURE 7-8. EXTRAPOLATION OF NOZZLE PRESSURES





### BULKHEAD PRESSURE



● INTERNAL

$$P = P_{\text{ambient}} = \text{const.}$$

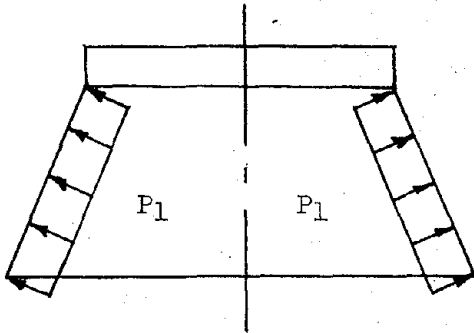
$$\left( \begin{array}{c} -L_B \leq x \leq 0 \\ -180^\circ \leq \phi \leq +180^\circ \end{array} \right)$$

● EXTERNAL

$$P = P_1 = \text{const.}$$

$$\left( \begin{array}{c} -L_B \leq x \leq 0 \\ -180^\circ \leq \phi \leq +180^\circ \end{array} \right)$$

### SKIRT PRESSURE



● INTERNAL

$$P = P_1 = \text{const.}$$

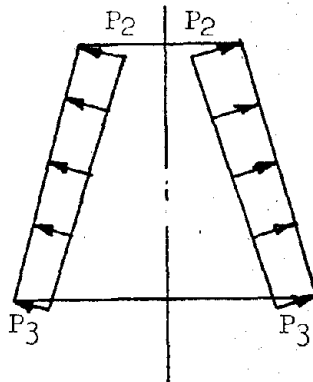
$$\left( \begin{array}{c} 0 \leq x \leq L_F \\ -180^\circ \leq \phi \leq +180^\circ \end{array} \right)$$

● EXTERNAL

$$P = P_{\text{ambient}} = \text{const.}$$

$$\left( \begin{array}{c} 0 \leq x \leq L_F \\ -180^\circ \leq \phi \leq +180^\circ \end{array} \right)$$

### NOZZLE PRESSURE



● INTERNAL

$$P = P_2 + \left( \frac{P_3 - P_2}{L_N} \right) \cdot x$$

$$\left( \begin{array}{c} 0 \leq x \leq L_N \\ -180^\circ \leq \phi \leq +180^\circ \end{array} \right)$$

● EXTERNAL

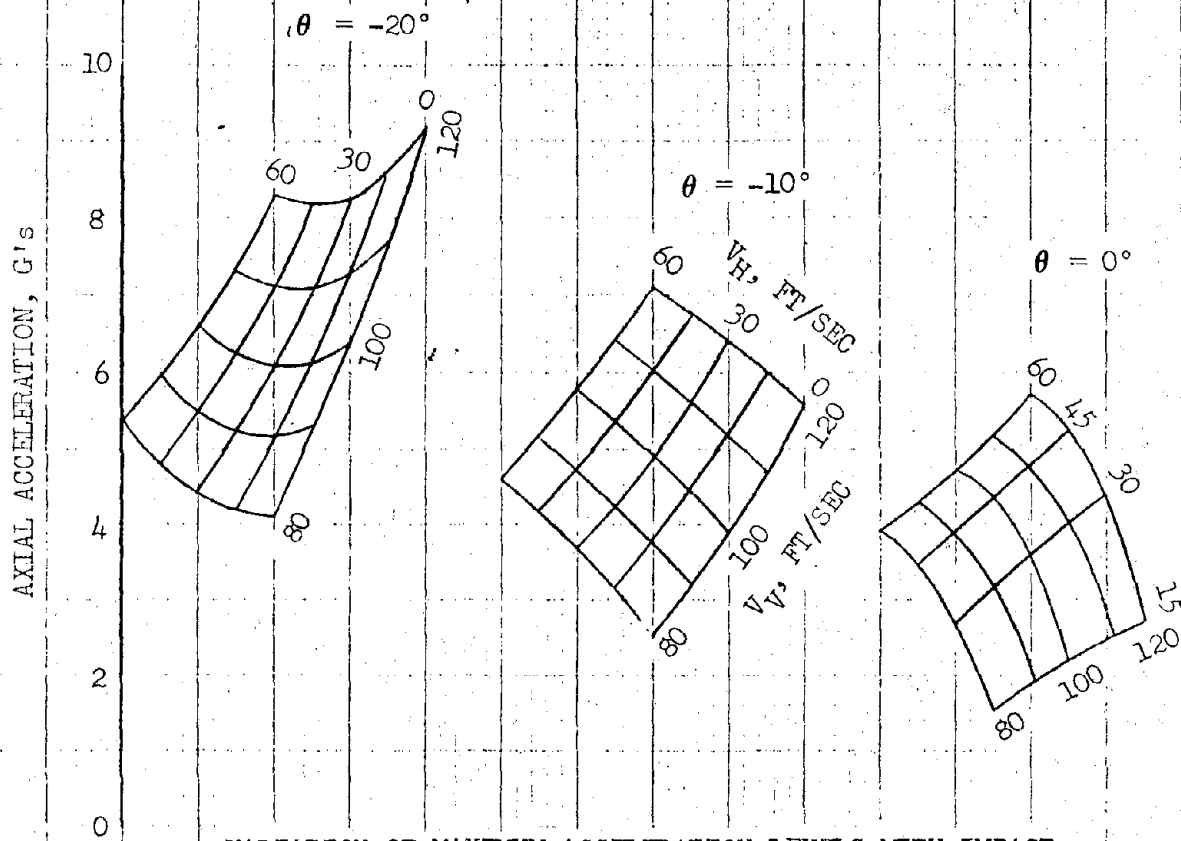
$$P = P_{\text{ambient}} = \text{const.}$$

$$\left( \begin{array}{c} 0 \leq x \leq L_N \\ -180^\circ \leq \phi \leq +180^\circ \end{array} \right)$$

NOTE: All surfaces for which pressure is not specified are subject to ambient pressure.

FIGURE 7-10 PRESSURE DISTRIBUTION AT MAXIMUM AXIAL ACCELERATION (WITH NOZZLE EXTENSION)

4/11 CONFIGURATION  
WITH NOZZLE EXTENSION

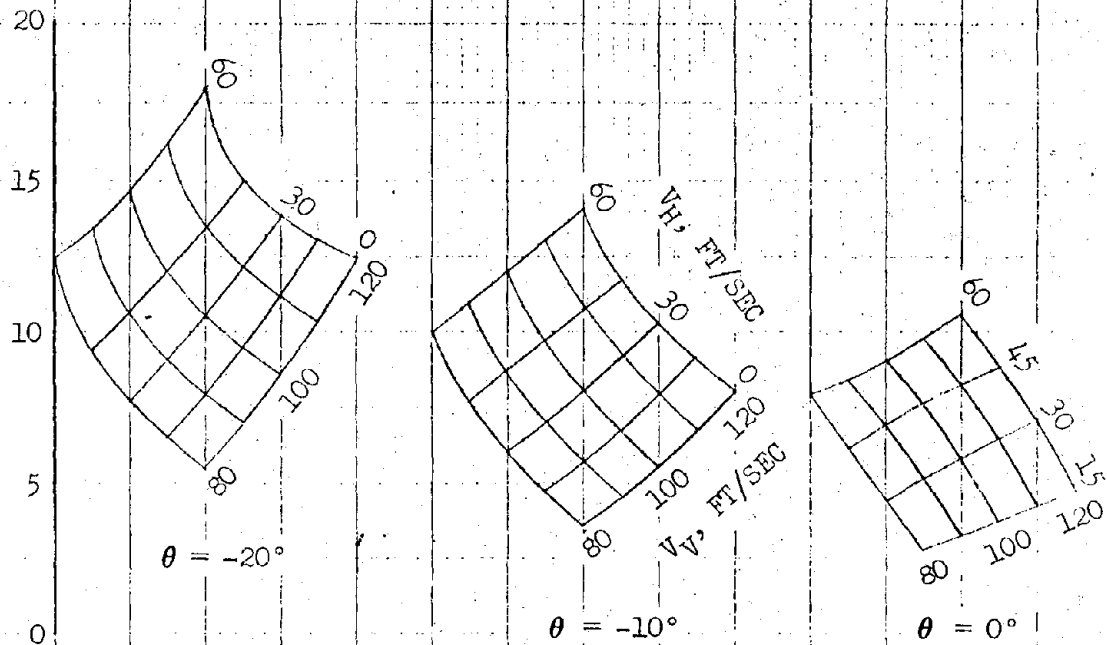


VARIAION OF MAXIMUM ACCELERATION LEVELS WITH IMPACT  
CONDITIONS - MAXIMUM PITCH ACCELERATION

FIGURE 7-11

4/11 CONFIGURATION  
WITH NOZZLE EXTENSION

PITCH ANGULAR ACCELERATION, RAD/SEC<sup>2</sup>



PITCH ACCELERATION AT C.G., G's

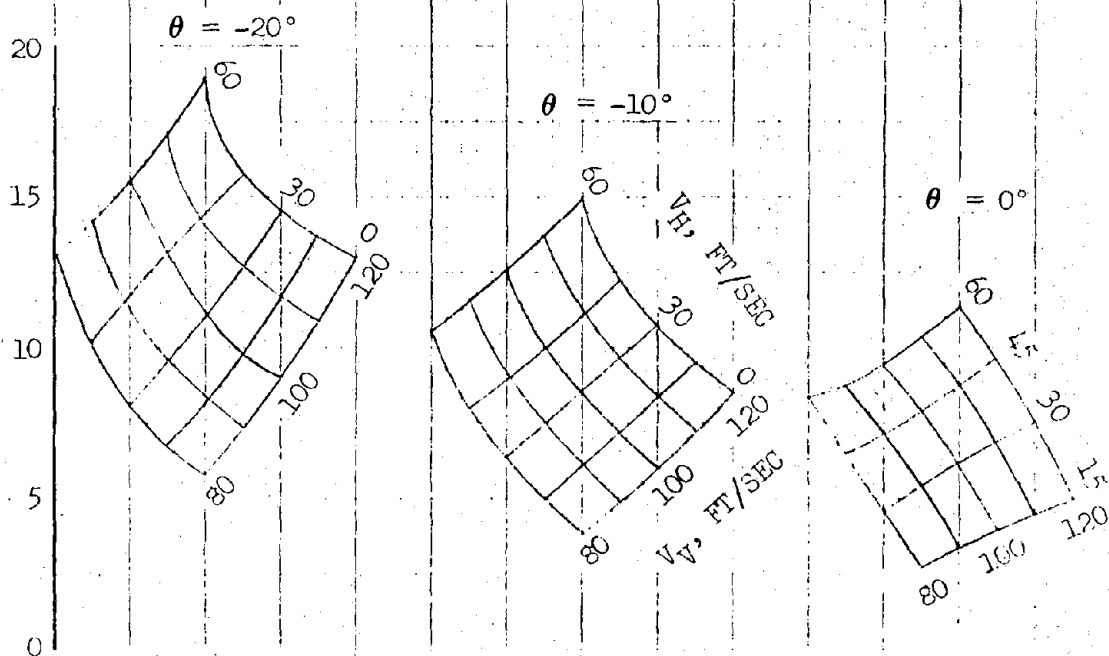
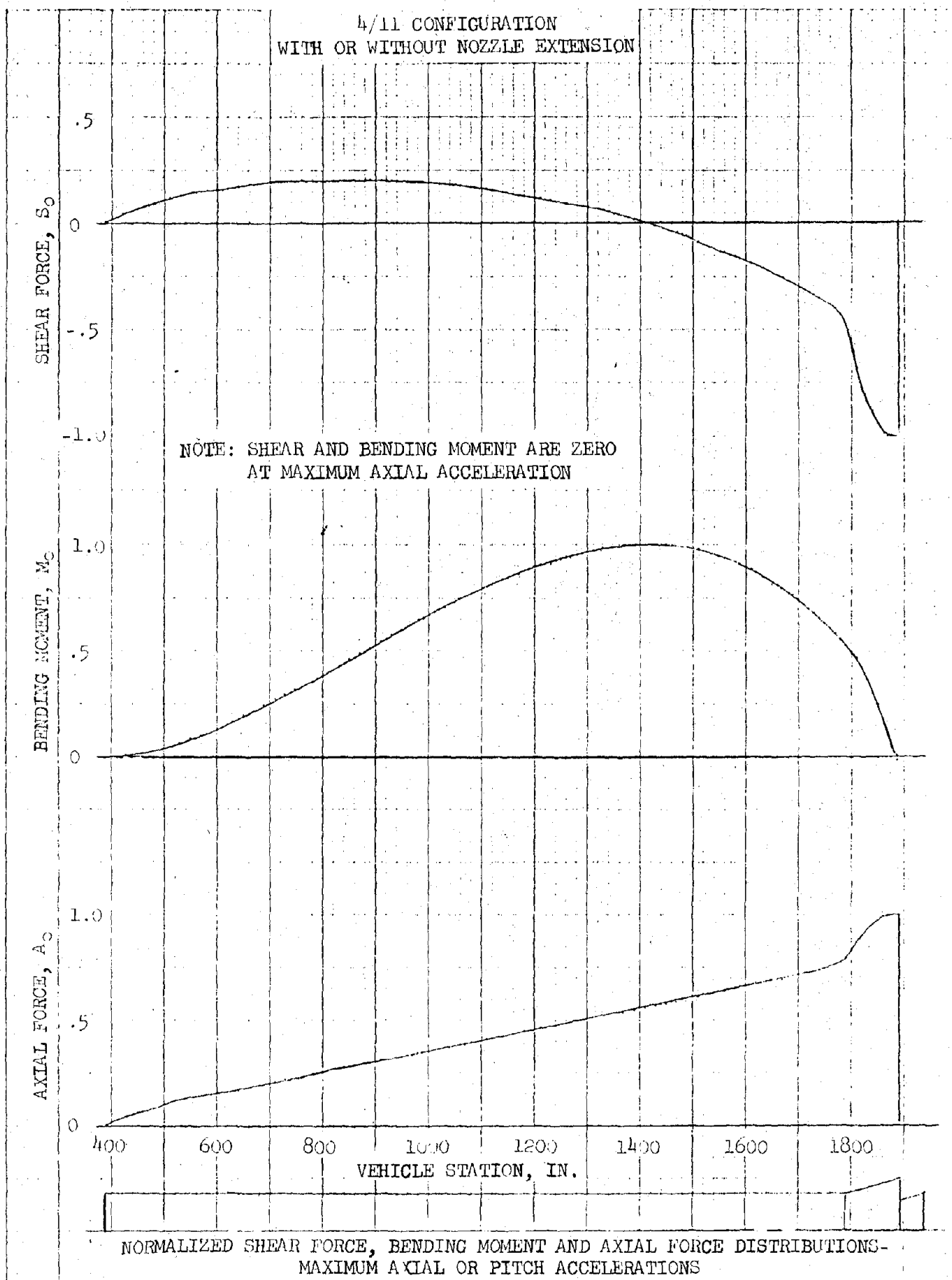


FIGURE 7-12 VARIATION OF MAXIMUM ACCELERATION LEVELS WITH IMPACT CONDITIONS - MAXIMUM PITCH ACCELERATION



—FIGURE 7-13

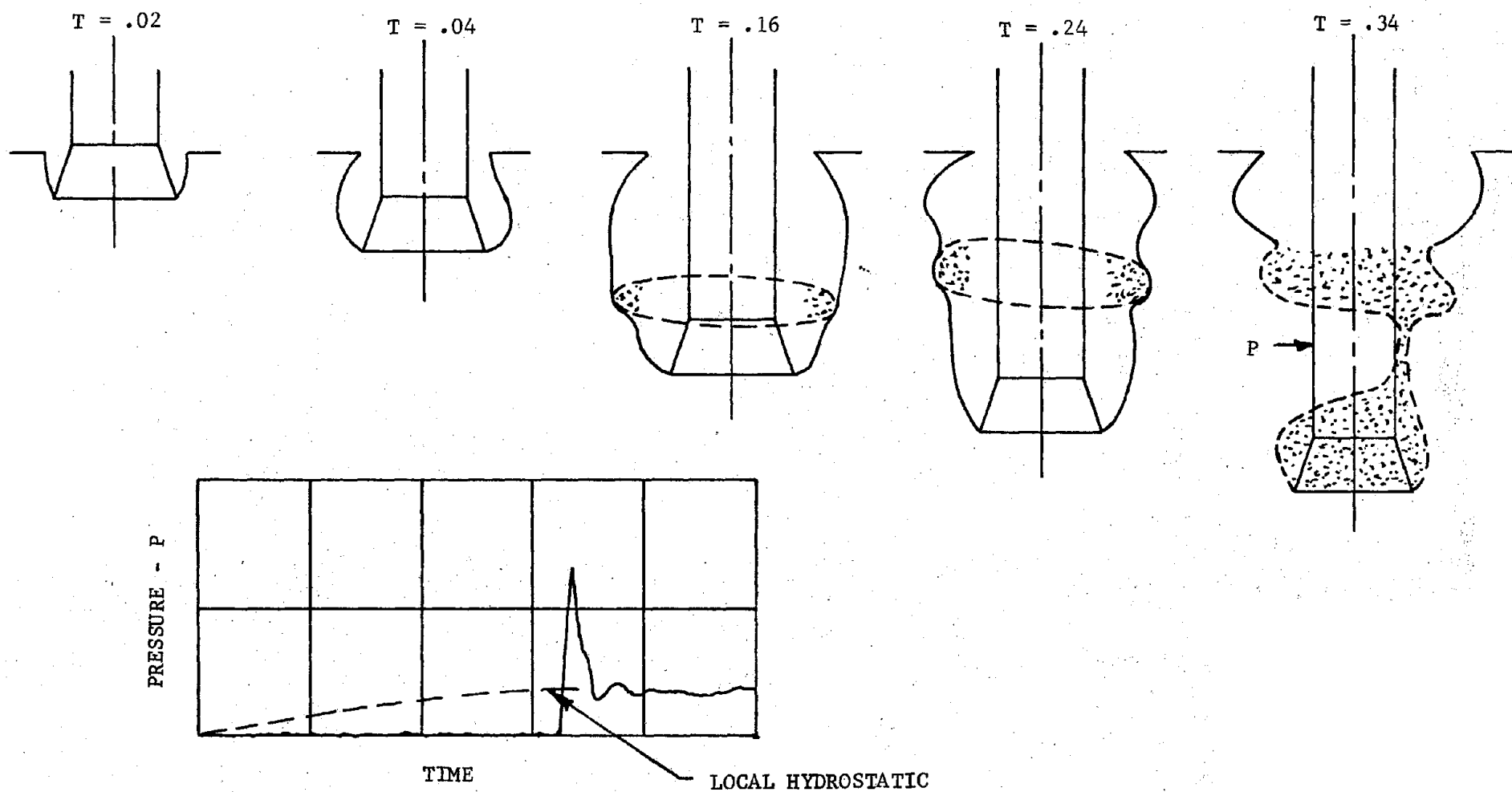


FIGURE 7-14 QUALITATIVE DESCRIPTION OF CAVITY FORMATION AND COLLAPSE  
(a) NEAR-ZERO EFFECTIVE IMPACT ANGLE

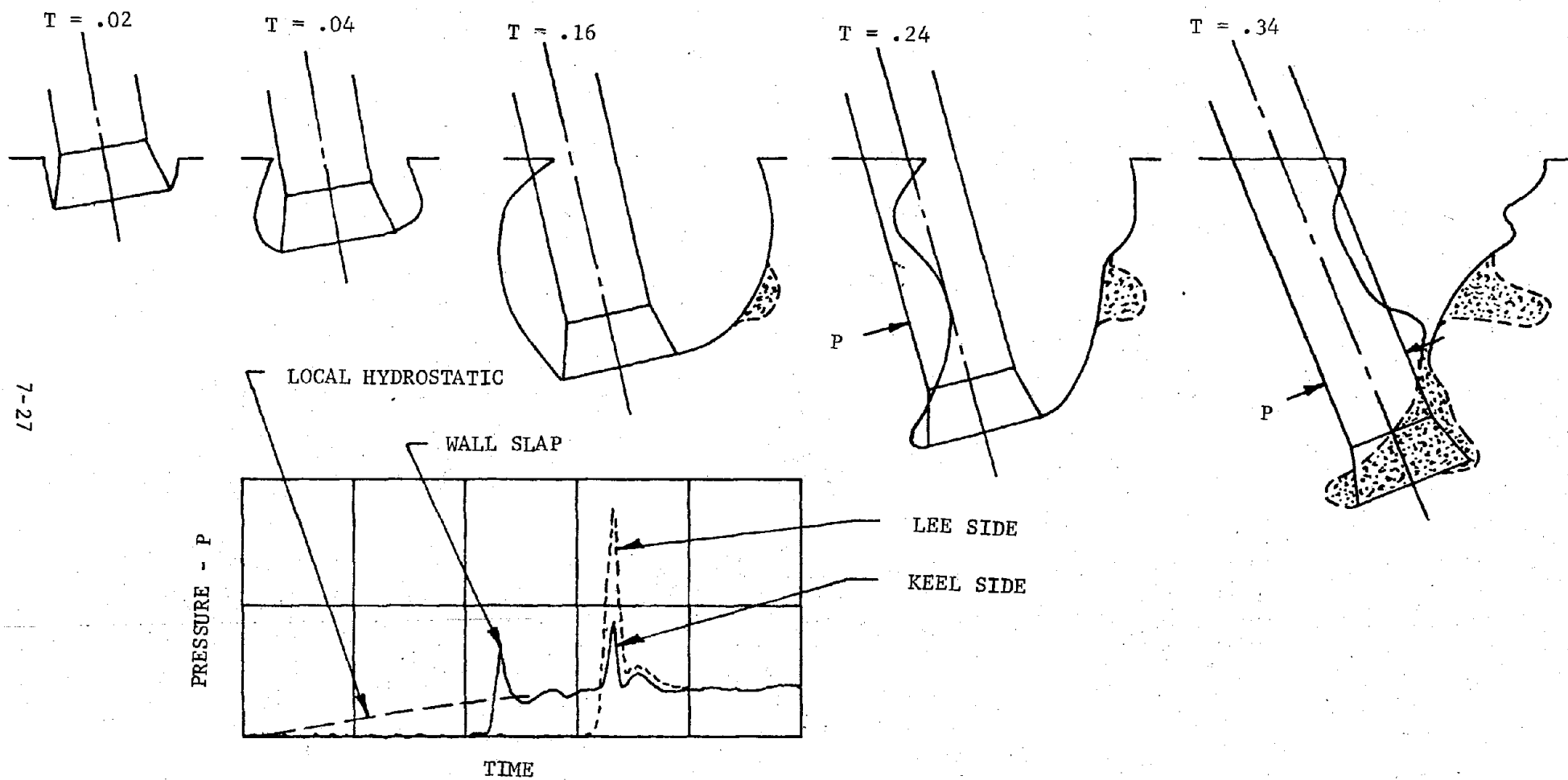


FIGURE 7-14 CONTINUED (b) MODERATE EFFECTIVE IMPACT ANGLE

CAVITY COLLAPSE RADIAL PRESSURE  
DISTRIBUTIONS AT STATION 104.2

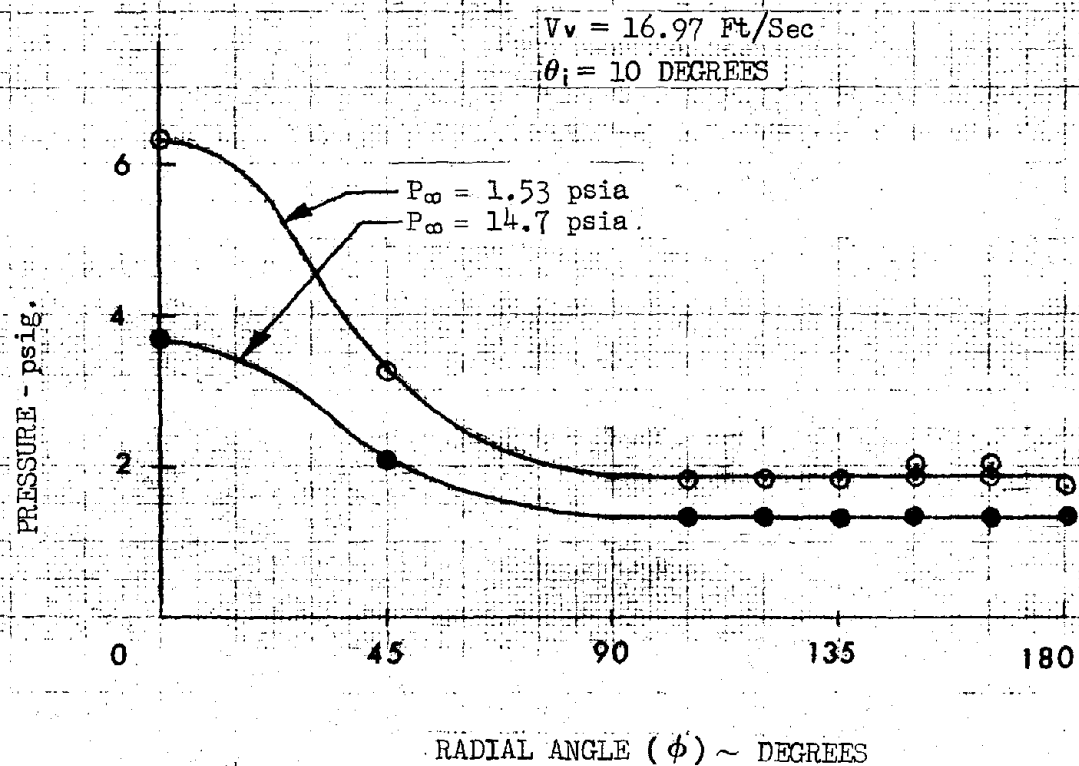
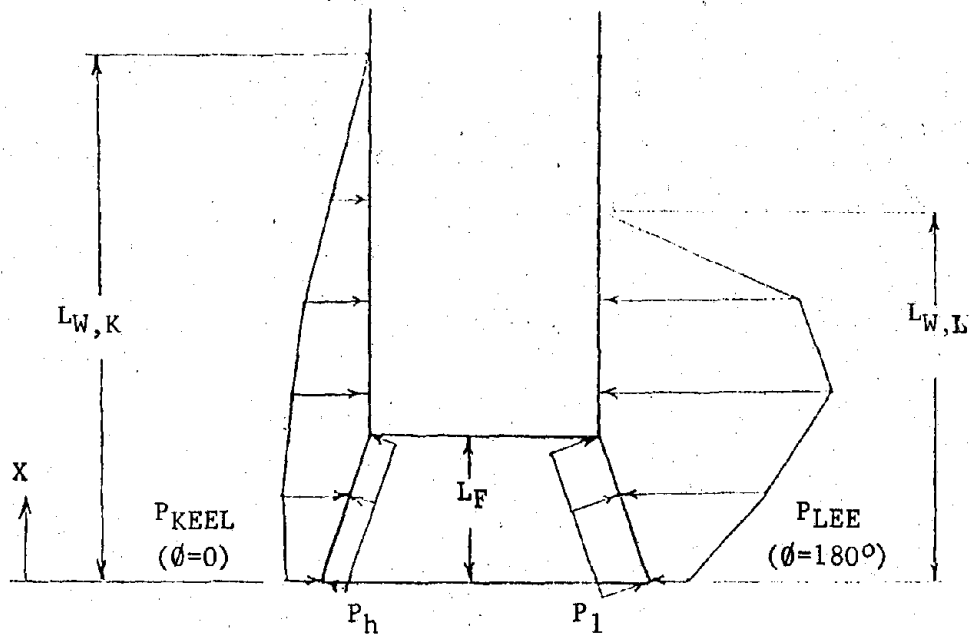


FIGURE 7-15 TYPICAL CAVITY COLLAPSE RADIAL PRESSURE DISTRIBUTION,  
NOL 12.5 INCH DIAMETER MODEL



## CAVITY COLLAPSE

### SRM CASE AND SRB AFT SKIRT PRESSURES



### INTERNAL PRESSURES

#### SRM CASE

$$P = P_{\text{PULLAGE}}, \text{ UNIFORM}$$

#### SRB AFT SKIRT

$$P = P_h + \frac{1}{2}(1 - \cos \phi)(P_1 - P_h)$$

$$0 \leq X \leq L_F, \quad -180^\circ \leq \phi \leq 180^\circ$$

### EXTERNAL PRESSURES

#### CIRCUMFERENTIAL DISTRIBUTION

$$P = P_{\text{KEEL}} + K_C (P_{\text{LEE}} - P_{\text{KEEL}}), \quad 0 \leq X \leq L_{W,L}, \quad -180^\circ \leq \phi \leq 180^\circ$$

$$P = P_{\text{KEEL}}, \quad L_{W,L} \leq X \leq L_{W,K}, \quad -\phi_w \leq \phi \leq \phi_w$$

$$K_C, \text{ SEE FIGURE III-2; } \phi_w = \cos^{-1} \left[ \frac{2(X - L_{W,L})}{(L_{W,K} - L_{W,L})} - 1 \right]$$

#### LONGITUDINAL DISTRIBUTION

SEE FIGURES FOR  $P_{\text{KEEL}}$  &  $P_{\text{LEE}}$  VS. STATION

FIGURE 7-16 CAVITY COLLAPSE PRESSURE DISTRIBUTIONS -  
SRM CASE AND AFT SKIRT PRESSURES

11/1/74 CONFIGURATION

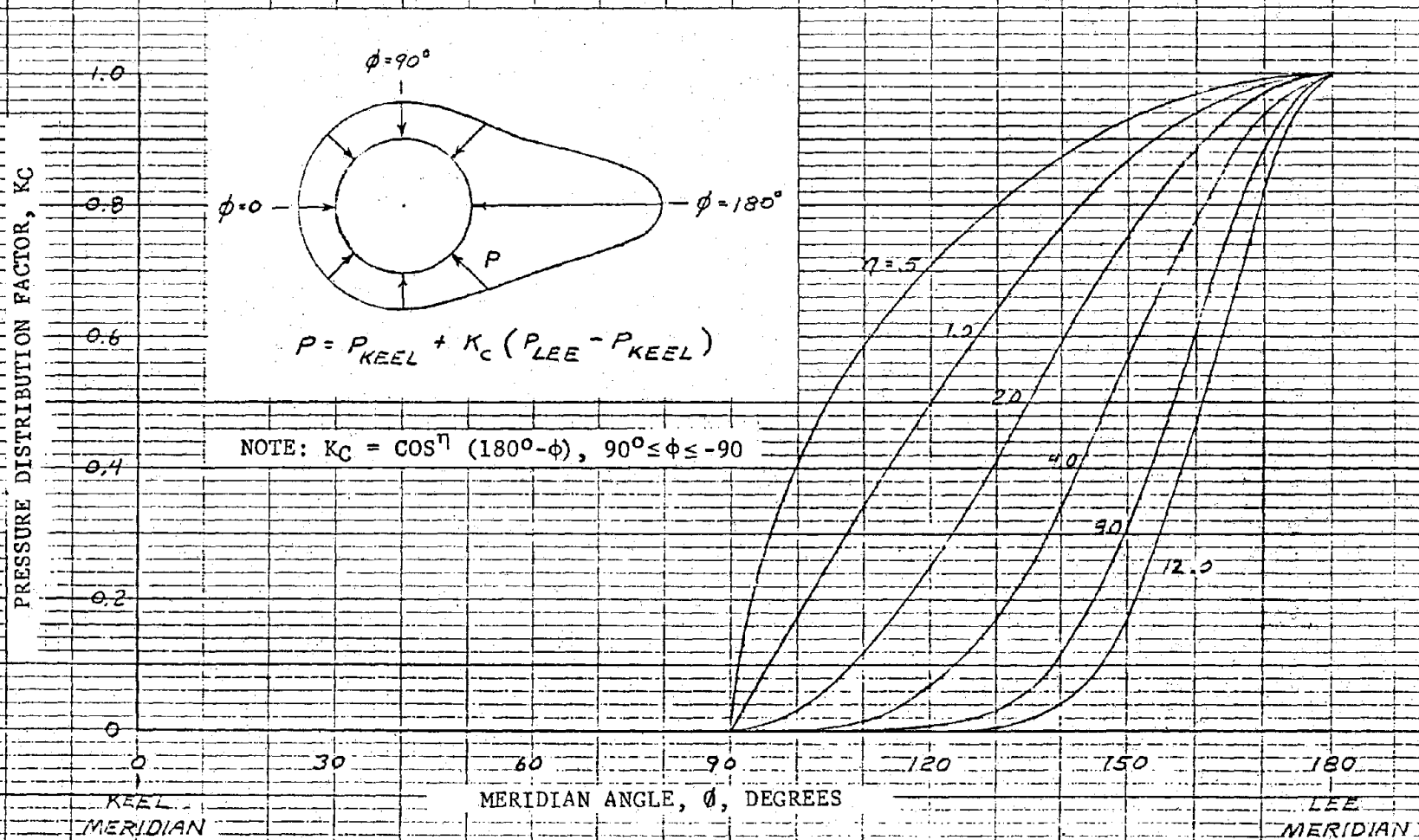


FIGURE 7-17 CAVITY COLLAPSE PRESSURE DISTRIBUTION FACTOR,  $K_c$

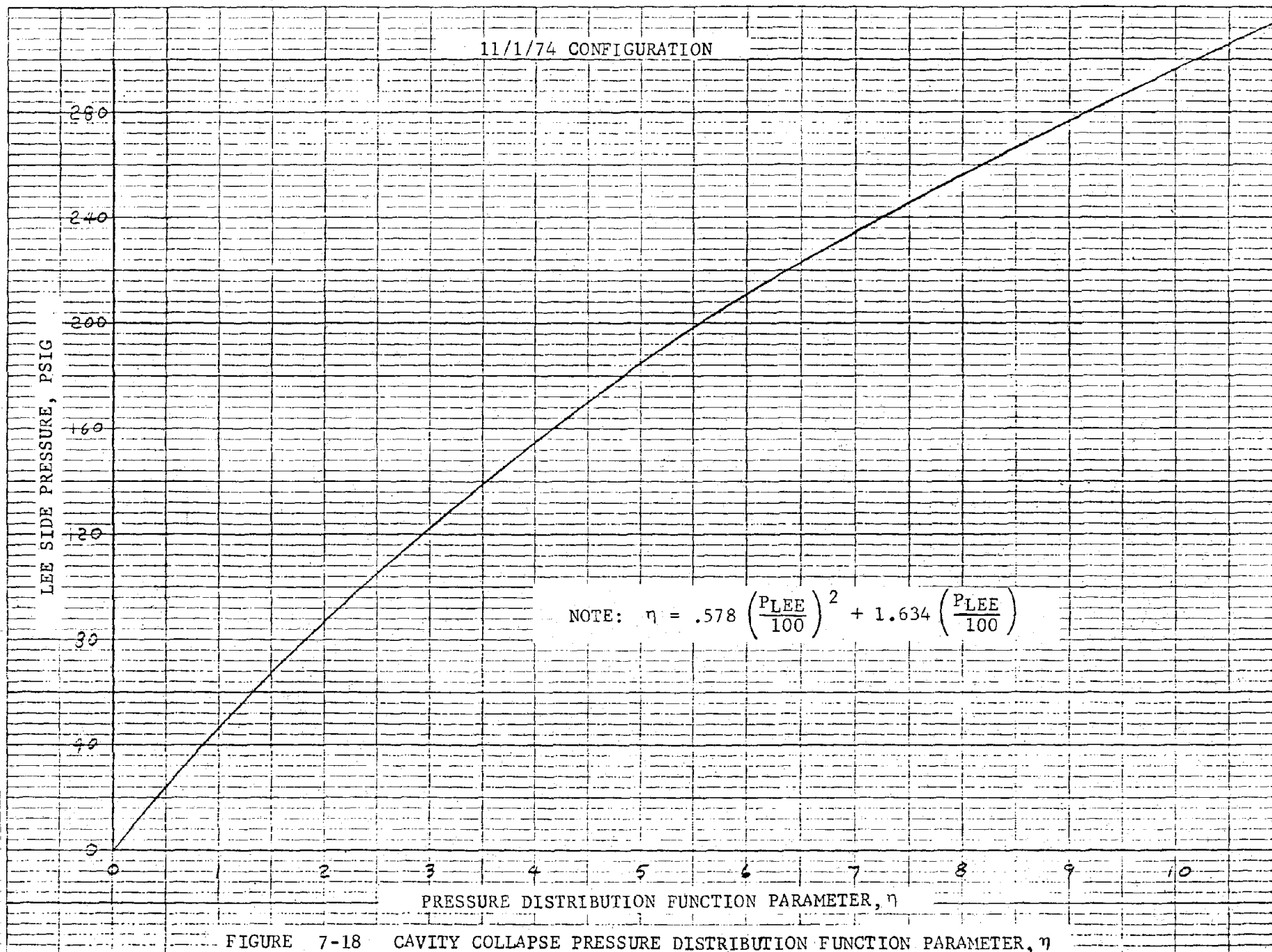
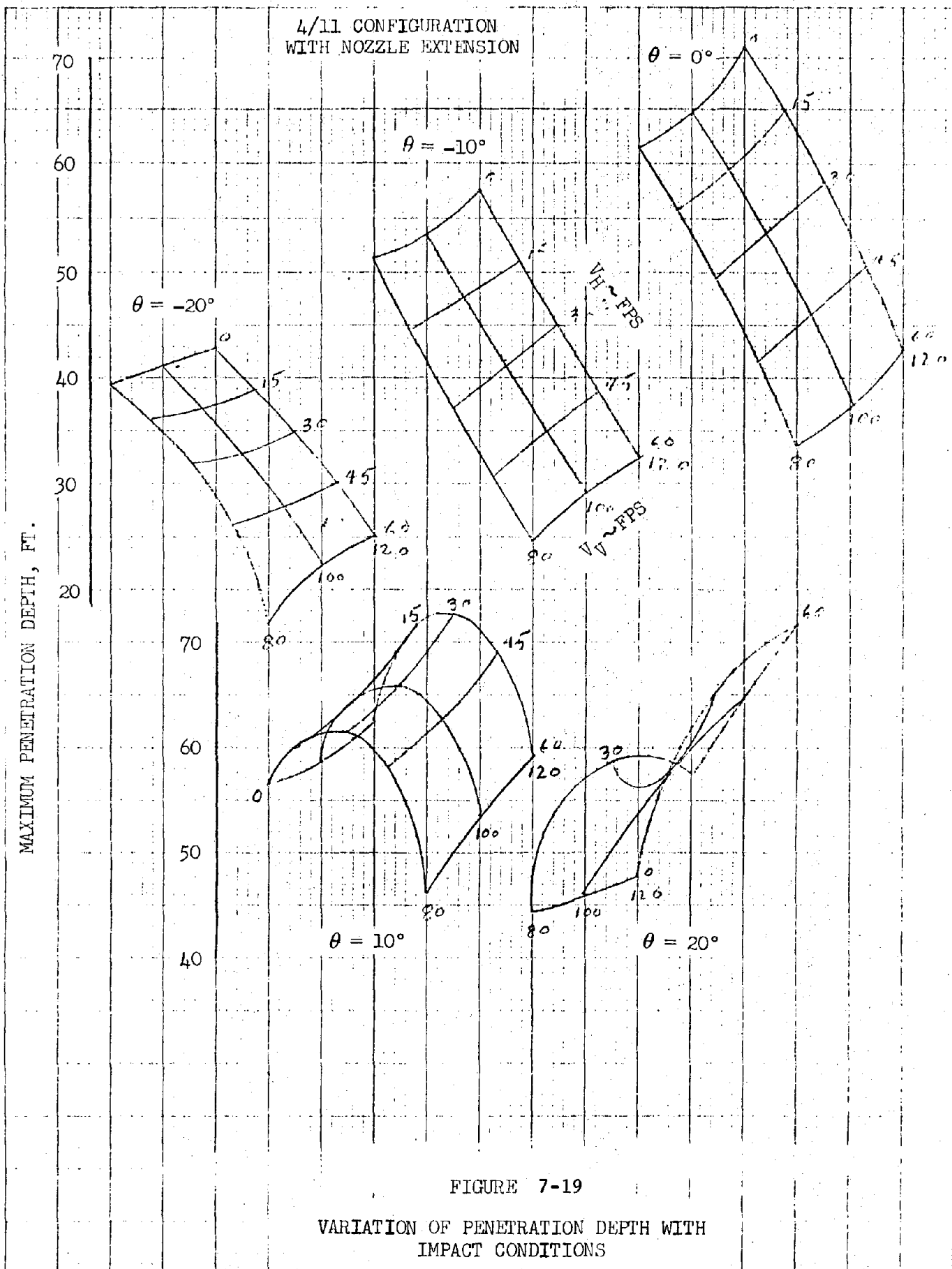
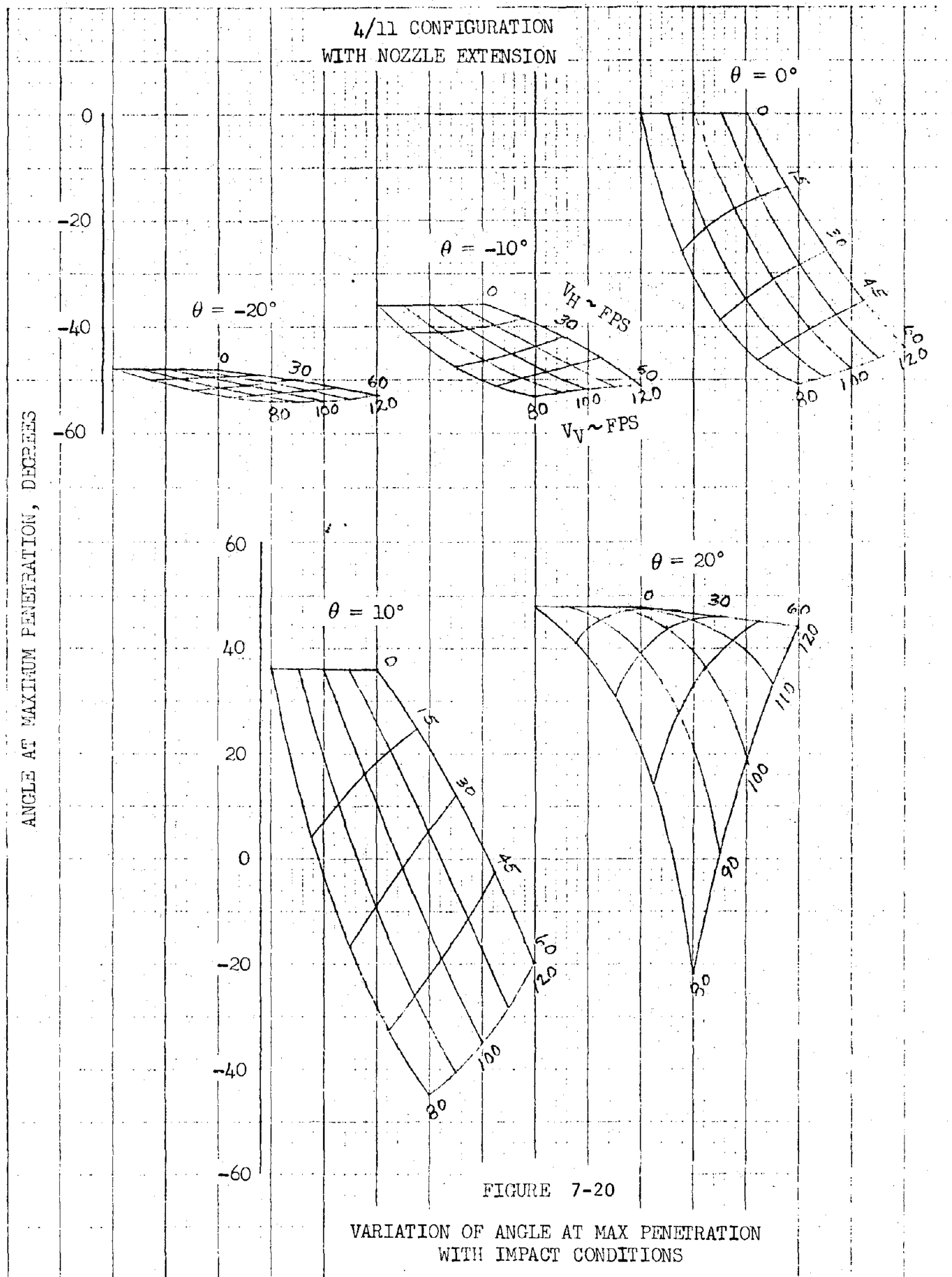


FIGURE 7-18 CAVITY COLLAPSE PRESSURE DISTRIBUTION FUNCTION PARAMETER,  $\eta$





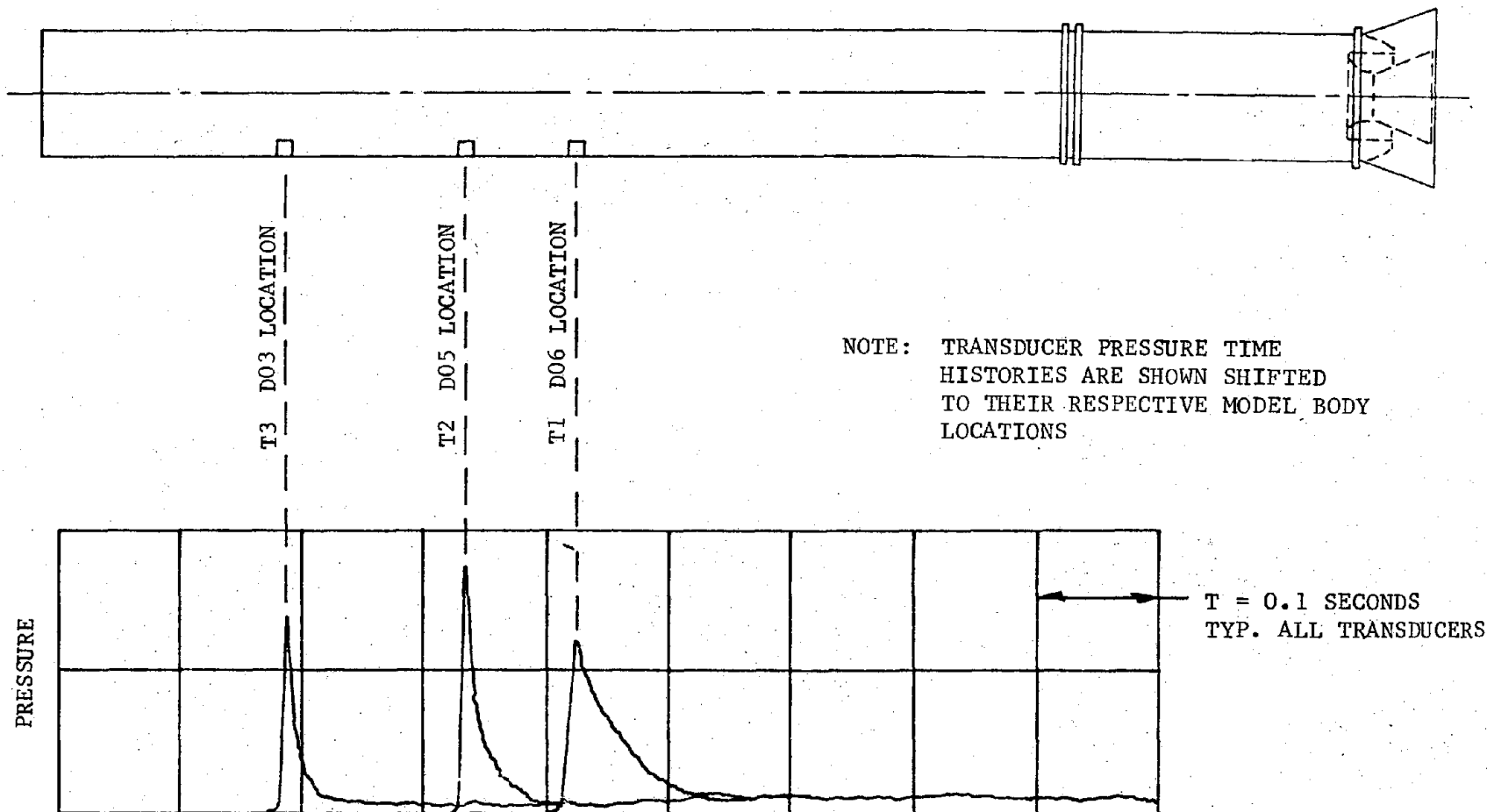


FIGURE 7-21. TYPICAL TIME HISTORIES OF SLAPDOWN PRESSURES

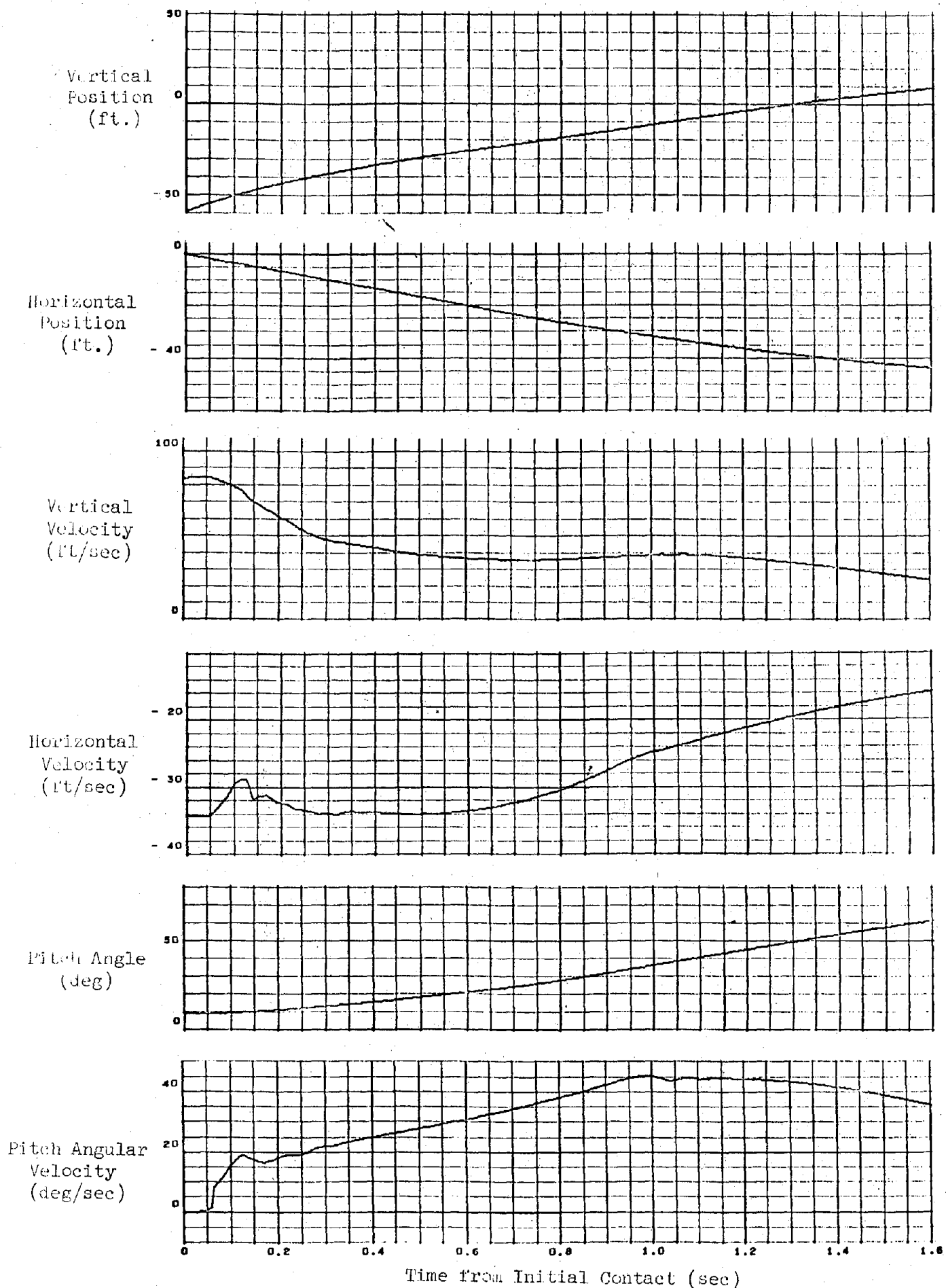


FIGURE 7-22. TYPICAL FULL SCALE TRAJECTORY FOR VEHICLE C.G., TEST P015-70

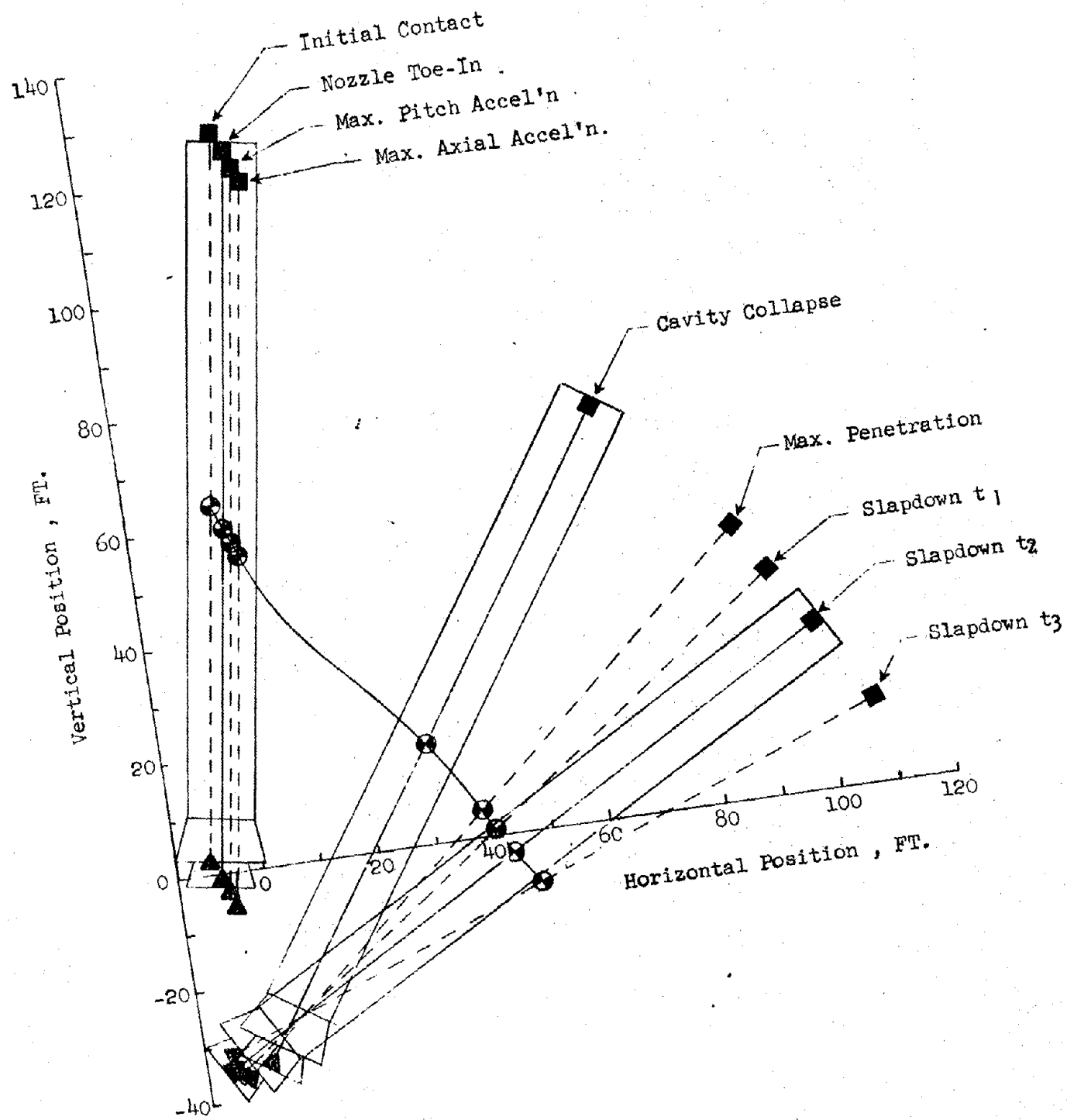


FIGURE 7-23 QUALITATIVE VEHICLE TRAJECTORY DURING IMPACT



## SECTION 8.0

### FULL SCALE LOADS

Full scale water impact loads were calculated for SRB configurations as they evolved from the initial 156 inch diameter SRB to the ~~current~~ 5/1/75 baseline configuration. These loads cover significant loading events from initial water contact through final settling in the water. A data base compiled from scale model tests and Froude scaling techniques were used to generate SRB loads as a function of water entry condition. This section presents the procedures used to calculate SRB loads in order of their occurrence from initial impact through cavity collapse, maximum penetration, and slapdown.

#### 8.1 Initial Impact

Vehicle loads at initial impact were determined at three events, maximum vehicle pitch acceleration, maximum vehicle axial acceleration, and maximum negative axial load on the nozzle. Maximum pitch acceleration was detected by all three pitch accelerometers. By definition, the time for this event is taken to be the time at which the pitch acceleration reaches a maximum. Due to the elasticity of the model structure, the time indicated for the event by the three accelerometers was not always precisely the same; under certain impact conditions, the indicated time varied by 2 to 4 milliseconds. Therefore, the output of the accelerometer located farthest aft, and therefore closest to that portion of the vehicle over which the impact loads were applied, was selected as the reference for determining the time of maximum pitch acceleration.

The time for the maximum axial acceleration event is defined as the time at which the axial acceleration reaches a maximum. This event was detected by the axial accelerometers. Generally, there was very little difference in the time indicated by all accelerometers. However, in those cases where there was some appreciable difference, the accelerometer located farthest aft was used as the reference.

At the maximum axial acceleration event the maximum positive axial and lateral loads on the nozzle also occur. As the annulus between the nozzle and skirt fills and the water head impacts the bulkhead, the forces on the nozzle reverse direction and the nozzle is pulled away from the bulkhead. This is the nozzle maximum negative axial load event and the time of this event was defined by peak negative axial load measured on the nozzle strain gage balance.

Pressures on the nozzle, skirt and bulkhead were read at the time of these three events for all pressure scaled tests. Using the actual impact conditions ( $V_V$ ,  $V_H$ ,  $\theta$ ) for each test, the resultant vehicle velocity,  $U$ , and effective impact angle ( $\alpha - \theta$ ) were calculated by:

$$U = \sqrt{V_V^2 + V_H^2}$$

$$(\alpha - \theta) = \tan^{-1} \left( \frac{V_H}{V_V} \right) - \theta$$

For maximum pitch and maximum axial acceleration events the measured pressures were nondimensionalized by the resultant dynamic pressure,  $q = \frac{1}{2} \rho U^2$ , and plotted as a function of ( $\alpha - \theta$ ). This resulted in a family of curves for each locally measured pressure with  $V_V$ ,  $V_H$ , or  $\theta$  as parameters. For

the event of maximum negative nozzle load which occurs latest in time, the effect of  $\alpha$  was small and the nondimensional pressures correlated primarily with  $\theta$ . By cross-plotting the nondimensional curves for the pressures at the transducer locations, extrapolating, and replotting, curves were constructed for axial locations coincident with nozzle throat and nozzle and skirt exit planes. Figures 8-1 thru 8-4 illustrate correlations of data at the three events. For any given set of full scale impact conditions the pertinent full scale nozzle, skirt, and bulkhead pressures were then obtained directly from the normalized curves.

The axial and pitch accelerometers were read at the three events and used to calculate axial, lateral, and angular accelerations at the dry vehicle C.G. accelerations were then divided by  $q$  and plotted VS  $(\alpha - \theta)$ . The correlated curves were used to define C.G. accelerations. The two aft model accelerometers, located at full scale station 1826, were correlated in the same manner and used to define nozzle inertial loads.

Data from the nozzle force balance was first corrected for balance interactions and nozzle inertial loads then forces and moments were transferred to the nozzle throat. These data were further adjusted to account for the compliance ring and a one foot nozzle extension resulting from redefinition of the nozzle extension separation plane. As test data was not available this adjustment was made analytically using the following equations for positive axial forces:

$$\text{Axial Force} = 2 \cdot \rho \cdot V_o^2 \left[ \frac{R_o}{r} \right]^6 \sin \alpha \cdot H \cdot \cos^3 \theta_i \int_0^\pi f(\delta_\phi) d\phi$$

$$\text{Lateral Force} = 2 \cdot \rho \cdot V_o^2 \left[ \frac{R_o}{r} \right]^6 \cos \alpha \cdot H \cdot \cos^3 \theta_i \int_0^\pi f(\delta_\phi) \cos \phi d\phi$$

$$f(\delta\phi) = \frac{1}{\sin\delta\phi} \left\{ \frac{\pi(\pi - 2\delta\phi)}{\sin 2\delta\phi [\Gamma(1 - \delta\phi/\pi) \cdot \Gamma(\frac{1}{2} + \delta\phi/\pi)]^2} - 1 \right\}$$

Where:

- $\Gamma$  - Gamma Function (See Figure 8-32)
- $\rho$  - Water density
- $V_0$  - Impact velocity
- $R_0$  - Nozzle exit radius
- $\bar{r}$  - Nozzle mid point radius
- $H$  - External free surface penetration
- $\theta_i$  - Impact angle
- $\delta$  - Flow directional angle
- $\phi$  - Radial angle

Negative axial force was calculated by:

$$F_{xnet} = \rho \cdot V_0^2 [ A_{pext} + 1/2 \cdot C_{pwed} (R_0/\bar{r})^4 \cdot A_{pint} ]$$

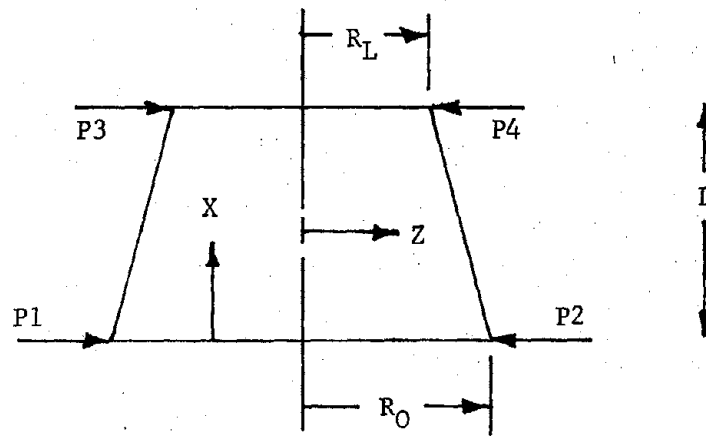
Where:

- $A_{pext}$  = Axial projection of exposed external nozzle surface area
- $C_{pwed}$  = Pressure coefficient on equivalent wedge surface
- $A_{pint}$  = Axial projection of nozzle internal surface area

The above equations using dimensions for the tested 11/1/74 and 5/1/75 baseline configurations indicate a 39% increase in nozzle loads during the positive axial force loading and a 29% increase for the negative axial nozzle load event. All applied nozzle forces and moments were then increased by these percentages.

The correlated model pressure, force, and acceleration data was then Froude scaled to full scale SRB values and used as inputs to the initial impact pressure integration program. The program simulates the SRB

skirt/nozzle area geometry as a series of conical frustums and rings. The skirt is modeled as two frustums and three rings, the aft closure is modeled as one frustum and one ring, the internal nozzle is modeled as two frustums, and the external nozzle is modeled as one conical frustum. Four pressures act on each frustum and ring assuming a  $\cos \phi$  distribution circumferentially and a linear distribution axially. A typical frustum segment is shown below.



The pressure distribution is defined by:

$$P = P_1 + (P_2 - P_1) \frac{(1 - \cos \phi)}{2} + \left\{ [P_3 + (P_4 - P_3) \frac{(1 - \cos \phi)}{2}] - [P_1 + (P_2 - P_1) \frac{(1 - \cos \phi)}{2}] \right\} \frac{X}{L}$$

This equation defines a  $(1 - \cos \phi)$  distribution for  $0 \leq \phi \leq 180^\circ$  and a linear distribution for  $0 \leq X \leq L$ . Integrating the pressures over the frustum surface results in loads defined by:

$$F_x = (-1)^n \frac{\pi}{3} (R_O - R_L) [3 (R_O + R_L) P_1 + (R_O + 2 R_L) (P_3 - P_1)] + (-1)^n \frac{\pi}{6} (R_O - R_L) [3 (R_O + R_L) (P_2 - P_1) + (R_O + 2 R_L) (P_4 - P_3 - P_2 + P_1)]$$

$$F_z = (-1)^n \frac{\pi}{12} L \left[ 3(R_o + R_L)(P_2 - P_1) + (R_o + 2R_L)(P_4 - P_3 - P_2 + P_1) \right]$$

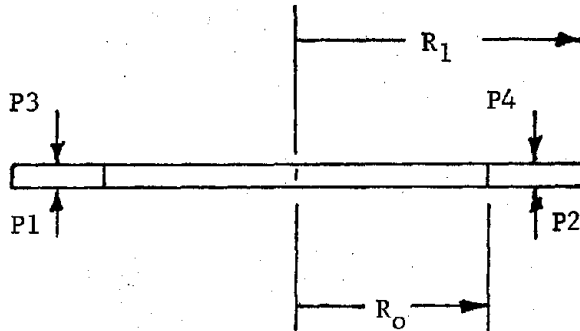
$$M_x = (-1)^n \frac{\pi}{24} (R_o - R_L) \left[ 4(R_o^2 + R_o R_L + R_L^2)(P_2 - P_1) \right. \\ \left. + (R_o^2 + 2 R_o R_L + 3 R_L^2)(P_4 - P_3 - P_2 + P_1) \right]$$

$$M_z = F_z x_{cg} + (-1)^{n+1} \frac{\pi}{24} L^2 \left[ 2(R_o + 2R_L)(P_2 - P_1) \right. \\ \left. + (R_o + 3 R_L)(P_4 - P_3 - P_2 + P_1) \right]$$

$$M_{cg} = M_x + M_z$$

For external surfaces  $n$  is an odd integer and for internal surfaces  $n$  is an even integer.

The ring segments shown below assume a  $(1 - \cos \phi)$  distribution over the upper and lower surfaces.



Integrating the pressures over the ring surface results in:

$$F_x = \frac{\pi}{2} (R_1^2 - R_o^2) \left[ (P_1 - P_3) + (P_2 - P_4) \right]$$

$$F_z = 0$$

$$M_x = \frac{\pi}{6} (R_1^3 - R_o^3) \left[ (P_2 - P_4) + (P_3 - P_1) \right]$$

$$M_z = 0$$

$$M_{cg} = M_x$$

The program calculates applied nozzle loads and total vehicle axial and normal forces and the pitching moment about the C.G. The SRB mass and pitch moment of inertia are used to calculate total vehicle axial, lateral and angular accelerations. The calculated accelerations and nozzle applied loads from pressure integrations were compared to the correlated accelerometer readings and nozzle strain gage loads. The pressures were then tempered within an allowable range of  $\pm 10\%$  until the integrated loads agreed with measured forces and accelerations. The pressures, vehicle accelerations, and nozzle loads were then carpet plotted as functions of impact conditions.

The initial loads documentation presented data for  $V_v = 80, 100, \text{ and } 120$  FPS. For each vertical velocity data was presented for  $V_H = 0, 15, 30, 45, \text{ and } 60$  FPS and  $\theta_i = -10, -5, 0, 5, \text{ and } 10^\circ$ . Finalization of the SRB parachute design resulted in a nominal vertical impact velocity of 85 FPS with a maximum expected deviation of  $\pm 5$  FPS, and a new set of water impact loads was prepared presenting data for  $V_v = 80, 85, \text{ and } 90$  FPS. These data were derived from a direct  $q$  interpolation of the  $V_v = 80$  and 100 FPS. The data presentation consisted of vehicle C.G. accelerations, 15 pressures in the nozzle/skirt annulus, applied nozzle loads, and inertial nozzle loads.

The previously described loads were derived from test data utilizing a model with a rigid concentric nozzle. However, the full scale nozzle is not rigid and will deflect up to  $\pm 5^\circ$  as a function of the dynamic response.

characteristics of the gimbal system and the applied load transient during impact. Therefore, nozzle loads incorporating the effect of nozzle motion were defined on the basis that:

1. Overall vehicle dynamics are not significantly influenced by nozzle deflections of less than  $5^\circ$  in either plane.
2. Nozzle applied axial load is primarily a function of total vehicle impact velocity vector and nozzle pitch plane attitude. Nozzle deflections in the yaw plane of less than  $5^\circ$  are insignificant to the magnitude of this force.
3. Only the initial phase of the nozzle applied load pulse, during nozzle filling, is significantly affected by nozzle vectoring. That portion of the nozzle load transient due to stagnation of the nozzle/skirt annulus flow is not affected by deflections of the nozzle less than  $5^\circ$  in either plane.
4. The component of nozzle lateral force in the yaw plane due to vectoring out of the pitch plane is dependent only on vehicle vertical impact velocity and not significantly affected by the horizontal drift velocity component or initial impact pitch plane attitude.

Within these assumptions, nozzle total applied load at any time (t), can be defined as the sum of the axial force component (not significantly affected by nozzle vectoring); the lateral force component in the vehicle pitch plane (defined by the total velocity vector and nozzle pitch plane attitude) and the lateral force component in the yaw plane (determined only



by yaw plane deflection angle and vertical velocity component). The total force vector can then be written as,

$$F = A_a (V_v, V_H, \theta_i, \alpha_n) + N_a (V_v, V_H, \theta_i, \alpha_n) + Y_a (V_v, \beta_n)$$

where  $\alpha_n$  and  $\beta_n$  are the respective angular deflections in each plane at any given time,  $t$ ; and  $V_v$ ,  $V_H$ , and  $\theta_i$  are initial vehicle water impact conditions.

The applied load moment about the nozzle throat centerline reference point may also be expressed as,

$$M = m_a (V_v, V_H, \theta_i, \alpha_n) + n_a (V_v, \beta_n)$$

Although nozzle loads vary with impact conditions, the load time history for each component can be represented by one of two characteristic shapes. One curve for impact conditions when  $V_H = 0$  or  $\theta_i$  is less than or equal to zero and one curve for impact conditions with positive values of  $V_H$  and  $\theta_i$ . Applied load time histories were normalized to the peak positive and negative magnitudes of the pulse, and the traces were shifted slightly to make the peaks of the axial and lateral forces time consistent for each case. The inertial time histories were normalized to the magnitude of the peak negative load.

Plots of the magnitude of the first and second applied load peaks were prepared for axial force and lateral force and moment in the pitch plane. These data which were presented for an impact angle range of  $\pm 15^\circ$  were derived from extrapolation of  $\pm 10^\circ$  data. Lateral forces and moments in the yaw plane were taken from the slope of applied normal force and pitching moment data for  $V_H = 0$  FPS. The slope of this data is linear over the range of  $\pm 10^\circ$  and yaw plane forces were expressed as:

$$\text{Yaw force} = 8.4 V_v^2 \beta_n$$

$$\text{Yawing Moment} = 368 V_v^2 \beta_n$$

where:

$V_v$  = Vertical velocity in ft/sec

$\beta_n$  = Nozzle deflection angle in degrees

Nozzle response loads were calculated using a dynamic computer model of the SRB. This math model simulated the geometry, mass, and stiffness of the SRB aft closure, skirt, heat shield, nozzle, nozzle actuators, flex bearing, gimbal stops and the snubber. The elasticity of the model components was assumed to be linear regardless of the load range. The normalized time histories of applied and inertial nozzle loads along with peak value force and moment data as a function of impact condition were used to calculate the time variant nozzle loads. This was an iterative procedure beginning at  $T = 0$  calculating the nozzle loads and applying them to the nozzle until time  $T_i$  when the nozzle deflects to  $\alpha_i, \beta_i$ . The new values of  $\theta_i + \alpha_i$  and  $\beta_i$  were used to reenter the peak load data arrays and determine updated peak nozzle loads. These were multiplied times normalized nozzle loads at time  $T_{i+j}$  and new nozzle deflection angles ( $\alpha_{i+j}, \beta_{i+j}$ ) were calculated.

The loads were updated until the nozzle axial load reversed. At this time stagnation is occurring in the nozzle skirt annulus and nozzle loads are dependent only upon initial impact conditions. The peak nozzle loads at maximum negative nozzle axial force were multiplied times the normalized time histories for the remainder of the impact.

Nozzle response loads were calculated for  $V_v = 85$  FPS,  $V_H = 5, 20$  and  $45$  FPS,  $\theta_i = -5^\circ, 0^\circ$ , and  $+5^\circ$ , and a vehicle flight path angles relative to the nozzle E actuator of  $45^\circ, 90^\circ, 135^\circ, 180^\circ$ , and  $225^\circ$ . Forces and

moments along the x, y, and z axes were calculated for the flex bearing, aft closure, flex bearing aft end ring, and nozzle snubber ring. Contact forces were calculated for the snubber along with axial forces for the nozzle actuators. Peak values of the forces and moments were smoothed and carpet plotted as functions of entry condition and flight path angle.

## 8.2 Cavity Collapse

As described in Section 5, the cavity collapse load event is a result of a high speed entry into the water by the SRB which generates a large open (ventilated) cavity during the entry phase. For a pure vertical entry ( $V_H = 0$ ,  $\theta_i = 0$ ) the cavity development and collapse is axisymmetric with the cavity wall collapsing on approximately the aft 2 diameters of the vehicle.

For moderately non-vertical entries ( $\alpha - \theta \cong 10^\circ$ ) the cavity collapses on itself along a line slightly inclined to the vehicle surface and emanating from the lee side of the vehicle base. The pressures associated with these conditions are much higher than for a pure vertical entry but are localized near the leeward meridian and about one vehicle diameter forward of the base. For large effective entry angles ( $\alpha - \theta \gg 10^\circ$ ), the cavity collapses along a line inclined at a large angle to the vehicle and significant pressures are experienced only on the lee side near the base of the vehicle.

Cavity collapse does not occur simultaneously along the vehicle for any of the entry conditions but generally occurs within about a 10 msec. (model scale) time span. Circumferential pressures do peak simultaneously, however, and since the critical loading is expected to be in the circumferential direction (i.e. a ring load), the peak cavity collapse pressures over the 10 msec. time span were combined and considered a distinct event.

The pressure pulse associated with cavity collapse is approximately triangular with about a 15 to 20 msec. (model scale) pulse duration. A simple one dimensional analysis of the response of the full scale vehicle first ring mode to this loading indicates that the equivalent static loading corresponding to the dynamic load is very nearly equal to the peak load and peak pressures were therefore taken to be representative of equivalent static pressures. A more rigorous structural dynamic analysis to cavity collapse loading is of course recommended to establish the validity of this simplified approach.

Analysis of the pressure data consisted of plotting longitudinal and circumferential distributions of peak pressures at the measurement stations on the model. At each station there were three transducers located at the  $0^\circ$ ,  $180^\circ$  and  $210^\circ$  meridian locations. In addition, many of the drop conditions were repeated with the aft model section rotated  $120^\circ$ . Combination of the data for these two drops would, with the assumption of planar symmetry, theoretically yield data at  $30^\circ$  meridional increments. It was found, however, that lack of repeatability of drop conditions for the  $120^\circ$  rolled cases and steep pressure gradients near the collapse meridian combined with off nominal roll and yaw angles precluded a direct measurement of maximum lee side pressure and distributions for each drop condition. The approach used therefore was to select those drop conditions where near nominal (zero) roll and yaw conditions were attained to define peak pressures and distributions and then use correlations to define other drop conditions.

Significant features of these distributions are the very high pressure gradients near the leeward meridian and the nearly constant levels on the windward side. The rate of fall-off of lee side pressure was found

to be proportional to the peak pressure and is attributed to the rapid diffusion of energy with distance associated with cavity collapse lines in close proximity to the SRB.

The circumferential pressure distribution was math-modeled as being constant on the keel side ( $-90^\circ \leq \phi \leq 90^\circ$ ) and varying on the lee side as

$$P = P_K + (P_L - P_K) \cos^n (180^\circ - \phi), \quad 90^\circ \leq \phi \leq -90^\circ$$

The exponent,  $n$ , was obtained from correlations of the circumferential pressure distribution (as measured by the lee side pressure drop,  $P(\phi = 180^\circ) - P(\phi = 210^\circ)$ ) with the magnitude of the lee side pressure.

A correlation parameter,  $\frac{\alpha}{2} - \theta_{cc}$ , was found which correlated the effects of initial horizontal velocity and pitch angle on cavity collapse pressures and loads. The significance of this correlation parameter is that it is an approximate measure of the angle between the cavity collapse line ( $\frac{\alpha}{2}$  from the vertical) and the vehicle centerline ( $\theta_{cc}$  from the vertical), and thus is a measure of the proximity of the cavity collapse line to the vehicle.

Correlations of maximum lee side pressures with  $\frac{\alpha}{2} - \theta_{cc}$  are shown in figure 8-5. At low values of  $\frac{\alpha}{2} - \theta_{cc}$ , the cavity collapses on the vehicle axisymmetrically and maximum pressures are 9 and 11 psig for  $V_V = 80$  and 100 fps. At moderate  $\frac{\alpha}{2} - \theta_{cc}$ , on the order of 10 to 20°, the cavity collapses on itself near the lee side and maximum pressures rise to 18 to 22 psig. The higher maximum pressures associated with these conditions are attributed to the concentration of the collapse energy near the lee

side. Most of the data for  $\frac{\alpha}{2} - \theta_{cc}$  greater than  $20^\circ$  was only run at ambient atmospheric pressure and not at the pressure scaled ambient pressure required for scaling the cavity collapse phenomena. In the absence of pressure scaled data for these conditions, the ambient atmospheric runs were assumed to be representative and the curves were faired into this data.

The above correlation was used to determine maximum lee side pressures for all conditions. The measured lee side pressures were then proportioned to match the correlated maximum value and used with measured windward pressures to define the longitudinal distributions along the windward and leeward meridians. Aft of the lee side wetted length,  $L_{W,L}$ , equation

$$P = P_K + (P_L - P_K) \cos^n (180^\circ - \phi)$$

was used to define the circumferential distribution. Forward of the lee side wetted length, the pressure varied little with meridian angle and was taken to be constant from the windward meridian to the wetted angle,  $\phi_w$ , where

$$\phi_w = \cos^{-1} \left[ \frac{2(X - L_{W,L})}{(L_{W,K} - L_{W,L})} \right]$$

This definition of  $\phi_w$  assumes that the cavity wall intersects the vehicle along a planar surface between the windward and leeward wetted lengths,  $L_{W,K}$  and  $L_{W,L}$  respectively.

Vehicle accelerations at cavity collapse were evaluated from the peak normal accelerations measured by the two aft pitch accelerometers. These readings were used to calculate angular and normal accelerations at the dry vehicle C.G. The C.G. accelerations were then plotted as a function

of  $\frac{\alpha}{2} - \theta_{cc}$  and curves were faired through the data for vertical impact velocities of 80 and 100 ft/sec. Data for  $V_y = 120$  ft/sec was extrapolated from the curves for  $V_y = 80$  and 100 ft/sec.

The correlated pressure and acceleration data were then Froude scaled to full scale values and input to a computer program for calculation of cavity collapse loads. This program considers the SRB to be a rigid body with pressure and inertial forces concentrated at discrete points, located 20 inches on center. Only forces normal to vehicle center line are considered.

Inputs to the loads program are:

- a. SRB mass distribution as a function of vehicle station.
- b. Onboard water as a function of vehicle station.
- c. Lee and keel side wetted lengths.
- d. Lee and keel side longitudinal pressure distributions.
- e. Normal and angular accelerations at the vehicle C.G.
- f. Pressure integration factors as a function of wetted lengths and local lee side pressure.

The program calculates the vehicle C.G. and pitch moment of inertia, and the local pressure and inertial shear forces at each 20 inch body section. The local shears are then integrated longitudinally to determine the net lateral load and the centroid of application for the pressure and inertial loads. The net loads are then compared and all input pressures are ratioed so that the net pressure load is equal to the net inertial load, and the vehicle angular acceleration is adjusted so that the centroids of the two shear diagrams match. The adjusted pressure and inertial

shears are then combined and total vehicle shear and bending moment diagrams are calculated.

If the pressure and inertial forces balanced within 3% the input data was considered satisfactory. If the load balance was not satisfactory, the input data was reviewed and individual pressures and/or accelerations were adjusted, generally less than 10%, and a new set of vehicle loads was calculated.

The output from the cavity collapse loads program are presented as plots of lee side pressure distribution, keel side pressure distribution, pressure shear diagram, inertial shear diagram, total vehicle shear diagram, and total vehicle bending moment diagram. Figure 8-7 illustrates typical results from the loads program.

Initially cavity collapse loads were prepared for the impact condition range of  $V_v = 80, 100, \text{ and } 120 \text{ FPS}$ ,  $V_H = 0, 15, 30, 45, \text{ and } 60 \text{ FPS}$ , and  $\theta_i = -10^\circ, -5^\circ, 0^\circ, 5^\circ, \text{ and } 10^\circ$ . After design definition of the SRB recovery system, the loads presentation was changed to vertical velocities of 80, 85, and 90 FPS. The 85 and 90 FPS data was derived through  $q$  interpolations of the correlated 80 and 100 FPS data. The new data presentation also incorporated additional horizontal velocities of 5 and 20 FPS. These were included as a result of a Monte Carlo statistical analysis that indicated that the SRB had a 90% probability of impacting the water with an impact angle between  $\pm 5^\circ$  and a horizontal velocity between 5 and 45 FPS with the mean value being 20 FPS.

The cavity collapse loads as prepared encompassed more than 100 impact conditions. As it would be impractical to analyze this quantity of



data from a structural design standpoint, it was decided to reduce the cavity collapse loads to a more simplified definition. This was based on the fact that the primary objective was to define a set of design capability loads with provisions to identify attrition rates due to perturbations of loads resulting from deviations from nominal impact conditions. The approach can then be to define a set of nominal loads with perturbation functions which allow the loads to be applied over the complete range of impact conditions.

The nominal loads were defined using data for  $V_v = 85$  FPS,  $0 \leq V_H \leq 45$  FPS, and  $-5^\circ \leq \theta_i \leq +5^\circ$ . Over this range of impact conditions (except for  $V_H = 0$ ,  $\theta = 0^\circ$ ) the wetted lengths and keel pressures are approximately the same and the lee side pressure distributions have the same shape with variations in magnitude. The nominal pressure distributions were defined as the numerical average of all pressure data. The peak lee side pressure was used with correlated data to define the impact parameter  $\alpha/2 - \theta_{cc}$  and this value defined CG accelerations.

The final data presentation consisted of load plots for two data cases,  $V_v = 85$  FPS,  $V_H = 0$ , and  $\theta_i = 0$ , and  $V_v = 85$  FPS nominal cavity collapse. Also presented were carpet plots of penetration depth and peak lee side pressure along with procedures for defining overall vehicle pressure and load distributions as a function of impact condition.

### 8.3 Maximum Penetration

Maximum penetration is attained when the farthest aft point along the vehicle centerline reaches its maximum depth. The event can be observed clearly in the underwater photographic records. These records were used

to measure penetration depth, pitch angle and velocity at the time of maximum penetration. Penetration depth and pitch angle were then plotted as a function of impact conditions (Figs. 8-8 and 8-9).

The vertical velocity of the vehicle is zero at the time of maximum penetration. There is some pitch rotation, but resultant velocities are negligibly small, so dynamic pressures can be neglected. Therefore, pressures acting on the vehicle are essentially defined by local hydrostatic values alone. That is -

$$P = \rho gh$$

where  $h$  = distance below the liquid free surface. With vehicle attitude (pitch angle,  $\theta$ ) and maximum penetration depth known as a function of impact conditions, definition of vehicle geometry then leads directly to the calculation of depth and corresponding hydrostatic pressure for all points on the vehicle. Cylinder body internal pressure was again assumed constant, at the minimum value dictated by case temperature as given in Fig. 8-10, and was regarded to be independent of impact conditions.

#### 8.4 Slapdown

Vehicle slapdown is defined as the phase of rapid angular rotation and lateral displacement from the near vertical to the horizontal flotation position. As this event occurs the forward portion of the vehicle is subjected to large oblique impact or slam pressures with the water pressure wave propagating radially around the cylindrical surface and longitudinally forward along the keel meridian. During slapdown the vehicle C.G. is at or approximately 1 diameter below the water surface and the body rotation is about a point near the base. The local crossflow velocities on the rear half of the vehicle are low and do not produce signi-

ficant hydrodynamic pressures. On the forward portion of the vehicle, crossflow velocities increase and substantial pressures are encountered. The peak pressure increases as the slapdown progresses, reaching maximum value when the pressure wave is approximately 2 diameters aft of the nose and then decreases as the wave moves to the nose.

Due to the time variation of pressure and acceleration forces during slapdown there is no obvious instant when the total vehicle structural loads are at a maximum. Therefore, in calculating slapdown loads, three or more time points were used so that the maximum load condition would be encompassed. These time points corresponded to the time of peak pressure at selected keel pressure transducer locations. At the selected time points model data was evaluated for use as inputs to the loads program.

During slapdown the vehicle is subjected to low frequency pitch accelerations as shown in figures 8-11 and 8-12. These were read from the three model accelerometers at the times of interest. The readings were then plotted and used to calculate the normal and angular accelerations at the dry vehicle C.G. These accelerations were then carpet plotted as a function of water entry condition for each time point. Smooth curves were faired through any irregularities and the data was extrapolated to cover impact conditions of interest where test data was not available.

The time history of slapdown pressure at a given body station appears as suddenly applied pressure decaying slowly to local hydrostatic pressure. As shown in Figure 8-13, the peak pressure is over a very short time duration which should contribute very little to the vehicle structural response other than some finite localized panel loads. The total vehicle external pressure load distribution was therefore treated as being com-

prised of a low frequency base load (assumed to be static at any given time slice) with the shorter pulse spray root pressure superimposed on top of it. The spray root pulse load was treated as a localized single degree of freedom system and the equivalent static pressure load for the spray root pressure spike is approximately  $1/3$  of the high frequency pulse peak. It should be stated that only the high frequency pressure spike, over and above the low frequency load pulse was actually reduced to an equivalent static value. All other pressures were read at a given instant in time and assumed as static. For expediency of hand reading data plots, the ten millisecond averaging routine was utilized as the best approximation of the equivalent maximum static values. More recently a complete set of differential equations have been incorporated into the data analysis system to define exactly the equivalent static response of a single degree of freedom system. These results agree quite well with ten millisecond average values, based upon the full scale vehicles response natural frequencies.

Keel pressure distributions for the forward portion of the body were read from model test data at the selected time points during slapdown. These data were plotted as a function of water entry condition for each transducer location and time point. The data was then smoothed and extrapolated to cover entry conditions where test data was not available. On the rear portion where pressures are hydrostatic the values were calculated for expediency rather than reading model data. These calculations were based on wetted length determined from transducer data, and the model pitch angle read from photographic data.

Radial pressure distributions were developed from correlations of previous model test data. These data were used to define radial distribution

relationships as a function of longitudinal station normalized by keel pressure. Definition of these distributions are presented in Figures 8-14 through 8-17.

There is a significant amount of internal water, on the order of 100,000 pounds full scale, in the vehicle during slapdown which effectively alters the SRB mass characteristics. The quantity and location of the water could not be determined from available test data so estimates were used.

It was assumed that the nozzle and skirt would be completely full and that inside of the case the water would be approximately at the nozzle throat with the surface parallel to the outside free water surface. Figure 8-18 shows the estimated injected water locations. In the loads program this water is accounted for by adding it to the dry SRB mass distribution.

The correlated pressure and acceleration data were then Froude scaled to full scale values and input to a computer program for calculation of slapdown loads. This program considers the SRB to be a rigid body with pressure and inertial forces concentrated at discrete points located 20 inches on center. Only forces normal to vehicle centerline are considered in the loads program.

Inputs to the slapdown loads program are:

- a. SRB mass distribution as a function of vehicle station.
- b. Onboard water as a function of vehicle station.
- c. Lee and keel side wetted lengths.
- d. Keel side longitudinal pressure distribution.

- e. Normal and angular accelerations at the vehicle C.G.
- f. Vehicle pitch angle.
- g. Pressure integration factors as a function of wetted length and keel pressure.

The program calculates the vehicle C.G. and pitch moment of inertia, and the local pressure and inertial shear forces at each 20 inch body section. The local shears are then integrated longitudinally to determine the net lateral load and the centroid of application for the pressure and inertial loads. The net loads are then compared and all input pressures are ratioed so that the net pressure load is equal to the net inertial load, and the vehicle angular acceleration is adjusted so that the centroids of the two shear diagrams match. The adjusted pressure and inertial shears are then combined and total vehicle shear and bending moment diagrams are calculated.

If the pressure and inertial forces balanced within 3% the input data was considered satisfactory. If the load balance was not satisfactory, the input data was reviewed and individual pressures and/or accelerations were adjusted, generally less than 10%, and a new set of vehicle loads were calculated.

The output from the slapdown loads program are presented as plots of keel pressure distribution, applied pressure load, applied inertial load, the total vehicle shear diagram, and the total vehicle bending moment diagram. Figures 8-19 through 8-22 show typical results from the loads program.

The initial slapdown loads documentation was prepared for impact conditions of  $V_V = 80, 100, \text{ and } 120 \text{ FPS}$ ,  $V_H = 0, 15, 30, 45, \text{ and } 60 \text{ FPS}$ , and  $\theta_1 = -10^\circ, -5^\circ, \text{ and } 0^\circ$ . Loads were presented at four time points during slapdown for

each impact condition. These data were later interpolated to provide data for vertical velocities of 85, and 90 FPS. As previously discussed in the Cavity Collapse section, it was not practical to structurally analyze the large quantity of slapdown data and a set of nominal loads was defined for a vertical impact velocity of 85 FPS. The pressure and accelerations used to calculate the nominal loads were the numerical average of data for  $V_v = 85$  FPS,  $V_h = 20$  and 45 FPS, and  $\theta_i = 0^\circ$  and  $-5^\circ$ .

Loads were calculated at four time points which corresponded with the initial keel wetting at vehicle stations 1009, 769, 569, and 409. Four plots are presented for each time point, applied keel pressure, applied pressure and inertial loads, vehicle shear and vehicle bending moment. Also presented are carpet plots of peak keel pressure as a function of impact condition and procedures for defining pressure and load distributions for impact conditions of interest.

#### 8.5 Component Loads

In addition to overall SRB loads, component level acceleration and pressure loads were developed for selected SRB structures. The components considered were:

1. Nose Cone frustum
2. Systems tunnel
3. E.T. Attach Ring
4. Aft separation motor
5. TVC package
6. Nozzle actuator
7. Heat Shield/Aft End Ring
8. SRM Clevis Joint Pin Retainer Band

Component acceleration loads were derived from model accelerometer data. These data were reviewed for peak axial and pitch accelerations over the complete range of water impact conditions. The data was presented as peak axial and lateral acceleration for three vehicle zones; the fwd. skirt, the SRM case, and the aft skirt. Component acceleration loads are shown in Figure 8-23.

Due to time, model scale, and instrumentation limitations, it was not feasible to simulate model hardware for direct measurement of component pressure loads. Therefore, these loads were generated using empirical methods as discussed in the following paragraphs.

#### 8.5.1 Nose Cone Frustum Loads

The SRB nose cone is to be recovered using the drogue chute of the main SRB recovery system to decelerate the nose frustum prior to water impact. The nose cone is expected to impact the sea with vertical velocities between 40 and 60 ft/sec, horizontal drift velocities from 0 to 45 ft/sec, and pitch angles up to 20°.

Water impact loads on the SRB Nose Cone Frustum were generated using empirically derived water impact pressure coefficients and a two degree of freedom trajectory program. The water impact pressure coefficients were obtained from model test pressures for the SRB nozzle and aft skirt, nondimensionalized by the dynamic pressure, and correlated with the local angle of attack. Internal and external pressures were correlated independently and the results are shown in Figure 8-24.

The two degree of freedom trajectory program allowed the Nose Cone Frustum to decelerate along its velocity vector but was constrained from rotating, i.e. its pitch attitude was fixed. Water impact pressures



were computed for the wetted portion of the vehicle from the above pressure coefficients and the pressures integrated to obtain the applied forces and decelerations. The wetted portion of the vehicle was taken as that portion of the vehicle below the free water surface.

Cavitation over external surfaces was accounted for by applying zero pressure coefficients (pressure equals zero psig) when the keel meridian angle of attack,  $\alpha_{\text{keel}}$ , was negative. Cavitation on the external lee side, when the keel meridian is at a positive angle of attack, was accounted for by applying a pressure distribution such that the pressure at and beyond the 90° meridian was zero psig. Internal cavitation was accounted for by using a pressure distribution such that the pressure on the internal keel meridian was zero (psig) when the keel meridian angle of attack was positive. Figure 8-25 illustrates the pressure distributions used in the analysis.

The nose cone frustum trajectory was calculated for 0.2 sec by which time all forces had reached maximum values and were decaying. The results

Table 8-1. Nomenclature for the listing is presented below:

#### NOSE CONE FRUSTUM TRAJECTORY NOMENCLATURE

AN	Normal acceleration, g's
AX	Axial acceleration, g's
B	Penetration depth, in.
LW1, LW2, LW3	Wetted lengths along longitudinal axis on keel, centerline, and lee meridians, inches forward of Station 395.
P1	Pressure acting on external side of bottom ring, psig.
P2	Pressure acting on internal keel meridian of Nose Cone Frustum, psig.
P3	Pressure acting on external keel meridian of Nose Cone Frustum, psig.

P4	Pressure acting on internal lee meridian of Nose Cone Frustum
T	Time from impact, seconds.
THDD	Pitch angular acceleration, radian/sec <sup>2</sup>
THETA	Pitch angle at impact, degrees
VH	Horizontal velocity at impact, fps
VV	Vertical velocity at impact, fps

#### 8.5.2 Systems Tunnel Loads

During water impact the systems tunnel, which runs the full length of the SRM case, will be subject to the same loads as the case. The peak normal pressure load will occur during cavity collapse with the tunnel on the lee side of the vehicle. The peak lateral load should occur during slapdown with the tunnel near but not on the keel so that a ventilated cavity is formed on one side of the tunnel with the other side subjected to keel slapdown pressure. Figure 8-26 illustrates the systems tunnel pressure distributions.

#### 8.5.3 E. T. Attach Ring Loads

The E. T. attach ring, located at SRB Station 1511, will be subjected to cavity collapse loads followed by hydrostatic pressures through maximum penetration, rebound, and slapdown. During cavity collapse, the ring will be first subjected to axial pressures as the cavity collapse wave propagates forward and then to radial pressures as the wave passes over the ring. The axial pressures were driven from maximum values read from lee and keel pressure transducers located immediately aft of the E. T. ring during test TMS-333. The lateral loads are assumed to be equal to cavity collapse pressure distributions at Sta. 1511. Figure 8-27 illustrates the E. T. ring pressure loads.

#### 8.5.4 Aft Separation Motor Loads

The SRB has four aft separation motors mounted on the outside of the aft skirt approximately at the midpoint of the skirt. Each motor is approximately 1 foot in diameter and three feet long. During initial impact, the motors will be in the ventilated cavity created by the skirt and will not be subjected to pressure loads until wall slap or the onset of cavity collapse.

With the motors on the keel side, they will first be subjected to either an axial load for pure vertical entry, or an axial and lateral load for a combined horizontal and vertical velocity entry. These load conditions will be followed by a stagnation loading as the cavity collapses. If the motors are on the lee side of the vehicle they only receive the stagnation load condition.

In the absence of test data, the initial axial and lateral pressures were calculated using a flat plate pressure coefficient of 2.0 and the vehicle velocity at cavity collapse. Correlations of photographic and accelerometer trajectory data show that velocities at cavity collapse are approximately 60% of initial impact velocities. The pressures  $P_1$  and  $P_2$  (Figure 8-28) were calculated by:

$$V_{\text{Cavity Collapse}} = (0.6) (V_{\text{Initial Impact}})$$

$$P = 2 \rho V_{cc}^2 / 2$$

Pressure  $P_1$  considers only vertical velocity and Pressure  $P_2$  considers vertical and horizontal velocities. Pressure  $P_3$  is the maximum skirt cavity collapse pressure.

#### 8.5.5 TVC Package Loads

Two TVC packages are located inside of the aft skirt. They consist of a number of cylindrical and spherical shapes attached to an open rectangular

I-beam framework that is approximately 3 ft. x 4 ft. Due to the small scale model SRB, it was not feasible to simulate this hardware in the test program. Also, because of the complex geometry of these packages and their location within the skirt, the flow is not amenable to rigorous analysis.

A simple analysis, however, was performed and the resulting estimates should be adequate for providing an overall design load. Pressure  $P_1$  was calculated as  $q$  and pressure  $P_2$  was calculated as  $2 \times q$ . The estimated pressure distributions and magnitudes are given in Figure 8-29. The maximum axial load is  $P_1$  as is the maximum lateral load which can exist in any direction normal to the SRB centerline. The stagnation loading condition is  $P_2$  applied uniformly around the component.

The maximum TVC package TVC package axial load occurs at the same time as the vehicle maximum positive axial acceleration event. The maximum lateral load can occur anytime from shortly after the vehicle maximum positive axial acceleration event to just prior to the maximum nozzle negative axial load event. For analysis purposes, assume that the TVC lateral load can occur in combination with either of the aforementioned vehicle loading events. The maximum TVC stagnation load occurs at the same time as the maximum nozzle negative axial load event.

#### 8.5.6 Nozzle Actuator Loads

Each SRB has two actuators located within the aft skirt. The actuator loading is generated from two sources, the first being the actuator axial load transmitted between the nozzle and skirt. This load was presented with initial impact data. The second source of load is caused by the water impacting the actuator. The actuator was not simulated in the test program

because of the restrictively small model size. Therefore, a simple analysis was performed, the results of which are given in Figure 8-30. The lateral pressure loading is  $P_1$  whereas the axial is  $P_2$ . The stagnation loading condition is  $P_3$  applied uniformly around the actuator. Actuator impingement pressures  $P_1$  and  $P_2$  were calculated from the following equation:

$$P = C_{DC} q \sin \delta$$

$$\cos \delta = \cos (\theta_i + \tan^{-1} V_h/V_v) \cos (\epsilon + \beta)$$

where:

$$C_{DC} = \text{Cross Flow Drag Coefficient} = 1.2 \text{ for } P_1 \text{ and } 1.5 \text{ for } P_2$$

$$\delta = \text{Flow impingement angle} = 36^\circ \text{ for } P_1 \text{ and } 18^\circ \text{ for } P_2$$

$$\epsilon = \text{Skirt cone half angle} = 18^\circ$$

$$\beta = \text{Incidence angle of nozzle actuator} = 18^\circ$$

$$q = \text{Dynamic pressure} = \frac{1}{2} \rho v^2$$

Stagnation pressure  $P_3$  was calculated as  $2 \times q$ .

Actuator maximum axial, maximum lateral, and maximum stagnation pressure loads occur in the same time sequence as the corresponding TVC pressure loads defined above.

During the initial impact dynamic sequence, the SRM nozzle is exposed to large applied and inertial reaction loads. Resultant nozzle motion within snubber limits then produce large actuator response loads. These loads have been analyzed for the specific impact conditions presented in Table 8-2 defining three possible levels of damage to the actuator system.

The actuator fluid by-pass valve will open under an approximate 120 KIP load allowing the actuator to respond with a constant load. This value was used

as input to the nozzle system response analysis. Under some conditions load relief provided by the fluid by-pass valve is insufficient to keep up with the applied load, resulting in an increase in the actuator response load to values far exceeding the 120 KIP by-pass limit.

Table 8-2 presents peak actuator response loads for the various impact conditions analyzed. The three values presented for each condition are maximum values and correspond to the three dynamic loading events of initial impact: 1) maximum nozzle positive applied load; 2) nozzle maximum negative applied load; and, 3) nozzle inertial response after decay of the nozzle external applied pressure load.

To define the total actuator load external applied pressure loads defined above must be combined with the actuator response loads due to nozzle motion at the respective dynamic loading events, that is, use  $P_1$  and  $P_2$  for event (1), and  $P_3$  for events (2) and (3). Use linear interpolation for pressures at intermediate angles not analytically defined on Figure 8-30.

#### 8.5.7 Heat Shield/Aft End Ring Loads

The heat shield concept analyzed is shown in Figure 8-31. The heat shield is relatively lightweight flexible curtain type structure which will fail under the water impact loading environment. Before failing, however, the heatshield will be loaded up to its capability (approximately 10 psig) which, in turn, will load up the aft skirt end ring. The maximum end ring water impact pressure is an order of magnitude greater than the current heat shield capability. Figure 8-31 illustrates the heat shield in the pre water impact configuration. Upon water impact, the heat shield moves up to the position shown by the dashed line as it is being loaded up. It takes

approximately 10 m sec for the heat shield to reach this state from its pre impact configuration. Shortly thereafter, the shield will fail as the load increases to its maximum value. On the other hand, the aft skirt end ring pressure builds up to a peak pressure of 85 to 125 psig in approximately 3 to 5 m sec. Therefore, the aft end ring can be loaded up to its maximum value before the heat shield will fail. Hence, for strength analysis purposes, the capability of the heat shield should be combined with the peak water impact aft ring pressure.

#### 8.5.8 SRM Clevis Joint Pin Retainer Band Loads

SRM clevis joint pin retainer band shear loads have been estimated and are presented herein. The slapdown dynamic loading event, which occurs during water entry, subjects the pin retainer band to the worst case of shear loading. The shear loading is caused by skin friction drag. Water entry trajectories obtained from model tests were combined with drag data to estimate the shear loading. Using a conservative approach, the maximum shear loading is estimated to be 0.5 psig. The reentry aerodynamic shear loading is an order of magnitude less.

TABLE 8-1 NOSE CONE FRUSTUM TRAJECTORY LISTING

VV = 90., VM = 45., THETA = 20.,

T	B	AX	AN	TH00	LW1	LW2	LW3	P1	P2	P3	P4
.001	1.600	3.558	.170	33.653	.000	.000	.571	58.639	.000	.000	46.618
.002	1.199	3.111	.304	74.549	.000	.000	1.141	58.442	.000	.000	46.491
.003	1.797	6.357	.972	96.999	.000	.000	1.710	58.157	.000	.000	46.297
.004	2.393	7.389	1.362	111.295	.000	.000	2.277	57.799	.000	.000	46.045
.005	2.987	8.372	1.990	130.967	.000	.000	2.842	57.380	.000	.000	45.746
.006	3.577	9.193	2.413	142.476	.000	.000	3.404	56.900	.000	.000	45.393
.007	4.165	10.037	3.139	160.534	.000	.000	3.964	56.373	.000	.000	45.000
.008	4.750	10.751	3.663	175.479	.000	.000	4.521	55.793	.000	.000	44.557
.009	5.332	11.466	4.358	186.755	.000	.000	5.074	55.170	.000	.000	44.074
.010	5.910	12.114	4.999	201.096	.000	.000	5.624	54.503	.000	.000	43.549
.011	6.484	12.704	5.598	209.923	.000	.000	6.171	53.798	.000	.000	42.984
.012	7.055	13.279	6.277	223.125	.000	.000	6.714	53.057	.000	.000	42.385
.013	7.621	13.771	6.814	230.124	.000	.000	7.253	52.283	.000	.000	41.749
.014	8.184	14.275	7.500	242.005	.000	.000	7.788	51.482	.000	.000	41.086
.015	8.743	14.682	7.986	247.385	.000	.000	8.320	50.652	.000	.000	40.390
.016	9.297	15.116	8.647	257.844	.000	.000	8.847	49.802	.000	.000	39.673
.017	9.847	15.445	9.077	261.737	.000	.000	9.371	48.928	.000	.000	38.929
.018	10.392	15.809	9.696	270.696	.000	.000	9.890	48.040	.000	.000	38.161
.019	10.933	16.065	10.064	273.164	.000	.000	10.403	47.135	.000	.000	37.365
.020	11.470	16.361	10.629	280.603	.000	.000	10.915	46.221	.000	.000	36.557
.021	12.002	16.551	10.936	281.792	.000	.000	11.422	45.296	.000	.000	35.732
.022	12.530	16.793	11.437	287.750	.000	.000	11.924	44.367	.000	.000	34.901
.023	13.053	16.912	11.686	287.790	.000	.000	12.422	43.431	.000	.000	34.057
.024	13.571	17.082	12.115	292.309	.000	.000	12.915	42.496	.000	.000	33.213
.025	14.085	17.157	12.308	291.306	.000	.000	13.404	41.560	.000	.000	32.362
.026	14.594	17.269	12.663	294.482	.000	.000	13.888	40.629	.000	.000	31.514
.027	15.099	17.295	12.804	292.579	.000	.000	14.369	39.700	.000	.000	30.664
.028	15.599	17.353	13.083	294.491	.000	.000	14.845	38.790	.000	.000	29.822
.029	16.095	17.337	13.176	291.826	.000	.000	15.316	37.866	.000	.000	28.982
.030	16.585	17.345	13.378	292.572	.000	.000	15.783	36.964	.000	.000	28.153
.031	17.072	17.288	13.432	289.240	.000	.000	16.246	36.058	.000	.000	27.330
.032	17.554	17.244	13.556	288.857	.000	.000	16.705	35.162	.000	.000	26.520
.033	18.031	17.157	13.579	285.044	.000	.000	17.159	34.279	.000	.000	25.721
.034	18.504	17.069	13.621	283.653	.000	.000	17.609	33.413	.000	.000	24.936
.035	18.973	16.961	13.626	279.544	.000	.000	18.055	32.561	.000	.000	24.165
.036	19.437	16.815	13.534	274.672	.000	.000	18.497	31.727	.000	.000	23.410
.037	19.897	16.711	13.585	272.979	.000	.000	18.934	30.911	.000	.000	22.673
.038	20.352	16.549	13.475	267.811	.000	.000	19.368	30.112	.052	.000	21.950
.039	20.803	16.420	13.474	265.072	.000	.000	19.797	29.331	.277	.000	21.245
.040	21.250	16.251	13.362	259.530	.000	.000	20.223	28.568	.497	.000	20.556
.041	21.693	16.094	13.296	256.122	.000	.000	20.644	27.824	.710	.000	19.886
.042	22.132	15.920	13.186	250.615	.000	.000	21.062	27.097	.917	.000	19.232
.043	22.567	15.725	13.014	244.739	.000	.000	21.476	26.390	1.116	.000	18.596
.044	22.998	15.565	12.955	241.241	.000	.000	21.886	25.702	1.308	.000	17.980
.045	23.425	15.366	12.782	235.430	.000	.000	22.292	25.032	1.493	.000	17.379
.046	23.847	15.197	12.671	231.493	.000	.000	22.694	24.380	1.671	.000	16.797
.047	24.267	14.990	12.507	225.842	.000	.000	23.093	23.746	1.843	.000	16.232
.048	24.682	14.780	12.301	220.011	.000	.000	23.488	23.130	2.007	.000	15.684
.049	25.093	14.603	12.195	216.100	.000	.134	23.880	22.533	2.163	.000	15.154
.050	25.501	14.396	11.996	210.444	.000	.568	24.268	21.953	2.314	.000	14.640
.051	25.905	14.205	11.844	206.237	.000	.998	24.652	21.389	2.457	.000	14.143
.052	26.305	14.005	11.663	200.838	.000	1.424	25.033	20.843	2.595	.000	13.662
.053	26.702	13.796	11.448	195.332	.000	1.846	25.411	20.313	2.726	.000	13.197
.054	27.096	13.612	11.305	191.260	.000	2.265	25.785	19.799	2.849	.000	12.748



TABLE 8-2 SRM NOZZLE ACTUATOR RESPONSE LOADS

IMPACT CONDITION			ACTUATOR E x 10 <sup>-3</sup> LBS.			ACTUATOR F x 10 <sup>-3</sup> LBS.			
V <sub>H</sub>	θ <sub>i</sub>	φ	NOZZLE AXIAL LOADING EVENT			NOZZLE AXIAL LOADING EVENT			
			MAX. POS	MAX. NEG.	REBOUND	MAX. POS	MAX. NEG.	REBOUND	
5	-5	+45	- 60	- 120	+120	- 120	+120	- 70	
20	↓	↓	- 120	+120	- 80	-120	- 120	+120	
45	↓	↓	- 170	- 120	+120	-210	-120	+120	
5	0		+ 40	- 120	+120	+ 50	- 120	+120	
20	↓		- 50	- 120	+120	- 50	- 120	+120	
45	↓		-120	- 120	+120	-120	- 120	+120	
5	+5		+ 60	-130	+130	+ 60	- 120	+140	
20	↓		+ 40	+120	-120	- 90	+120	+ 120	
45	↓	↓	-120	+120	-120	-120	+120	- 120	
0*	-5	+ 90	+ 80	- 120	+ 120	- 60	- 120	+140	
5	↓	↓	+ 60	- 120	+120	-120	- 120	+140	
20			- 120	+120	- 70	-120	- 120	+140	
35	↓	↓	+ 50	-130	+110	-195	+160	- 80	
45	↓		- 90	-110	- 60	-320	-380	+200	
0*	0		+100	- 120	+120	+100	- 120	+ 120	
5	↓	↓	- 120	+120	- 60	- 120	+120	- 80	
20		↓	- 120	+120	- 60	- 120	- 120	+ 120	
45	↓	↓	-110	+120	- 60	-210	- 120	+135	

TABLE 8-2 SRM NOZZLE ACTUATOR RESPONSE LOADS (Continued)

IMPACT CONDITION			ACTUATOR E x 10 <sup>-3</sup> LBS.			ACTUATOR F x 10 <sup>-3</sup> LBS.			"
V <sub>H</sub>	θ <sub>i</sub>	φ	NOZZLE AXIAL LOADING EVENT			NOZZLE AXIAL LOADING EVENT			
			MAX. POS.	MAX. NEG.	REBOUND	MAX. POS.	MAX. NEG.	REBOUND	
5	+5	+90	- 45	-120	+120	+ 70	-120	+120	
20	↓	↓	-60	-120	+140	-30	+120	-120	
45	↓	↓	- 70	-120	+120	-120	+160	-130	
5	-5	+135	+120	+120	-120	- 80	-120	+120	
20	↓	↓	+120	+ 60	-120	-120	-120	+120	
45	↓		+225	+120	-120	-225	-120	+120	
5	0		+110	-120	+120	+ 20	-120	+120	
20	↓		+120	-120	+120	- 80	-120	+120	
45	↓		+150	+120	-120	-150	-120	+120	
5	+5		- 50	-120	+120	+ 70	-125	+120	
20	↓		+ 60	-204	+120	- 20	+120	-120	
30	↓		+120	-270	+120	- 90	+110	-120	
45	↓	↓	+120	-270	+120	-120	+120	-120	
5	-5	+180	+120	-110	-120	+80	-120	+120	
20	↓	↓	+140	-130	- 50	+ 60	-120	+120	
25	↓		+210	-120	- 60	+ 60	-120	+120	
45	↓		+370	+530	-180	-20	+120	-120	
5	0	↓	+120	-120	+120	+80	-120	+120	

TABLE 8-2 SRM NOZZLE ACTUATOR RESPONSE LOADS (Continued)

IMPACT CONDITION			ACTUATOR E x 10 <sup>-3</sup> LBS.			ACTUATOR F x 10 <sup>-3</sup> LBS.			
V <sub>H</sub>	θ <sub>i</sub>	φ	NOZZLE AXIAL LOADING EVENT			NOZZLE AXIAL LOADING EVENT			
			MAX. POS.	MAX. NEG.	REBOUND	MAX. POS.	MAX. NEG.	REBOUND	
20	0	+180	+120	-100	-120	+70	-120	+120	
45	↓		+270	+180	-120	+30	-120	+120	
5	+5		- 15	-125	+120	-70	-120	+120	
20	↓		+ 90	-225	+120	+ 25	-120	+120	
40	↓		- 30	-285	+120	+ 30	-120	+120	
45	↓	↓	+120	-255	+120	+20	- 90	+110	
5	-5	+225	+115	-115	-100	+120	-120	+115	
20	↓	↓	+120	-120	- 70	+120	-120	- 50	
30	↓		+120	-120	- 50	+120	-120	- 60	
45	↓		+225	+120	-120	+230	+120	-120	
5	0		+110	-120	+120	+120	-120	+120	
20	↓		+120	-110	- 90	+120	-120	-120	
45	↓		+150	+120	-120	+150	+120	-120	
5	+5		+ 20	-120	+120	- 80	-120	+120	
20	↓		+ 60	-160	+120	+ 60	-140	+120	
45	↓	↓	+110	-160	+120	+110	-160	+120	

\* VALUES FOR V<sub>H</sub> = 0 MAY BE USED FOR ALL  $\phi$  ANGLES.

NOTE: PLUS INDICATES ACTUATOR COMPRESSION

MINUS INDICATES ACTUATOR TENSION

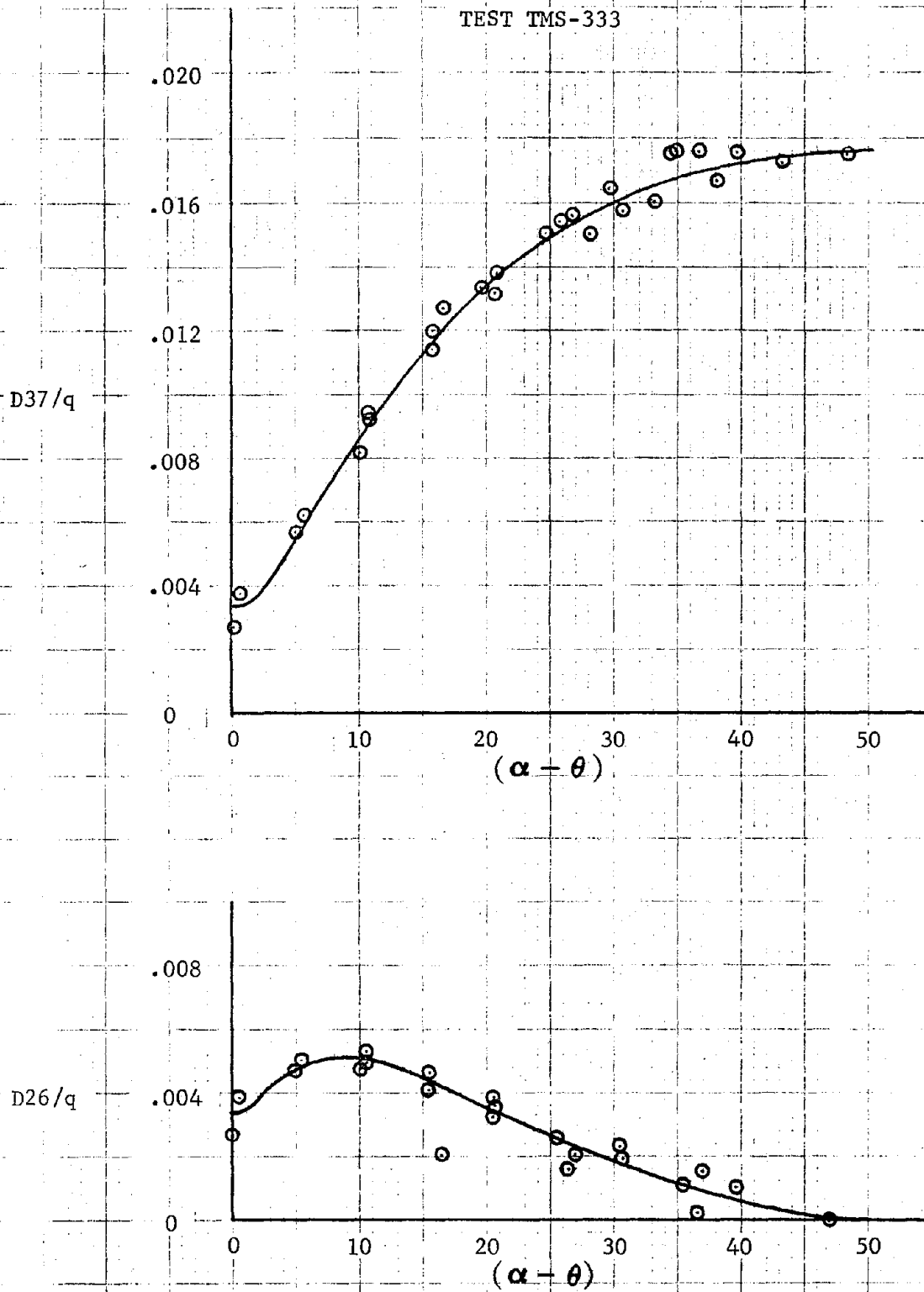


FIGURE 8-1. CORRELATION OF INTERNAL SKIRT PRESSURES,  
MAXIMUM PITCH ACCELERATION EVENT

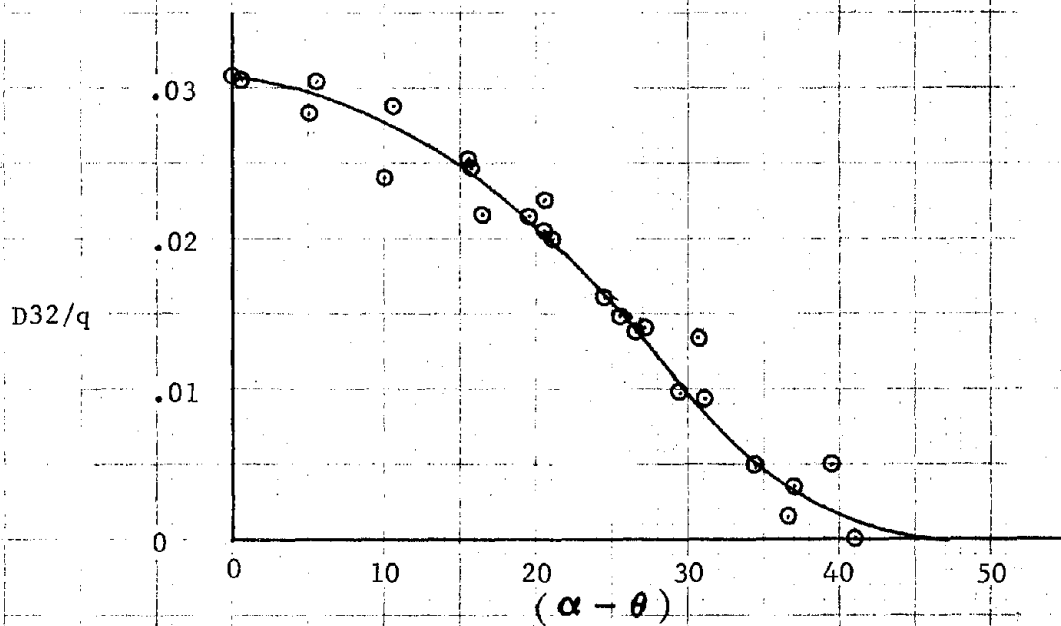
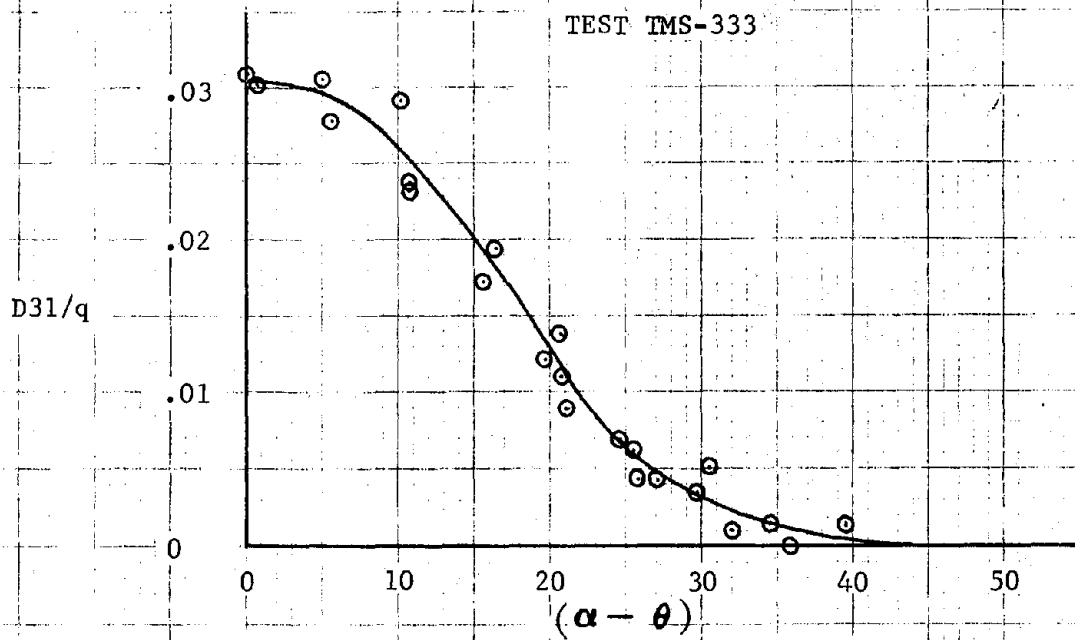
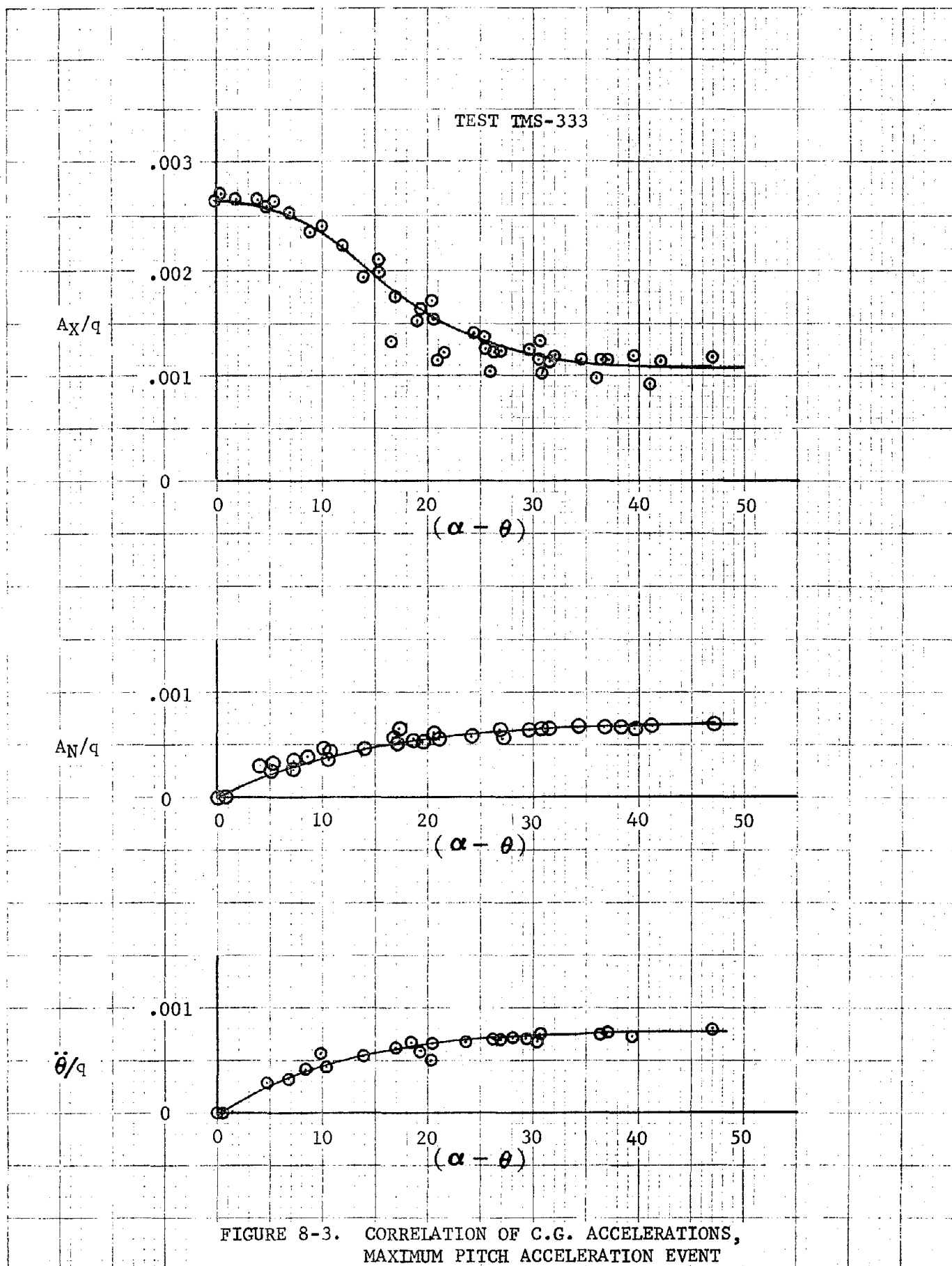


FIGURE 8-2. CORRELATION OF BULKHEAD PRESSURES,  
MAXIMUM AXIAL ACCELERATION EVENT



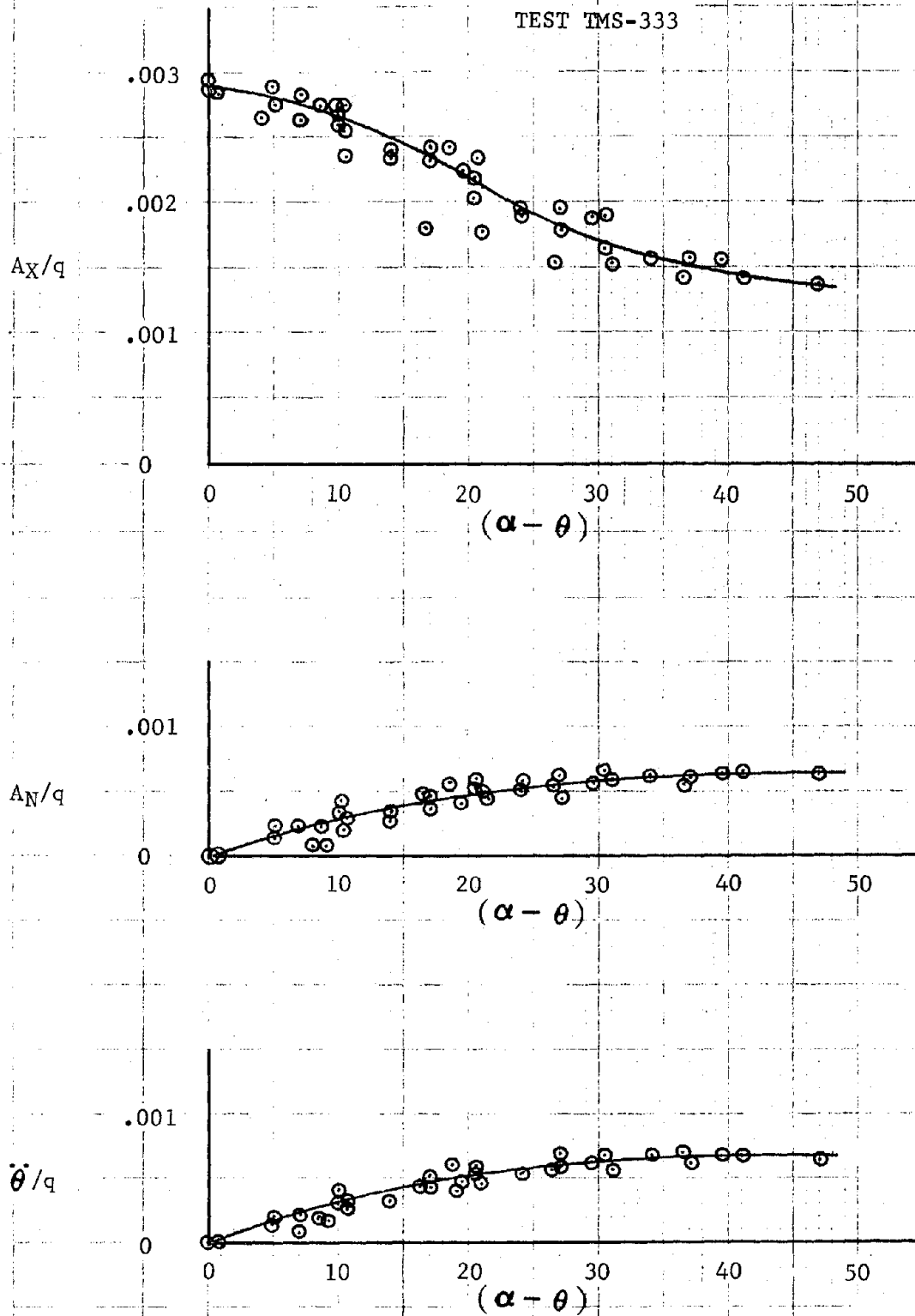


FIGURE 8-4. CORRELATION OF C.G. ACCELERATIONS,  
MAXIMUM AXIAL ACCELERATION EVENT

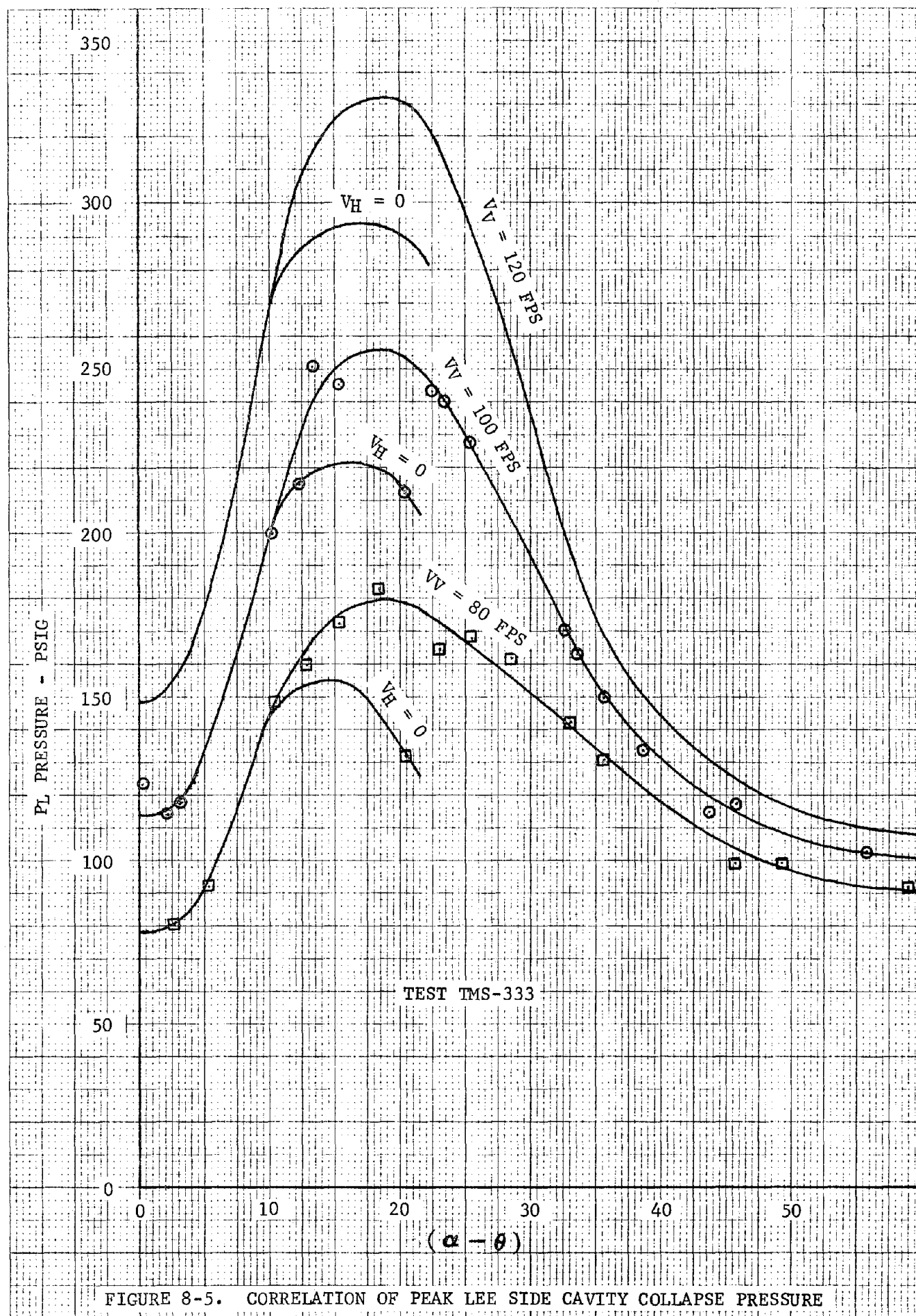


FIGURE 8-5. CORRELATION OF PEAK LEE SIDE CAVITY COLLAPSE PRESSURE



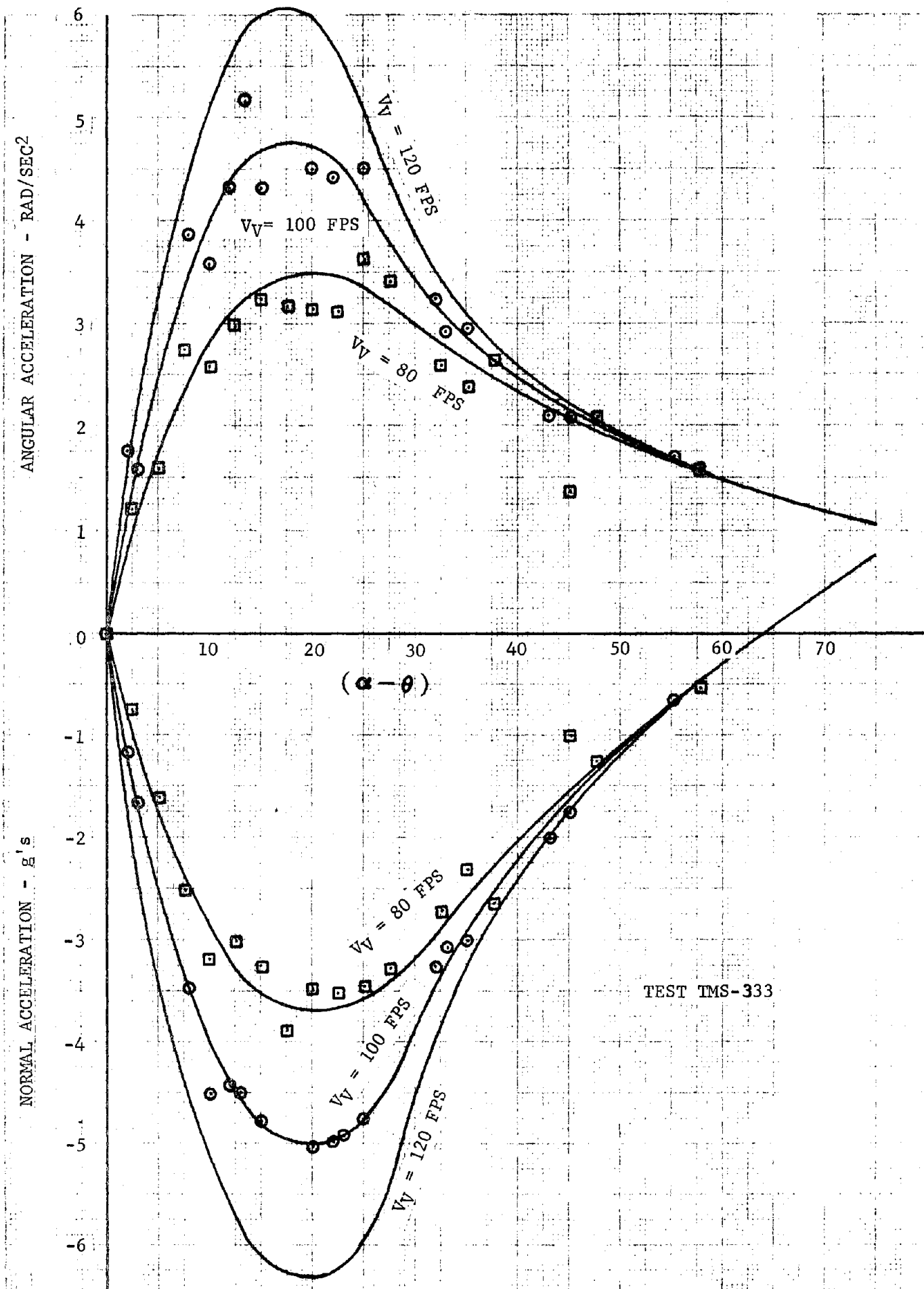
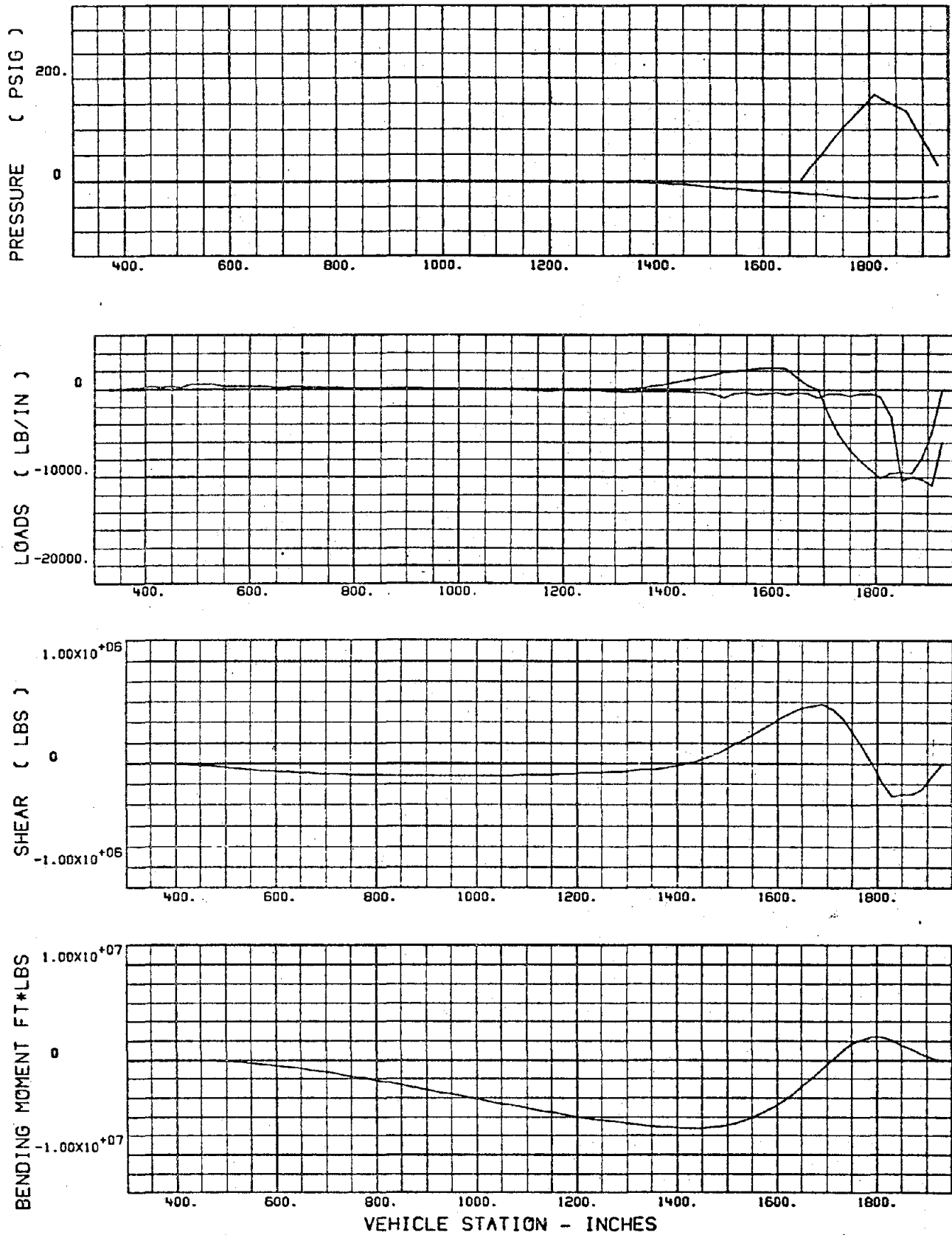


FIGURE 8-6. CORRELATION OF C.G. ACCELERATIONS AT CAVITY COLLAPSE

FIGURE 8-7

NOMINAL SRB WATER IMPACT CAVITY COLLAPSE LOADS  
 5/1/75 FULL SCALE CONFIGURATION  
 IMPACT CONDITIONS  $VV = 85$   $0 \leq VH \leq 60$   $-10 \leq TH \leq 10$   
 $\Phi = 0$  AND  $180$  DEG PRESSURE DISTRIBUTIONS



11/1/74 CONFIGURATION

$V_V = 80 \text{ FPS}$

$V_V = 100 \text{ FPS}$

$V_V = 120 \text{ FPS}$

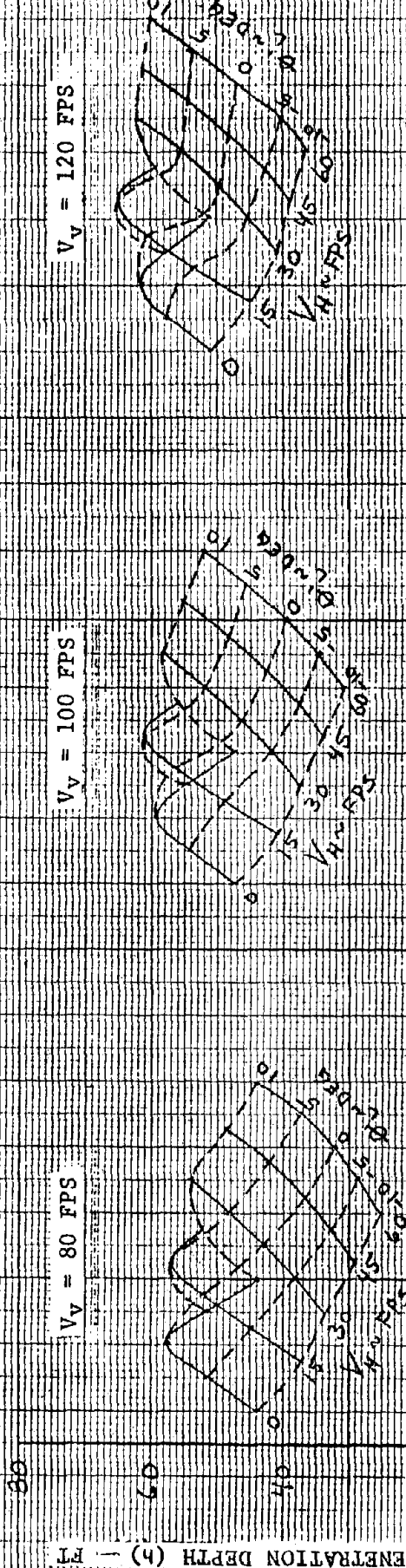


FIGURE 8-8 MAXIMUM PENETRATION DEPTH

11/1/74 CONFIGURATION

$V_V = 80 \text{ FPS}$

$V_V = 100 \text{ FPS}$

$V_V = 120 \text{ FPS}$

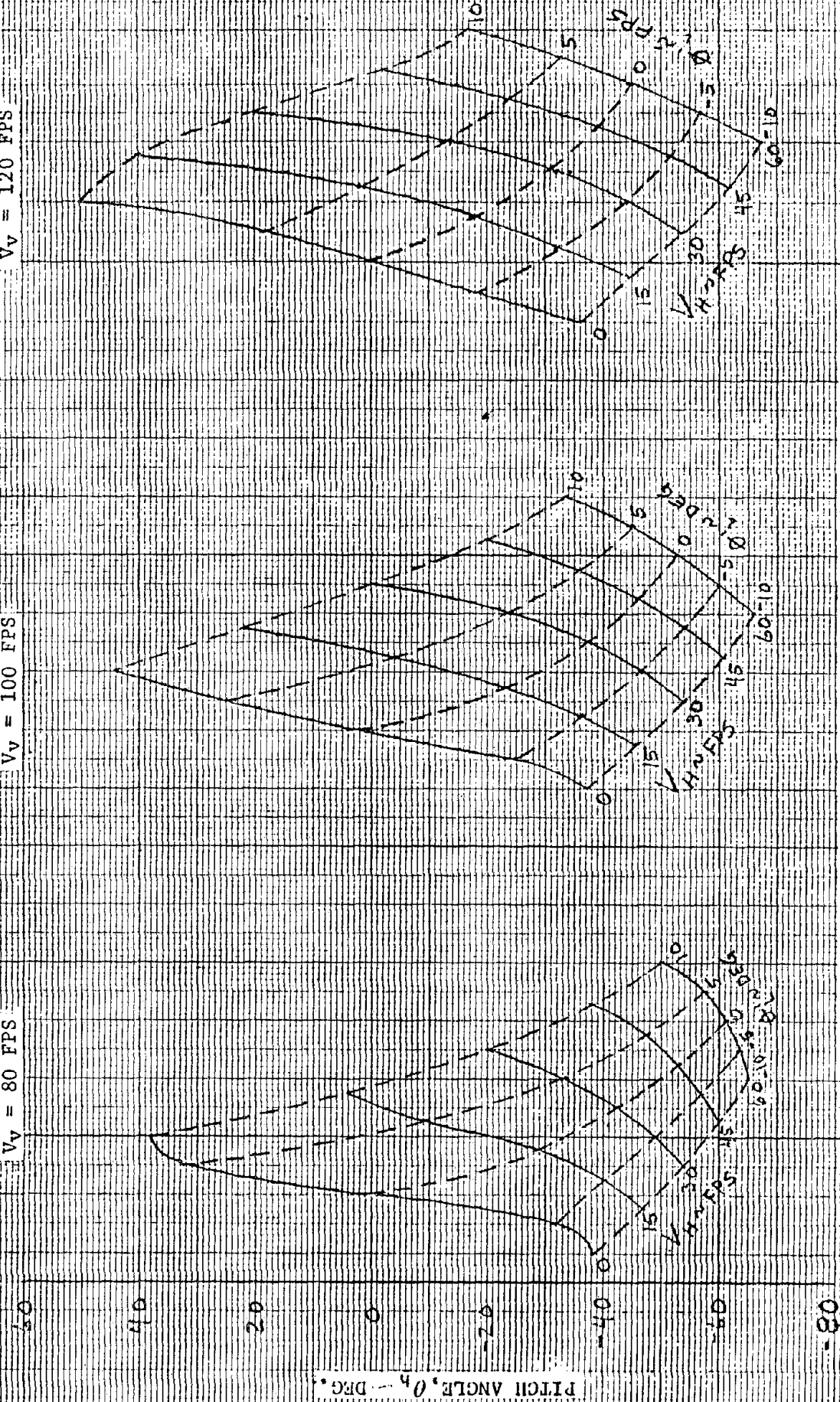


FIGURE 8-9 PITCH ANGLE AT MAXIMUM PENETRATION DEPTH

11/1/74 CONFIGURATION

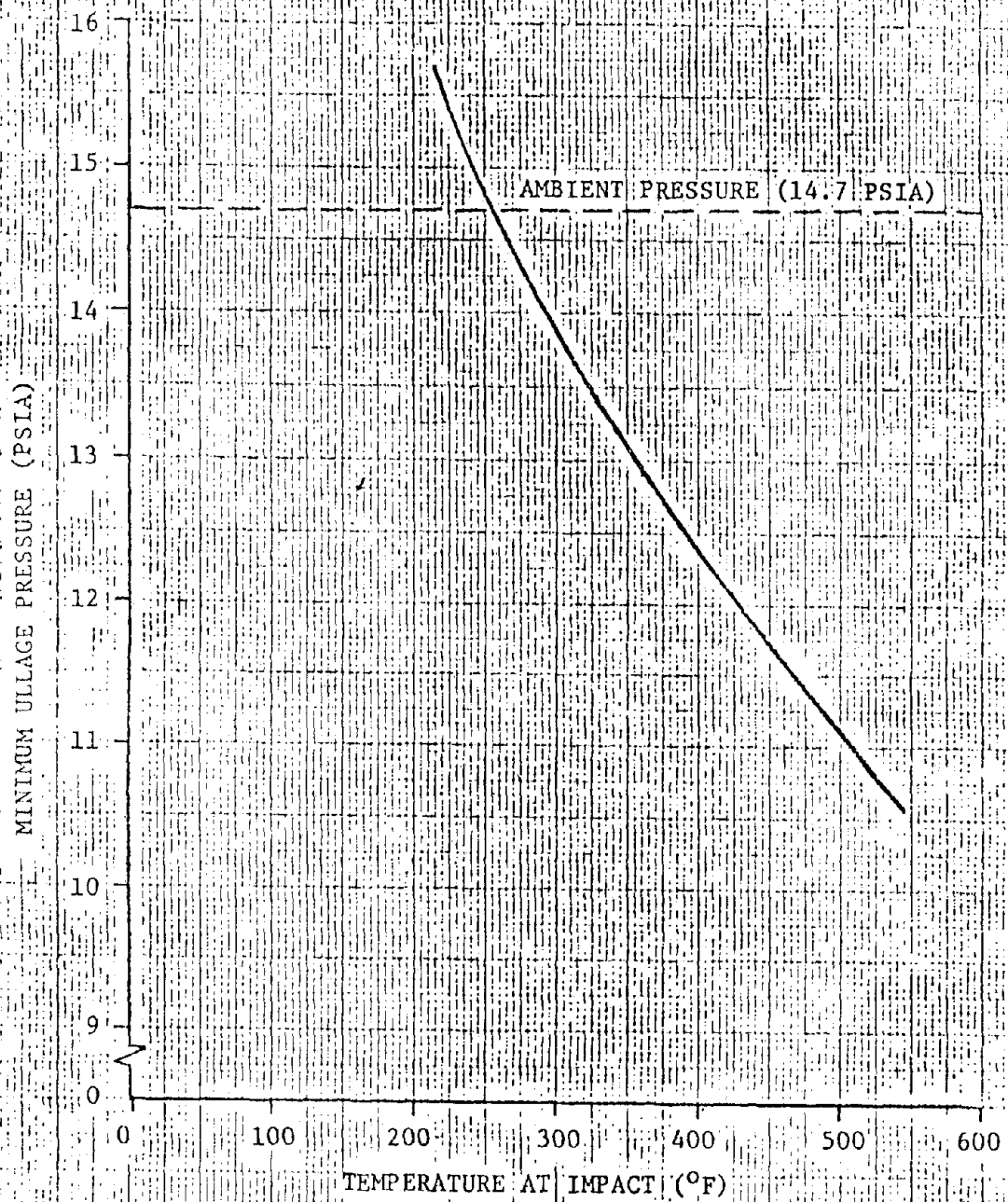


FIGURE 8-10 MINIMUM EXPECTED ULLAGE PRESSURE  
FOR SOLID ROCKET MOTOR

























































































































































































































































